In Vivo Dosimetry with GDCA in Particle Therapy: Variations in Secondary Photon Radiation Across Ion Species

U.PORTO
FACULDADE DE CIÊNCIAS
UNIVERSIDADE DO PORTO

MSc

Tiago Bettio
Master in Medical Physics
Department of Physics and Astronomy of the
Faculty of Sciences of the University of Porto
2023/24

In Vivo Dosimetry with GDCA in Particle Therapy: Variations in Secondary Photon Radiation Across Ion Species

U.PORTO
FACULDADE DE CIÊNCIAS
UNIVERSIDADE DO PORTO

MSC

Tiago Bettio
Project Report carried our as part of the Master in Medical Physics
Department of Physics and Astronomy
2023/24

Supervisor:
Prof. Dr. João Seco, Biomedical Physics in Radiation Oncology – German Cancer Research Center (DKFZ)

Co-supervisor:
Msc.Joana Vale, Specialist Medical Physicist – Atrys Health Portugal – Advanced Medical Center, Santa Maria da Feira Portugal

Co-supervisor:
Prof. Dr. Pedro Teles, Department of Physics and Astronomy of the Faculty of Sciences of the University of Porto

University of Porto

In Vivo Dosimetry with GDCA in Particle Therapy: Variations in Secondary Photon Radiation Across Ion Species

Author:

TIAGO BETTIO

Supervisor:

Prof. Dr. João Seco

Co-supervisors:

Msc. Joana Vale

Prof. Dr. Pedro Telles

Faculty of Sciences of the University of Porto

Department of Physics and Astronomy

October 30, 2024

Acknowledgements

Start a Master in a new country where the professors and the science culture is different from the one you have been experienced your whole life is not an easy task. Many cultural barriers I had to go through in order to finish this master and follow my dream to be a scientist. I wouldn't be able to do so without the friends I've made here in Portugal and there in Germany. Many people gave me support to get it, and I'm very grateful for all of them.

To Professor Doctor Pedro Teles, that has been my teacher since day 1 through many lessons from medical physics and Monte Carlo programing. I thank you for all the support and lessons that have made me able to finish this thesis.

To Joana Vale, I thank you for being the person responsible for my first clinic experience and for the help on this path, as an advisor and also as a friend, with great support.

To Catarina Souto, I thank you for being a great medical physics professional that has inspired me, and the support on the thesis.

To Hugo Freitas, I have truly no words to thank you for all the weekend messages, late night questions and orientation when I most needed.

To Professor Dr. João Seco I want to give a special thanks for jumping into this project since day 1. Dr. João has given me the opportunity of working at one of the best research centers in Europe and supervised my work giving me directions that were crucial for the elaboration of this thesis.

Also, all my colleagues in this master, Maria João, Amizito, Jonas Ternes, have helped me get through this what was a new word for me. My colleagues at the E0471 group on the DKFZ for the enormous support that I've got there, this thesis has definitely the influence of Elpida screams, Clarence calm, Beatriz peace, Mariana happiness, Tenda jokes and so on, there are many great people on that group.

My personal friends I will give a special thanks once going through Porto's winter having to study for 10 exams in one month is not a task that I would handle well without them. Therefore, a special thanks to Maria Clara, Isaac, Renan, Robson, Ialla, João, and many others.

Thanks, my family for all the support and the education that I have received, and all my Brazilians professors and friends.

University of Porto

Abstract

Faculty of Sciences of the University of Porto

Department of Physics and Astronomy

Msc. Medical Physics

In Vivo Dosimetry with GDCA in Particle Therapy: Variations in Secondary Photon Radiation Across Ion Species.

By Tiago Bettio

Heavy particle radiotherapy is a highly advanced form of cancer treatment that uses high-energy particles, such as protons, helium, or carbon ions, to target and destroy tumor cells with minimal damage to surrounding healthy tissues. Radiation dose measurements and calculations are critical aspects of this therapy. Due to the particles high Linear Energy Transfer (LET), accurate dosimetry is essential to ensure optimal treatment outcomes. When irradiated with heavy particles, Gadolinium emits a very specific photon energy spectrum showing promising potential for use *in vivo* dosimetry techniques.

The photon flux generated depends on the type of particle used in the beam, so analyzing the peak signal relative to the equivalent dose could be useful to determine whether spectroscopic techniques might be applied for *in vivo* dose measurement.

In this work Monte Carlo MCNP6 code was used to simulate experimental setup to investigate the code's capability to simulate this spectrum. The findings indicate that the MCNP6 cascade mode, employing the CEM03.03 model, yields accurate predictions for proton beam interactions. However, it significantly underestimates the photon flux, with discrepancies amounting to a factor of 3.2 for helium ions and 54.7 for carbon ions. The equivalent dose for these particles shows that carbon ions produce the strongest signal per ion per mSv.

Keywords: Radiotherapy, Dosimetry, Heavy Particles.

Contents

1. INTRODUCTION 12

2. THEORY FRAMEWORK 15

2.1. HEAVY PARTICLES TREATMENT FACILITIES 18
2.2. HEAVY IONS THERAPY 19
2.2.1. THE PHYSICS OF PROTON THERAPY 19
2.2.1.2. Particle Induced X-Ray Emission (PIXE) 22
2.2.1.3. CSDA Range 22
2.2.1.3.1. PET imaging 25
2.2.1.3.2. Prompt Gamma Imaging 25
2.2.1.4. Nuclear Reactions 27
2.2.1.4.1. Neutron Emission Decay: Emission of a neutron particle 30
2.2.1.4.2. Neutron interaction with matter 30
2.2.2. HELIUM AND CARBON ION THERAPY 31
2.2.2.1. Energy Loss rate (Linear Stopping Power) 32
2.2.2.2. CSDA Range 33
2.2.2.3. Nuclear reactions 34
2.3. DOSIMETRY 37
2.4. GADOLINIUM (Gd) 39
2.4.1. IN VIVO DOSIMETRY WITH GADOLINIUM 41
2.5. MONTE CARLO METHOD 41
2.5.1. MONTE CARLO METHOD VS DETERMINISTIC METHOD 43
2.5.2. MCNP CODE 43
2.5.2.1. Nuclear Data and Reactions 44
2.5.2.2. Physics 45

3. METHODOLOGY 46

3.1. PRACTICAL DOSIMETRY STUDIES 46
3.2. EXPERIMENTAL SETUP 46
3.2.1. DETECTORS 48
3.2.1.1. Cerium Bromide ($CeBr3$) Scintillator 48
3.3. EXPERIMENTAL RESULTS 49
3.4. MCNP CODE 51
3.4.1. 43 KEV PEAK REGION SPECTRUM MCNP CODE VALIDATION 51
3.4.1.1. Physics Model 52
3.4.1.2. Geometry 55
3.4.1.3. Materials 55
3.4.1.4. Source 57
3.4.1.5. Tally detector 58

3.4.1.6. Single Track card 60
3.4.1.7. Coarse Grained Multiscale (CGM) 61
3.4.2. EQUIVALENT DOSE CALCULATION 62
3.4.2.1. Tally Detector 62
3.5. SPECTRUM ANALYSIS 64
3.5.1. NORMALIZATION OF THE SPECTRUM 65
3.5.2. SIGNAL CONVOLUTION 65
3.6. EQUIVALENT DOSE ANALYSIS 68

4. SIMULATION RESULTS 70

4.1. 43 KEV PEAK SIMULATIONS 70
4.1.1. PROTON BEAM 70
4.1.2. HELIUM BEAM 73
4.1.3. CARBON BEAM 75
4.2. EQUIVALENT DOSE 77
4.2.2. ENERGY DEPOSITION AND MEASURED DOSE 78

5. DISCUSSION 80

5.1. 43 KEV PEAK REGION 80
5.1.1. SPECTRUMS ANALYSIS 81
5.1.2. NEUTRON PRODUCTION VS PEAK SIGNAL 84
5.1.3. PIXE PRODUCTION VS SIGNAL 86
5.2. EQUIVALENT DOSE 90
5.2.1. PROTON BEAM 90
5.2.2. HELIUM BEAM 91
5.2.3. CARBON BEAM 91
5.2.4. PHYSICS ABSORBED DOSE COMPARATION 92
5.2.5. EQUIVALENT DOSE COMPARATION 94

6. CONCLUSION 97

List of Figures

Figure 1 - Therapeutic window. [9] 16
Figure 2 - Illustration of proton interaction mechanisms. (p: proton, e: electron, n: neutron, Y: gamma Rays [4].......... 19
Figure 3 - Absorbed dose D as function of depth z in water from an unmodulated proton Bragg peak. Produced with a proton beam with initial 154 MeV [4]. 21
Figure 4 - Relative fraction of the fluence in a broad beam of protons remaining as function of depth in water. [4] 23
Figure 5 - Relationship between the Stopping Power, Range and Energy of the beam. [4].......... 24
Figure 6 - Gent4.10 simulation of a proton beam penetrating in water. [25] 26
Figure 7 - Proton induced nuclear cross sections for C12 production comparison with different data tables and simulations. [29] 29
Figure 8 - Relative absorbed dose of high energy x-rays, protons Helium and carbons ions as a function of depth in water. [14]. 32
Figure 9 - Stopping power of different light ions as function of energy [31]. 33
Figure 10 - Range of different ions in water as function of energy per nucleon. [31] 34
Figure 11 - Sketch of two possible nuclear reactions. Top: nucleon-nucleus. Bottom: Nucleus-Nucleus. Taken from [22]. 35
Figure 12 - Multiple de-excitation reactions for different ion beams. [26] 36
Figure 13 - Relative importance of the three major types of gamma-ray interactions. [8] 38
Figure 14 - A representative characteristic X-ray spectrum from Gd natural. [39] . 40
Figure 15 - Event log of a life particle throughout its life in a medium. [43] 42
Figure 16 - HIT treatment facility 3D scheme. Source: https://www.klinikum.uni-heidelberg.de/.......... 46
Figure 17 - Experimental Setup. On the Left the Cerium Bromide Detector at the center the Dotarem flask and on the right the Cadimo detector. 47
Figure 18 - Schematic diagram of a scintillation detector along with the photomultiplier tube (PMT) data from: web.stanford.edu/groups/scintillators/scintillators.html, accessed 15/07/2024. 48
Figure 19 - Full range PGS spectra for proton, helium and carbon irradiation of a vial either filled with GD or water. [50] 49
Figure 20 - PGS spectra of the steps used to quantify the GD peak. a: Selection of region of interest and baseline restoration. b: Gaussian fit to the GD peak and area determination. [50]. 50
Figure 21 - GD signal as function of ion for irradiation of a vial filled with GD. [50]. 51
Figure 22 - Flow chart of nuclear-reaction calculations by CEM03.03 [53] 53

Figure 23 - 2D Neutron Spectra at different angles from a thin 12C target bombarded with 290 MeV/u 12C beam. taken from: [22] 54
Figure 24 - MCNP6 output geometry file. 55
Figure 25 - Isotropic distribution of prompt-gamma and X- ray area around the Dotarem Flask 60
Figure 26 - 2D spectrum from 10 keV to 70 keV. On the left neutron free without single track on the right neutron free with single track for electrons under 70 keV for Proton beam. 61
Figure 27 - 2D spectrum of a proton irradiation into da Gadolinium Flask. 66
Figure 28 - 2D spectrum of a convolve curve representing the Peak area sum. 67
Figure 29 - 2D spectrum of a proton irradiation on a Gadolinium flask with 1 keV bin. 68
Figure 30 - 2D Convoluted Spectrum for a proton beam irradiation on DOTAREM from the MCNP6 Simulation. 70
Figure 31 - 2D convoluted Spectrum with error bars from the MCNP6 simulation for a proton beam of the interested zone. 71
Figure 32 – Left: The spectrum selection from 30 to 60 keV marked in the red and green lines respectively. Right: the calculated area delimited over the baseline. 72
Figure 33 - 2D Helium beam spectrum. 73
Figure 34 - 2D convoluted spectrum with error bars from MCNP6 simulation of helium beam of the interested zone. 74
Figure 35 - Left: The spectrum selection from 30 to 60 keV marked in the red and green lines respectively. Right: The calculated area delimited over the baseline. 74
Figure 36 - 2D convoluted spectrum for a carbon beam irradiation on DOTAREM from the MCNP6 simulation. 75
Figure 37 - 2D convolved spectrum with error bars from the MCNP6 simulation. 76
Figure 38 - Left: The spectrum selection from 30 to 60 keV marked in the red and green lines respectively. Right: The calculated area delimited over the baseline. 76
Figure 39 - GD signal as function of ion for irradiation of a vial filled with GD simulated in MCNP6. 80
Figure 40 - Comparation areas of the simulation and the experimental data. 81
Figure 41 - Plot Crossing the simulated data from MCNP6 and the experimental data for Proton (top), Helium (medium) and Carbon (bottom) 83
Figure 42 - Neutron cross-section of gadolinium depending on energy of irradiated neutron. [62] 85
Figure 43 - Neutron Free simulated areas. 87
Figure 44 - Bar plot of the calculated 43 peak region area from a full particle simulation vs neutron free particle free simulation on MCNP6 87
Figure 45 - Bar plot of the calculated 43 peak region area from a full particle simulation vs secondary particle free simulation on MCNP6 88
Figure 46 - Normalized area for particles/second and Gray. 93

Figure 47 - Normalized weighted area of the 3 different ion species. 95

List of Tables

Table 1 - Interaction protons with matter [4] 20
Table 2 - Characteristics X-ray from most abundant atoms in organic tissue. (https://xdb.lbl.gov/Section1/Table_1-2.pdf) 22
Table 3 - Proton induced nuclear reaction when 12C is the atom target. [28] .. 27
Table 4 - Natural Gadolinium composition. [3] 39
Table 5 - Table 5 - Photon Emission probabilities for the Gd isotopes interested in this study. [38] 41
Table 6 – Total of irradiations performed at the HIT institute. 47
Table 7 - Percentage of $DotaremR$compound. 56
Table 8 - Weighting Factor for particles used in this work. [60] 64
Table 9 – Zone of interest bins relative errors for the Proton beam simulation 72
Table 10 – Zone of interest bins relative errors for the helium beam simulation. ... 73
Table 11 - Some bins relative errors for the carbon beam simulation 75
Table 12 - Results of the Neutron Spectra analysis of its energy on different ion species. 77
Table 13 - Proton Beam simulated energy deposition at the flask. 78
Table 14 - Helium beam simulated energy deposition at the flask. 78
Table 15 - Carbon Beam simulated energy deposition at the flask. 79
Table 16 - Total of Neutrons created in the MCNP6 simulation with cross-sections higher than 10000 b. 85

1. Introduction

Radiotherapy has a rich history that began in the late 19th century with Wilhelm Röntgen's discovery of X-rays in 1895 and the discovery of radium by Marie and Pierre Curie shortly thereafter [1]. These breakthroughs laid the foundation for using ionizing radiation to treat cancer, with early radiotherapy employing X-rays and radium to target tumors. Over the years, advancements in technology and a deeper understanding of the radiation's effects in biological tissues led to the development of more precise treatment methods, such as Intensity Modulated Radiation Therapy (IMRT) [1]. By the latter half of the 20th century, proton therapy emerged, offering a treatment that minimized damage to surrounding healthy tissues. This evolution continued, driven by the need to further reduce side effects and increase efficacy, leading to the development of new treatments. Heavy ions, such as helium and carbon ions, provide unique advantages due to their higher mass and charge, allowing even greater precision in targeting tumors and delivering a potent dose of radiation directly to cancer cells while sparing surrounding healthy tissue [2]. This precision and effectiveness make heavy ion therapy particularly valuable in treating radio-resistant tumors and those located near critical structures [2]. In radiation therapy, precise dose delivery is vital for maximizing therapeutic efficacy while minimizing harm to healthy tissues. In vivo dosimetry, which involves the real-time measurement of radiation dose within a patient, is a great tool that can be used for ensuring the accuracy of treatment. One emerging approach in this field is the use of Gadolinium (Gd), due to its high atomic number (Z=64) and its ability to emit prompt gamma and X-rays upon nuclear interactions [3]. When heavy particles are employed, the frequency of nuclear reactions increases due to the elevated incident energy required for these particles to penetrate tissue effectively [4]. Gadolinium atoms emit a distinct spectral signature compared to the atoms typically found in the organic tissue. This characteristic renders gadolinium an excellent candidate for in vivo dosimetry [5].

This thesis investigates the prompt gamma-ray and characteristic X-ray emissions of Gadolinium when exposed to different ion species, aiming primarily to compare experimental observations with simulations conducted using the Monte Carlo N-Particle transport code, MCNP6. Such comparisons are essential for validating the simulation models increasingly relied upon in radiation therapy planning and dosimetry. Although the Monte Carlo N-Particle Transport Code (MCNP6) has been extensively validated for applications involving prompt gamma-ray production and dose deposition [5], [6], heavy ion therapy necessitates the simulation of interactions involving ions that are heavier than protons. This study will explore these phenomena in detail. Additionally, the study involves experimental measurements for in vivo dosimetry related to photon emissions. Different ion species interact uniquely with matter, and thus the intensity of flux from gadolinium's prompt gamma-ray and characteristic X-ray emissions varies accordingly. The gadolinium photon emissions will be correlated with the equivalent dose, a measure that takes into account solely the LET. For clinical applications, it is crucial to relate these variables to understand the actual impact of radiation biological effects. In vivo dosimetry techniques depend on the generation of signals from these photons. A secondary objective of this work is to relate the signal produced by experimental data to the dose deposition of energy calculated using the MCNP code. This relationship is important for determining which ion species produce the highest signal under equivalent physical conditions.

The initial phase of this study is conducted at Atrys Health Portugal – Advanced Medical Center, focusing on a practical investigation in dosimetry. Then the study moves to an experiment conducted at the Heidelberg Ion Beam Therapy Center (HIT), where treatment beams were utilized to irradiate a Dotarem® flask, a pharmaceutical preparation containing gadolinium atoms. The emitted photon spectrum from gadolinium was subsequently collected using a scintillator detector. This experimental setup was then modeled using the MCNP6 code, replicating the same environmental conditions, particle energies, and distances to facilitate a comprehensive analysis of the emitted spectrum and radiation dose.

The structure of this thesis is organized as follows: Section 1 delves into the theoretical framework, emphasizing the physical characteristics of heavy ion radiotherapy, the interactions of Gadolinium with ionizing radiation, and its potential applications in in vivo dosimetry. Additionally, this section discusses the operational principles and functionalities of the MCNP6 simulation code. Section 2 outlines the methodology employed in this study, detailing the experimental setup, the selected input parameters for MCNP6, and the methods used for data processing. Section 3 presents the simulation results, which are subsequently followed by a comprehensive discussion that analyzes the findings and examines the underlying phenomena. Section 4 addresses the implications of the results for clinical practice and future research, with a particular focus on the potential of protons, helium, and carbon ions to enhance the precision of Gadolinium-based dosimetry. Finally, Section 5 concludes the thesis by synthesizing the key findings and their significance within the context of radiation therapy advancements.

The findings of this work could support the implementation of *in vivo* dosimetry techniques in heavy ion therapy treatments, potentially improving patient outcomes through real-time dose monitoring to ensure accurate administration of prescribed doses. Understanding gadolinium-induced photon emissions and neutron capture for different ion species will broaden the clinical applicability of this technique. The use of the well-validated MCNP6 code also reduces uncertainty regarding the method. The physics models, data tables, and configurations used in this work contribute to a deeper understanding of how this code can be applied to simulate these phenomena with precision. Additionally, comparing the signal production of different ion species aids the future clinical application of this method. This study showed that carbon, despite its higher LET, stands out as a promising candidate for in vivo dosimetry using gadolinium prompt gamma-ray and characteristic X-ray emissions. Under equivalent physical conditions, the carbon beam produced a higher signal per source particle per μSv of equivalent dose.

2. Theory Framework

The technique of radiotherapy emerged as a cancer treatment at the end of the 19th century, following the discovery of X-rays by physicist Wilhelm Conrad Röntgen in 1895 and the subsequent discovery of radium (Ra) by Marie and Pierre Curie in 1898 [1]. This marked one of the earliest applications of radiation in cancer therapy, with the first patient treatment occurring in 1898 [7]. Radiotherapy involves the generation of an external radiation beam that is precisely targeted at a predetermined volume where the tumor is located. The primary objective of this treatment modality is to induce maximum damage to cancer cells while minimizing collateral damage to healthy surrounding tissues. Achieving this goal presents significant challenges, as numerous variables must be taken into account, including tumor location, the proximity of surrounding organs, and the biological characteristics of the tumor itself. The amount of energy deposited by the radiation ($\bar{\varepsilon}$) per unit of mass (m) is defined as the absorbed dose (D) [8], which is a critical parameter in determining the effectiveness and safety of the treatment, and is defined as:

$$D = \frac{d\bar{\varepsilon}}{dm}, \qquad [Gy] \tag{1}$$

Radiation therapy delivers energy throughout the treatment volume, resulting in the absorption of a certain energy by both tumor and healthy cells. Therefore, it is essential to analyze two distinct curves when planning radiotherapy treatment: Tumor Control Probability (TCP) and Normal Tissue Complication Probability (NTCP). These curves define the therapeutic window for radiation therapy [4]. The TCP curve represents the likelihood of eradicating tumor cells, which is influenced by various factors, including the type of radiation used, beam energy, the LET of the radiation, and the biological characteristics of the tumor. Conversely, the NTCP curve establishes a limit for treatment by assessing the probability of complications in normal tissues. This curve indicates the maximum dose that can be safely administered, also depending on the aforementioned parameters. The therapeutic window is the region where effective radiotherapy occurs, as illustrated in Figure 1. As the radiation dose increases, the TCP also rises, enhancing the likelihood of tumor control and patient cure. However, an increase in the dose simultaneously elevates the NTCP, leading to a higher risk of adverse effects in healthy tissues. Balancing these probabilities is crucial for optimizing treatment outcomes while minimizing complications.

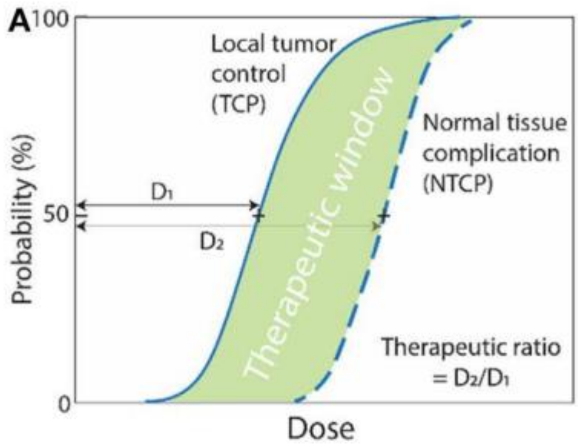

Figure 1 - Therapeutic window [9].

Technological advancements aim to enhance the therapeutic window in cancer treatment, potentially increasing the likelihood of patient cure rates [1]. Currently, numerous radiotherapy techniques are available to achieve this goal. The most commonly utilized radiation modalities are photons and electrons, which were among the first particles employed in clinical practice; these machines and their associated technologies have been in development for many years [1]. Recent research has significantly improved treatments involving these particles, with methodologies such as Intensity-Modulated Radiation Therapy and Volumetric Modulated Arc Therapy (VMAT) contributing to an expanded therapeutic window. IMRT utilizes advanced computational resources to modulate the intensity of the radiation beam during treatment, allowing for more precise targeting of tumor tissues while sparing surrounding healthy cells. In contrast, VMAT employs the continuous movement of the treatment gantry to deliver radiation from multiple angles, optimizing dose distribution and further reducing collateral damage to healthy tissues. Both techniques share the common objective of maximizing dose deposition to the tumor while minimizing adverse effects on normal cells.

An alternative strategy for enhancing the therapeutic window in cancer treatment is heavy ion therapy, which involves the generation of beams composed of heavy charged particles such as protons, helium ions, and carbon ions. This approach was first proposed in 1946 by Robert Wilson, who published a seminal paper advocating the use of proton beams for the treatment of deep-seated tumors in patients [10]. Following this the first patient was treated with protons beams in 1954 at the Lawrence Berkeley Laboratory [11]. There are several reasons why heavy particles beams are interesting for radiotherapy, they have physics proprieties that make their deposition of energy more selected, resulting in a bigger spare of healthy tissue. Although the adoption of this treatment is difficult due to the relatively large cost involved in the infrastructure and maintenance of heavy charged particles facilities in comparison to megavoltage x-ray and electrons installations [12].

The International Commission on Radiological Protection (ICRP), in its publication ICRP 26 [13], established the concept of **Relative Biological Effectiveness (RBE)** to address the varying biological effects of different types of ionizing radiation as they interact with tissue.

$$RBE = \frac{Reference\ Dose}{Tested\ radiation\ Dose} \tag{2}$$

The reference dose is defined as the radiation dose required to elicit a specific biological effect. In contrast, the tested radiation dose refers to the dose delivered by the particle under investigation that is necessary to produce the same biological effect [13]. RBE is a crucial parameter in radiobiology, used to compare the biological effectiveness of various radiation types by quantifying the extent of biological damage induced by a specific type and energy of radiation relative to a reference radiation, typically X-rays or gamma rays at a defined energy level. The significance of RBE arises from the fact that different radiation types—such as alpha particles, neutrons, and gamma rays—can elicit distinct biological damage profiles, even when they deliver equivalent amounts of energy to biological tissues. The RBE value is influenced by multiple factors, including the radiation type, energy level, the biological tissue in question, and the specific biological endpoints assessed (e.g., DNA damage, cell lethality) [14]. For instance, alpha particles, characterized by their high ionization potential, generally exhibit a higher RBE than less ionizing radiation, such as X-rays. The application of RBE is vital in the fields of radiation protection and radiotherapy, as it facilitates the adjustment of radiation doses to account for disparities in biological damage, thereby ensuring that the effective dose accurately reflects the actual risk associated with exposure to various forms of radiation.

In heavy ion therapy, RBE plays a critical role in treatment planning. Therefore, a specific dose calculation is introduced for these cases. The biological weighting of the absorbed dose (D_{IsoE}) provides a comprehensive basis for understanding, interpreting, and reconstructing treatments [15].This value can be calculated as follows:

$$D_{IsoE} = D \times W_{IsoE} \tag{3}$$

, where W_{IsoE} represents the weighting factor accounting for the effects of various parameters such as dose per fraction, total treatment time, dose rate, instantaneous dose rate, dose homogeneity, radiation quality (RBE), and other technical or biological conditions. In this study, only RBE is considered as the primary factor for investigation, with other parameters excluded from analysis

To better understand the various types of radiation effects on biological tissues, it is preferable to utilize the concept of equivalent dose. Equivalent dose is a measure predominantly employed in radiation protection to evaluate the biological impact of an absorbed dose of radiation, accounting for the type of radiation involved [16]. It is calculated by multiplying the absorbed dose average over the tissue or organ T, by a radiation weighting factor (W_R) , which reflects the relative biological effectiveness of the different radiation types [16].

$$H_T = \sum_R W_R \, . \, D_{T,R} \tag{4}$$

This equation represents the biological effectiveness of specific types of radiation without considering tissue-specific factors. The weighting factor, known as the Relative Biological Effectiveness (RBE), varies because different radiation types—such as helium ions, protons, and carbon ions—induce varying levels of biological damage. Specifically, carbon ions exhibit a substantially higher radiation weighting factor due to their greater mass and charge, which enhances their efficacy in damaging cancer cells while simultaneously increasing the risk to adjacent healthy tissues [16]. These variations in energy transfer and biological impact necessitate the application of different equivalent doses for each radiation type in order to accurately reflect their potential to induce biological damage in radiation therapy.

2.1. Heavy Particles treatment facilities

To achieve the desired energy levels for therapeutic beams, heavy charged particles are generated and accelerated using devices such as cyclotrons and synchrotrons [12]. A cyclotron accelerates particles along a spiral trajectory through two half-cylindrical electrodes, where an alternating radiofrequency voltage induces acceleration, while a uniform magnetic field keeps the particles in a circular path. As particles exit the gap between electrodes, they continue to accelerate as they re-enter the gap with reversed electric field direction, resulting in a gradual increase in kinetic energy with each passage. In contrast, a synchrotron maintains a constant-radius circular orbit within a vacuum chamber, with a time-varying magnetic field that compensates for the increase in particle mass at higher energies, allowing for the acceleration of both electrons and heavier particles. In this system, particles gain kinetic energy as they pass through a resonator cavity multiple times, and they are often injected after initial acceleration from auxiliary equipment, such as a linear accelerator [8].

2.2. Heavy Ions Therapy

2.2.1. The Physics of proton therapy

A proton beam interacts with matter in a manner distinct from that of electrons and photons. The primary mechanisms are Coulomb interactions with atomic electrons, Coulomb interactions with the atomic nucleus, nuclear reactions, and Bremsstrahlung (Bs), as illustrated in Figure 2 [4]. This figure depicts the most common interactions of protons with the medium. Panel (a) illustrates an inelastic Coulomb interaction, which accounts for the continuous loss of kinetic energy by the protons [8]. Despite these interactions resulting in energy loss, protons typically maintain a straight-line trajectory due to their rest mass being approximately 1832 times greater than that of electrons [4]. When these high-energy particles impact a material, they can transfer momentum and energy to electrons within the atoms of that material, displacing them from their bound states. These displaced electrons, now termed "knock-on electrons," can then travel through the material, often leading to further ionization, excitation of atoms, or secondary damage to the material's structure [17]. In panel (b), elastic scattering is presented, which occurs due to the repulsive Coulomb force exerted by the atomic nucleus. Because the nucleus possesses a significantly larger mass, it can deflect the proton from its original straight-line path. Panel (c) shows a nuclear inelastic reaction, wherein a proton with sufficient energy can overcome the Coulomb repulsion of the nucleus. This interaction may result in the emission of particles such as protons, deuterons, tritons, or heavier ions, as well as one or more neutrons. Although these nuclear reactions are less frequent, they can produce gamma-ray emissions detectable in spectroscopy profiles. While Bremsstrahlung radiation is theoretically possible with protons, its significance is negligible when considering the energies associated with therapeutic proton beams [4].

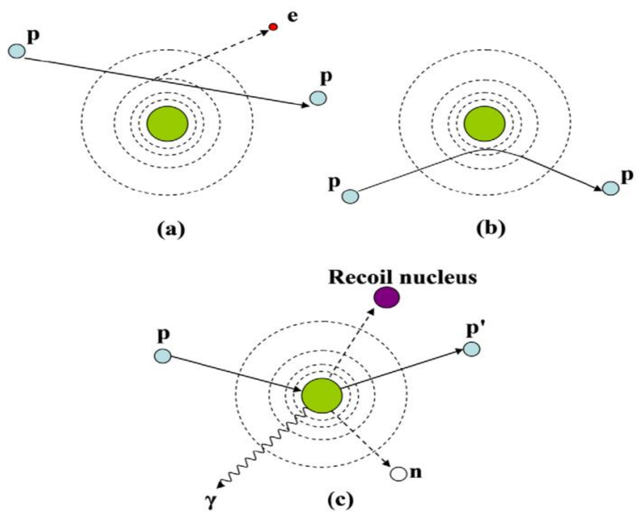

Figure 2 - Illustration of proton interaction mechanisms. (p: proton, e: electron, n: neutron, Y: gamma Rays [4].

The interactions between protons and matter play a crucial role in determining the effects of proton therapy on the patient's body. Table 1 provides a comprehensive summary of the various types of proton interactions, their respective targets, the resultant secondary particles produced, the influence on the incident proton beam, and the associated dosimetric outcomes.

Interaction type	Interaction target	Interaction products	Influence on proton	Influence on dosimetry
Inelastic Coulomb Scattering	Atomic Electrons	Primary proton, Ionization electrons	Quasi-Continuous Energy loss	Energy Loss determines range in patient
Elastic Coulomb Scattering	Atomic Nucleus	Primary protons, recoil Nucleus	Change in trajectory	Determines Lateral Penumbral Sharpness
Non-Elastic Nuclear Reactions	Atomic Nucleus	Secondary Protons and heavier ions, neutrons, and gamma rays	Removal of primary protons from beam	Primary fluence, generation of stray neutrons, generation of prompt gammas for in vivo interrogation
Bremsstrahlung	Atomic Nucleus	Primary proton, BS photons.	Energy loss, change in trajectory	Negligible.

Table 1 - Interaction protons with matter [4].

2.2.1.1. Stopping Power

The stopping power is defined as the rate of energy lost (dE) per unit of path length (dX) [8]. This rate is typically influenced by the characteristics of the medium through which the radiation travels. When the linear stopping power is divided by the density (ρ) of the absorber, it yields the mass stopping power, defined as:

$$\frac{S}{\rho} = -\frac{dE}{\rho.dX}, [MeV.cm^2.g^{-1}] \tag{5}$$

This relationship highlights how the energy lost per unit length varies with the material properties, allowing for a more comprehensive understanding of the interaction between radiation and matter.

As protons traverse a medium, initially lose energy only at a moderate rate due to the inverse dependence on its velocity squared ($\frac{1}{\beta^2}$). However, due to quasi-continuous Coulomb interactions with the orbital electrons in the atoms, $\frac{S}{\rho}$ will increase, and the particles will slow-down, and start to lose their last bits of energy increasingly locally, leading to an energy loss peak, represented at figure 3 – the Bragg peak – after which they come to rest. At this peak, protons deposit the majority of their energy [4]. Beyond the Bragg peak, energy deposition decreases rapidly, enabling precise targeting of tumors while minimizing damage to adjacent healthy tissues. This distinctive depth-dose characteristic distinguishes proton therapy from conventional X-ray treatments, establishing it as a valuable approach for the treatment of specific cancers [4].

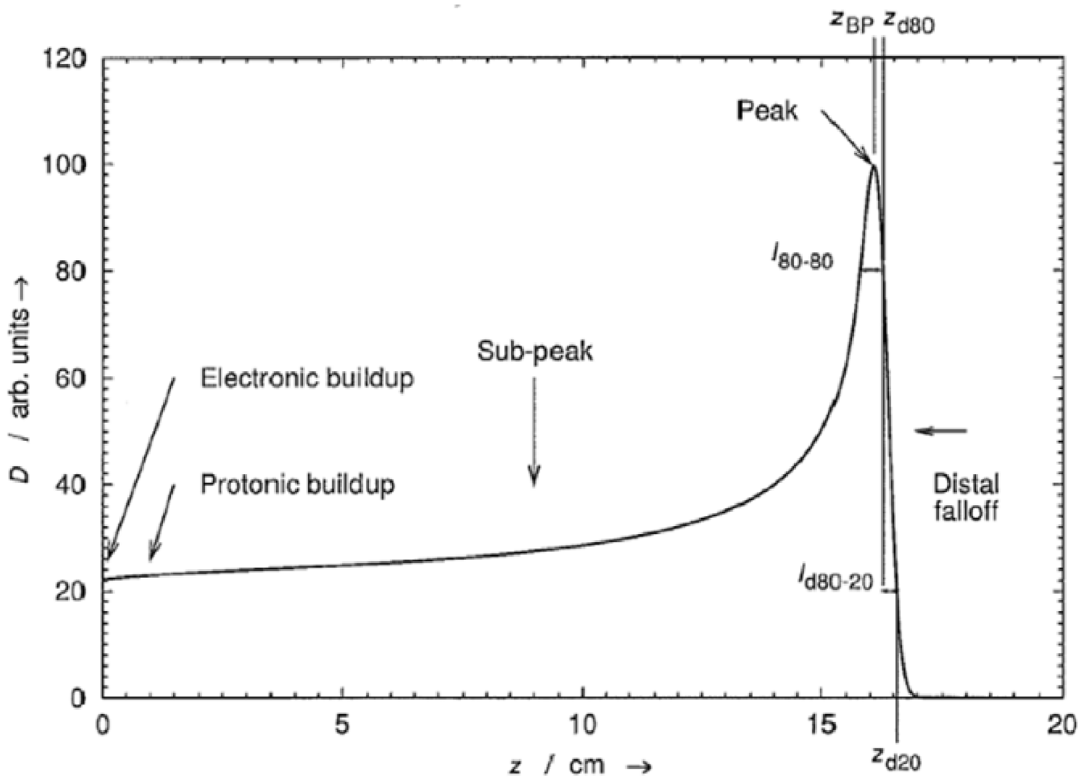

Figure 3 - Absorbed dose D as function of depth z in water from an unmodulated proton Bragg peak. Produced with a proton beam with initial 154 MeV [4].

The dose distribution in proton therapy is predominantly influenced by the generation of Knock-on electrons (KOE) generated by hard-collisions of the heavy particles with these electrons [4]. In an aqueous medium, these secondary electrons typically do not acquire sufficient energy to travel beyond a few millimeters from the proton trajectory. This characteristic allows proton therapy to minimize side effects, as energy deposition occurs locally within the tumor tissue, thereby sparing surrounding healthy structures. However, the energy lost determined by the stopping power does not equate to the energy deposited by the proton beam itself. Some secondary particles generated by the medium's ionization can transport energy away from the area and do not contribute to biological damage [4].

2.2.1.2. Particle Induced X-Ray Emission (PIXE)

The same hard-collisions between the charged particles and the orbital electrons of a medium are responsible for delivering a dose to the medium by removing electrons from the atoms, are also responsible for induced x-ray emissions, via fluorescence that will compete with Auger and Cherenkov emissions [9]. These interactions also facilitate the emission of induced X-rays. The human body is composed of various types of atoms, and when subjected to bombardment by particle beams, core electrons are primarily ejected from inner shells [18]. This ejection depends on the binding energy of the electrons as well as the energy of the incident particle. Subsequently, outer shell electrons transition to fill the vacancies created in the inner shells, and this de-excitation process results in the emission of X-rays with energies that are characteristic of the specific atom [18]. When an electron is ejected from these inner shells, an outer shell electron fills the vacancy, leading to the emission of X-rays that correspond to the energy difference associated with the shell transitions, a characteristic that is specific to the atom in question [19]. The most prevalent atoms in the human body are carbon-12 (^{12}C), oxygen-16 (^{16}O), and nitrogen-15 (^{15}N) [5]. The energy of these emitted characteristic X-rays is intrinsic to the atomic structure of each element, functioning as a unique signature that can be utilized to identify the irradiated atom. In the context of organic tissue, the relevant atoms possess two electron shells (K and L). Consequently, the emitted X-rays primarily arise from the Kα transition, wherein an electron transitions from the L shell to the K shell (table 2).

Nucleus	$k\alpha_1$ (keV)
^{12}**C**	0.277
^{16}**O**	0.392
^{15}**N**	0.525

Table 2 - Characteristics X-ray from most abundant atoms in organic tissue (Adapted from: X-Ray Data Booklet, 2009.).

In heavy ions particle therapy, this is known as Particle Induced X-ray Emission (PIXE), and it can be used in heavy ions therapy to verify the range accuracy of the beam to improve the target localization and reduce patient setup errors [20].

2.2.1.3. CSDA Range

In proton therapy, range refers to the distance that protons travel in tissue before they come to a complete stop and release their maximum energy [21].

As previously discussed, nuclear reactions also influence the flux of the beam. As illustrated in Figure 4, the effect of nuclear reactions on beam flux is relatively minor compared to the reduction in velocity.

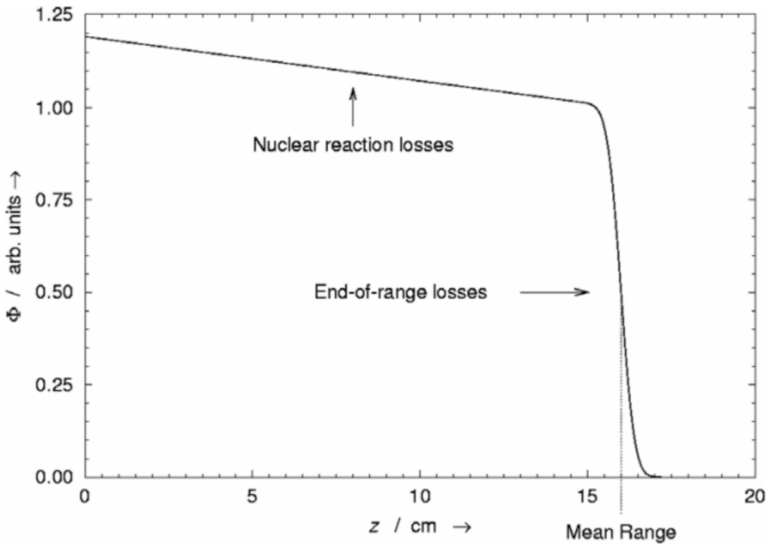

Figure 4 - Relative fraction of the fluence in a broad beam of protons remaining as function of depth in water [4].

The Continuous Slowing Down Approximation (CSDA) range refers to the average distance a charged particle travels in a material before coming to rest [17]. This range is calculated under the assumption that the particle undergoes continuous and uniform energy loss primarily through ionization and excitation processes, rather than through discrete interactions [22]. The CSDA range ($R(E)$) is calculated as follows:

$$R(E) = \int_0^E \left(\frac{dE'}{\rho . dx}\right)^{-1} . dE', \qquad \left[\frac{g}{cm^2}\right] \tag{6}$$

Where dE is the energy lost, dx is the unit of path length, and ρ is the medium density.

Using this equation, it is possible to estimate the proton range, as illustrated in Figure 5, which presents the range for various initial energies. The proton range of interest typically spans from approximately 1 mm, roughly the size of a voxel in an anatomical image of patient anatomy, to about 30 cm, which corresponds to the midline of a large adult male's pelvis, the deepest region within the human body. These ranges correspond to proton energies of approximately 11 MeV and 220 MeV, respectively [4].

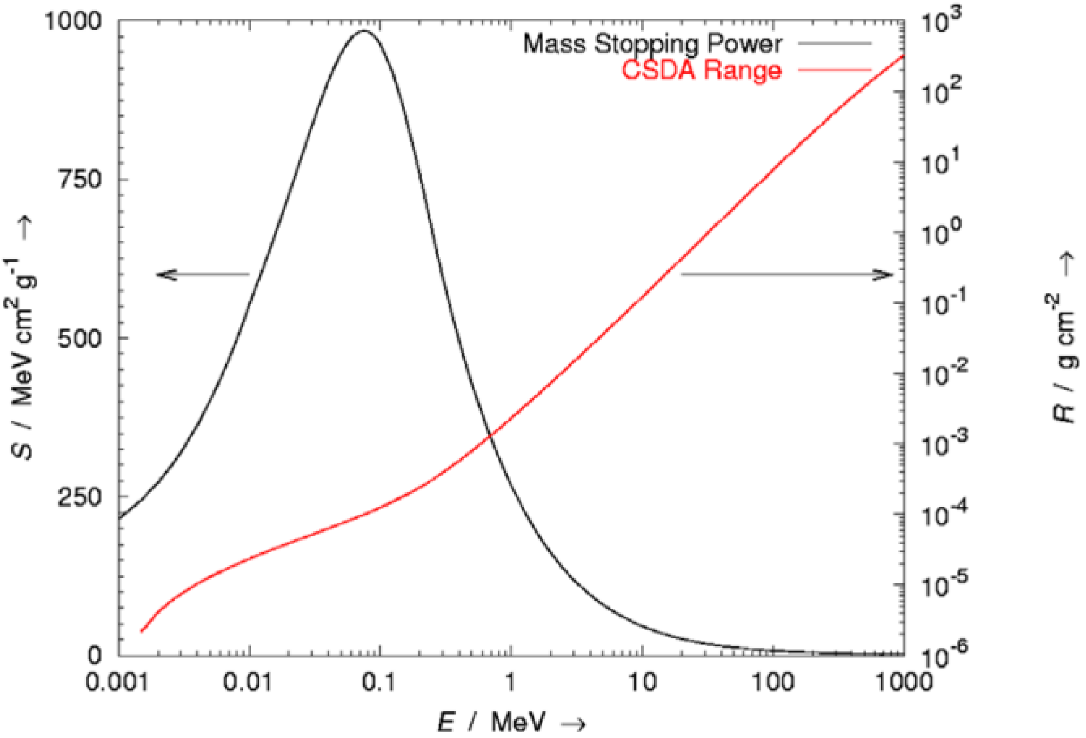

Figure 5 - Relationship between the Stopping Power, Range and Energy of the beam [4].

Figure 5 demonstrates that the stopping power generally decreases as the energy of the proton beam increases from 0.1 MeV and higher, with a corresponding increase in the beam's range. This trend aligns with theoretical predictions, as higher proton energies (and velocities) reduce the frequency of Coulomb interactions with electrons in the medium. Accurate determination of proton penetration depth is crucial for all proton therapy techniques; however, precise range verification is challenging due to inherent uncertainties in proton range [14]. Unlike photon treatments, where dose deposition is more diffuse, proton dose deposition is sharply defined by the Bragg peak. Consequently, even minor range miscalculations can significantly impact treatment outcomes. The heterogeneity of human tissue introduces additional complexity, as the beam traverses varying densities, which directly affects Coulomb interactions and thereby the rate of energy loss [17]. Modern proton therapy planning mitigates some of these challenges by using computerized tomography (CT) datasets that model tissue heterogeneity with a high degree of accuracy [22]. However, limitations in CT imaging, such as acquisition noise and beam hardening artifacts, can still affect range predictions. In conventional radiotherapy, the planning target volume (PTV) concept addresses uncertainties, including patient positioning. In proton therapy, however, PTV adjustments are complex; patient positioning directly affects beam range as tissue density heterogeneities shift, altering dose deposition [23].

Numerous solutions have been proposed to address proton range uncertainties, including advanced processing hardware, ‘smearing’ techniques, and robust optimization methods [14]. A promising approach to reduce these uncertainties is in vivo range verification. In the literature, verification methods are broadly categorized as direct and indirect. In this work, two indirect methods are particularly noteworthy: PET imaging and prompt gamma imaging.

2.2.1.3.1. PET imaging

This method is not applicable to the current study. It involves using PET imaging systems to detect gamma rays emitted during the annihilation of a positron with an electron. In tissue, nuclear interactions during proton travel generate positron-emitting isotopes, such as ^{11}C, ^{13}N and ^{15}O. These isotopes decay via β^+ emission, where the positron subsequently encounters an electron, resulting in annihilation and the production of two coincident gamma photons. These photons are detected by the PET camera, enabling imaging of the positron-emitting distribution within the medium [24].

2.2.1.3.2. Prompt Gamma Imaging

During their passage through tissue, protons with sufficient energy can induce nuclear reactions, some of which result in gamma-ray emission [23]. The sources of prompt gamma emission will be discussed in the following section on nuclear reactions. Following a nuclear inelastic interaction, the target nucleus is excited to a higher energy state and subsequently emits secondary particle(s) to return to its ground state. It has been demonstrated that such inelastic interactions occur nearly throughout the entire proton penetration path, extending up to approximately 2-3 mm before the Bragg peak and subsequent energy fall-off [17]. At this point, the particles in the proton beam possess lower energy, resulting in a decrease in reaction cross-sections as the protons lack sufficient energy to overcome the nuclear repulsive force. A simulation using Geant4.10, conducted by, is shown in Figure 6, illustrating the longitudinal distribution of prompt gamma emission and neutron production along the proton path [21].

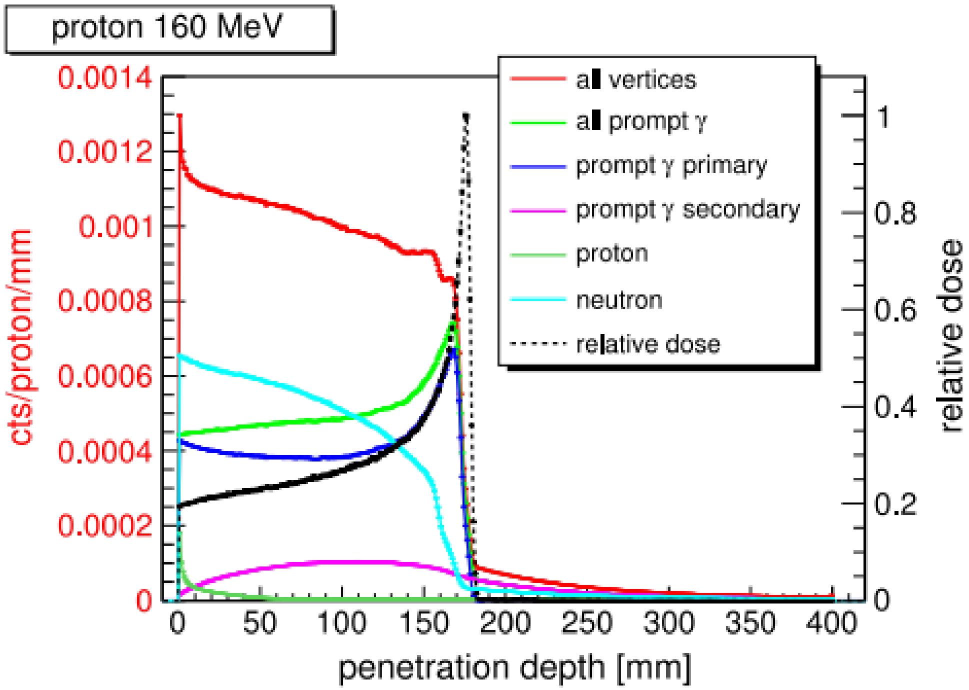

Figure 6 - Gent4.10 simulation of a proton beam penetrating in water [25].

It can be observed that prompt gamma rays exhibit a similar depth of fall-off as that of proton beam particles. This observation has driven the development of prompt gamma techniques that leverage measured information to infer particle range. Prompt Gamma Imaging (PGI) captures either a 1D longitudinal profile or a 2D/3D spatial distribution of gamma-ray production yields. The feasibility of PGI was first demonstrated by Chul-Hee Ming [23], verifying proton beam range measurements of a 100 MeV beam with an accuracy of 1–2 mm. A related non-imaging approach, Prompt Gamma Timing (PGT), relies on the measurement of gamma-ray time of flight (TOF). For protons with a typical range of 10–15 cm, the nominal TOF to full deceleration in the medium is approximately 1–2 ns; deviations from the expected range are reflected as shifts in the TOF distribution. A study utilizing PGT on a graphite target with a 150 MeV proton beam demonstrated the detection of range shifts of approximately 5 mm [23]. The third technique, Prompt Gamma Ray Spectroscopy (PGS), is based on acquiring discrete gamma-ray lines and analyzing their intensities. As detailed in the following section, the intensity of prompt gamma rays generated from nuclear reactions depends on the velocity of the incident proton beam particles [18]. This is due to its relationship with both the cross-sectional area of the reaction and the abundance of the target element. Because the production cross-section of each specific gamma line is a function of proton energy, it is possible to infer the residual range from these measurements [26]. Another study, by Hueso-González [27] , employed full-scale PGS on a PMMA phantom with clinical proton pencil beam scanning, achieving a 1.1 mm absolute proton range accuracy for each spot in the highest energy layer, with a 95% confidence level.

2.2.1.4. Nuclear Reactions

Proton-nuclear interactions are categorized into two primary processes: nuclear scattering (elastic) and nuclear capture (inelastic) [4]. In the elastic process, protons scatter off the nucleus, generating a lateral spread or "shadow" in the beam profile. In the inelastic process, protons collide with the nucleus, generating a nuclear reaction. The various types of nuclear reactions are outlined in ICRU Report 63 [28]. Table 3 provides an example, using a ^{12}C atom as the target, to illustrate all proton-induced nuclear reactions that occur with it. The table details the resulting transitions of the excited nuclei and the energy of the emitted gamma rays. Additionally, it specifies the mean lifetime of the excited nucleus produced by each nuclear reaction. Observations of this target atom reveal that emission times span from nanoseconds for slower reactions to attoseconds for the fastest ones. This rapid emission of prompt gamma rays facilitates real-time monitoring of the irradiation beam, providing immediate feedback during exposure.

Proton inducted nuclear reactions	Transition	Gamma-ray Energy [MeV]	Mean life [Seconds]
^{12}C(p,x)^{10}B*	$^{10}B^*_{0,718} \rightarrow g.s.$	0.718	1.0×10^{-9}
^{12}C(p,x)^{10}C(e)^{10}B*	$^{10}B^*_{0,718} \rightarrow g.s.$	0.718	1.0×10^{-9}
^{12}C(p,x)^{10}B*	$^{10}B^*_{1,740} \rightarrow {}^{10}B^*_{0,718}$	1.022	7.5×10^{-15}
^{12}C(p,x)^{11}C*	$^{11}C^*_{2} \rightarrow g.s.$	2.000	1.0×10^{-14}
^{12}C(p,x)^{11}B*	$^{11}B^*_{2,125} \rightarrow g.s.$	2.124	5.5×10^{-15}
^{12}C(p,p\`)^{12}C*	$^{12}C^*_{4,439} \rightarrow g.s.$	4.438	6.1×10^{-14}
^{12}C(p,2p)^{11}B*	$^{11}B^*_{4,445} \rightarrow g.s.$	4.44	5.6×10^{-19}
^{12}C(p,x)^{11}C*	$^{12}C^*_{6,339} \rightarrow g.s.$	6.337	$< 1.1 \times 10^{-13}$
^{12}C(p,x)^{11}C*	$^{12}C^*_{6,478} \rightarrow g.s.$	6.476	$< 8.7 \times 10^{-15}$
^{12}C(p,x)^{11}B*	$^{11}B^*_{6,743} \rightarrow g.s.$	6.741	4.3×10^{-20}
^{12}C(p,x)^{11}B*	$^{11}B^*_{6,792} \rightarrow g.s.$	6.790	5.6×10^{-19}
^{12}C(p,p\`)^{12}C*	$^{12}C^*_{15,11} \rightarrow g.s.$	15.10	1.5×10^{-17}

Table 3 - Proton induced nuclear reaction when 12C is the atom target [28].

In the context of particle physics and nuclear reactions, the concept of microscopic cross section refers to a measure of the probability that a specific interaction will occur between incident particles and a single atom of the target. Mathematically, it is represented as an effective area, which quantifies the likelihood of interaction based on the geometry of the scattering process, and can be calculated as follows [8]:

$$\sigma_e = \frac{Ni}{\varphi \times N1}, [cm^2 \; or \; m^2] \tag{7}$$

Where Ni is the number of interactions, φ is the fluence of incident particles and N1 is the number of target particles per unit of area.

The factors that influence a macroscopic cross section encompass both intrinsic properties of the interacting particles and the characteristics of the target medium. One primary factor is the energy of the incident particles; higher energy levels can increase the likelihood of interactions by overcoming potential barriers, thereby resulting in larger cross sections [8]. Additionally, the nature of the interaction plays a crucial role; for instance, strong interactions generally yield larger cross sections compared to weak interactions. The target material's atomic number and density also significantly affect a macroscopic cross section, as heavier and denser materials provide a greater number of target nuclei per unit volume, enhancing the probability of collisions [8]. Moreover, the angular distribution of scattered particles is relevant, as certain interactions may preferentially occur at specific angles, influencing the effective cross section observed in experiments. Using the microscopic cross-section showed in equation 7 and the characteristics described above, the macroscopic cross section can be calculated as:

$$\sigma = \frac{N_A \times \sigma_e \times \rho}{A} \tag{8}$$

Where N_A is the Avogadro's number, σ_e microscopic cross-section, ρ density of the medium and A is the atomic mass of the medium. The equation can be used to calculate the total cross section per unit length in the material, which represents the overall probability of an incident particle interacting with any atom within the medium over a path length of 1 cm.

The Janis books serve as a comprehensive compilation of cross-section curves derived from both evaluated and experimental data sourced from numerous libraries, covering a range of nuclear reactions and their associated products. Figure 7 presents an example of cross-section curves for proton-induced nuclear reactions on ^{16}O, extracted from the Janis compilation [29]. This library can be utilized for various elements, with the data exemplified in Figure 7 demonstrating the breadth of information available.

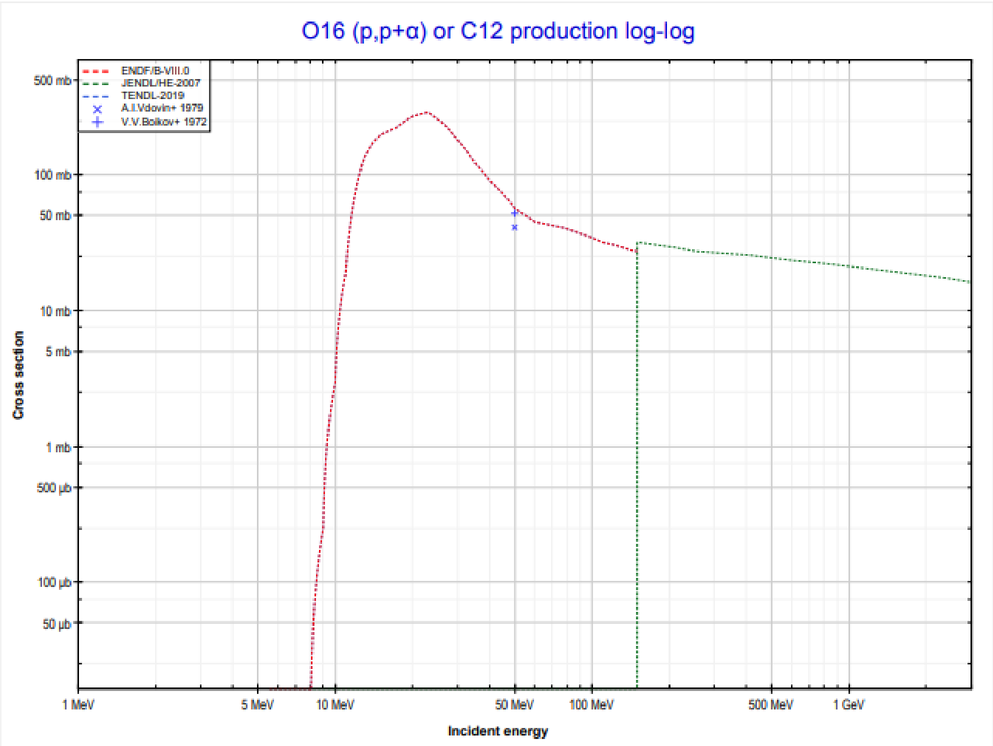

Figure 7 - Proton induced nuclear cross sections for C12 production comparison with different data tables and simulations [29].

That reaction is listed in table 3 because it creates a $^{12}C^*_{4.439}$ atom that release after few seconds a gamma-ray to get in a ground state. Is possible to see by the figure that the cross-section growths with incident energy until a certain peak, after that starts to slowly get down. The limit for this reaction to happens is the incident beam energy around 8 MeV, and as the therapeutic proton beam is losing energy during its path when this value of energy arrives this cross section goes to zero and no more $^{12}C^*_{4.439}$ gamma ray transition will be seen in the spectrum. Is important to notice that for each reaction this threshold is different as well as the curve behavior, therefore is expected to see different spectrums at different depths, once the reaction is more likely to occurs a certain depth value, for example the mentioned reaction get a higher probability of happen when the beam energy reach 30-40 MeV.

After the nuclear reaction the atom may be in an unstable state that means that it can reach for a more stable nuclear configuration, becoming then radioactive. Those process are [8]:

- Alpha (α) decay.
- Beta (β) decay.
- Gamma (γ) decay.
- Spontaneous fission (SF).
- Proton Emission (PE) decay.
- Neutron Emission (NE) decay.

2.2.1.4.1. Neutron Emission Decay: Emission of a neutron particle

Neutron emission is an important topic on heavy particles therapy, once some of the nuclear reactions induced by the beam undergo a neutron emission decay and those emitted neutrons get capture for other atoms, that reach an excited level and also emits gamma-ray photons [30]. The neutron-rich nucleus remains its atomic Z number the same, but the atomic mass number A decreases by 1.

$$ {}^{A}_{Z}P \rightarrow {}^{A-1}_{Z}D + n \tag{9}$$

Therefore, both the parent (P) and the daughter (D) are isotopes of the same nuclear species. This neutron emitted works an indirect radiation and as it goes through the absorber, they may undergo elastic and inelastic scattering as well as trigger nuclear reactions, such as neutron capture, spallation, and fission [4]. The probability for these different types of interaction depends on the kinect energy (E_k) of the neutron and the physical properties of the absorber nuclei atoms [8]. Neutrons interact mostly with the nuclei of the medium atoms, for being a neutral particle they are not suffer any interference from Coulomb repulsive and attractive force and they are classified by the kinect energy in several categories [8]:

1. Ultracold neutrons: $E_k < 2x10^{-7}\ eV$.
2. Very cold neutrons: $2x10^{-7}\ eV \leq E_k \leq 5x10^{-5}\ eV$
3. Cold neutrons: $5x10^{-7}\ eV \leq E_k \leq 0.025\ eV$
4. **Thermal Neutrons**: $E_k \approx 0.025\ eV$
5. **Epithermal Neutrons:** $1\ eV < E_k < 1\ keV$
6. Intermediate neutrons: $1\ keV < E_k < 0.1\ MeV$
7. Fast Neutrons: $E_k < 0.1\ MeV$

Only thermal Neutrons, Epithermal Neutrons and fast neutrons are used in medicine.

2.2.1.4.2. Neutron interaction with matter

There are five principal processes by which neutrons interact with the nuclei of the absorber [8]:

- Elastic Scattering: Neutron collides with a nucleus that recoils.
- Inelastic Scattering: Neutron is captured by the nucleus and re-emitted as neutron n' with lower energy and different direction.
- Neutron Capture: Nuclear reaction in which a thermal neutron bombards a nucleus and then there is an emission of a proton or gamma ray.

- Nuclear Spallation: Disintegration of a target nucleus into many small residual components.
- Nuclear fission: the target nucleus fragments into two daughter nuclei and this process is accompanied by production of several fast neutrons.

When talking about proton therapy there are only two ranges in neutron classification to be considered, the Thermal neutrons and the Epithermal neutrons. Those have two possible interactions with nuclei tissue that are important, because of its relatively high cross-section [30]. The first is the neutron capture by Nitrogen-14 ${}^{14}_{7}N(n,p){}^{14}_{6}C$ and the neutron capture by hydrogen-1 $({}^{1}_{1}H(n,\gamma){}^{2}_{1}H$. In the first reaction the neutron kinetic energy is divided between the proton and the carbon-14 nucleus, the protons will be able to go a short length once they are interacting with matter by Coulomb forces and depositing their energy locally [31]. The second reaction happens with a much large probability, once the cross section for this is bigger than the first one and the amount of hydrogen in tissue is higher than nitrogen [31]. In that case, a gamma ray photon is emitted with the energy equals the binding energy difference between a proton and a deuteron, neglecting the recoil energy of the deuteron is possible to assume that the energy of this photon is 2.225 MeV [5]. Therefore, neutrons produced by this reaction may also produce prompt gamma-rays but also delayed gamma rays.

2.2.2. Helium and Carbon Ion Therapy

As a heavy particle therapy, the helium and carbon beams have similarities when interacting with matter as the proton beam, however few differences make them more suitable for some cases other than proton therapy [14]. That been said the comparison between the proton therapy with carbon and helium will be made in this chapter to clarify those similarities and the differences.

To create the beams, the difference for those two particles will be the magnitude of the magnetic field, it has to be stronger, since the mass of carbon and helium ions are bigger than the proton’s.

2.2.2.1. Energy Loss rate (Linear Stopping Power)

Figure 8 shows the distinction of the Bragg peak for the different particles. Is important to note that to reach the same depth, the beam must have different rate energy/particle. A big ion atomic number (Z) means more protons on the atom nucleus, therefore more charge and consequentially it will face more Coulomb interactions. It will lead to a strong increase of the energy loss for heavier ions at the same velocity [31]. Protons are charged particles with$1,6x10^{-19}C$, comparing this with helium (2 protons) and carbon (6 protons) shows that the carbon ion beam has to have more energy to get at the same depth as protons and helium. At the Bragg peak the carbon beam has the highest energy deposition followed by the helium and then protons, it is an important fact once make them deposit the higher amount of energy on the wanted area.

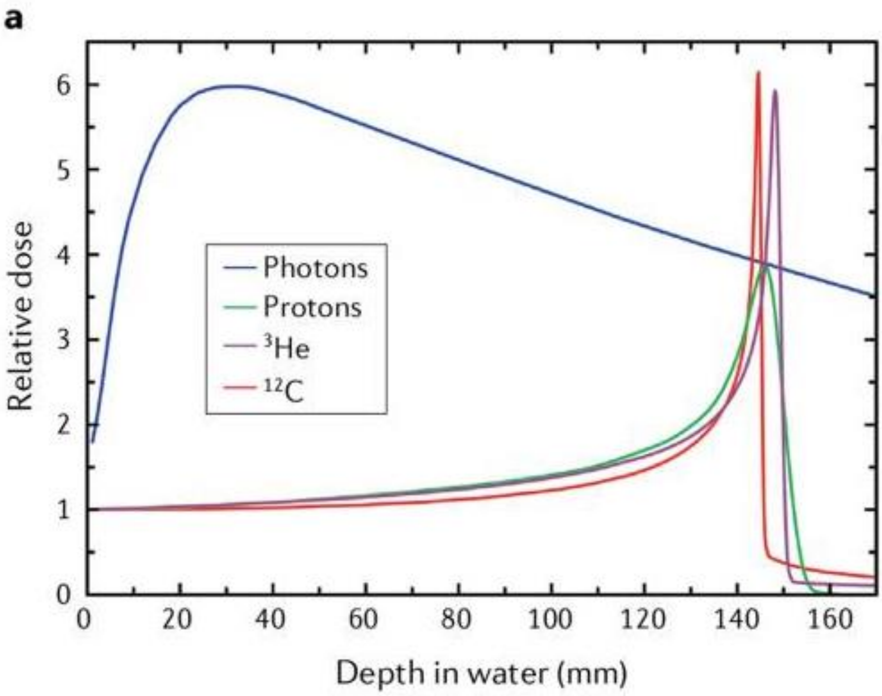

Figure 8 - Relative absorbed dose of high energy x-rays, protons Helium and carbons ions as a function of depth in water [14].

Combined with the fact that carbon has the lowers thick peak (order of few millimeters), giving this treatment the more precise energy deposition and making it spare surrounding healthy tissues [14]. Another difference is the tail created by the carbon that is not possible to see on protons beams. This phenomenon is caused by secondaries particles created by the inelastic nuclear collisions, and it brings a dose deposition after the Bragg peak that can be a problem in some treatments [14]. The helium beam stays at the middle ground between proton and carbon, as it has a thin peak as well, not as much as the carbon, but doesn't have the tail problem.

Figure 9 shows that at low energy, under 1 MeV, the biggest ions have higher stopping powers than protons, it makes the residual range of them smaller and therefore creating a thin energy deposition peak. This great difference results from the dependence of stopping power on the square of the charge of the particle. With the same velocity for example protons and helium beams will have a different stopping power by a factor of 4, i.e., $S_{he}\ (\beta) = 4.S_p(\beta)$ [8].

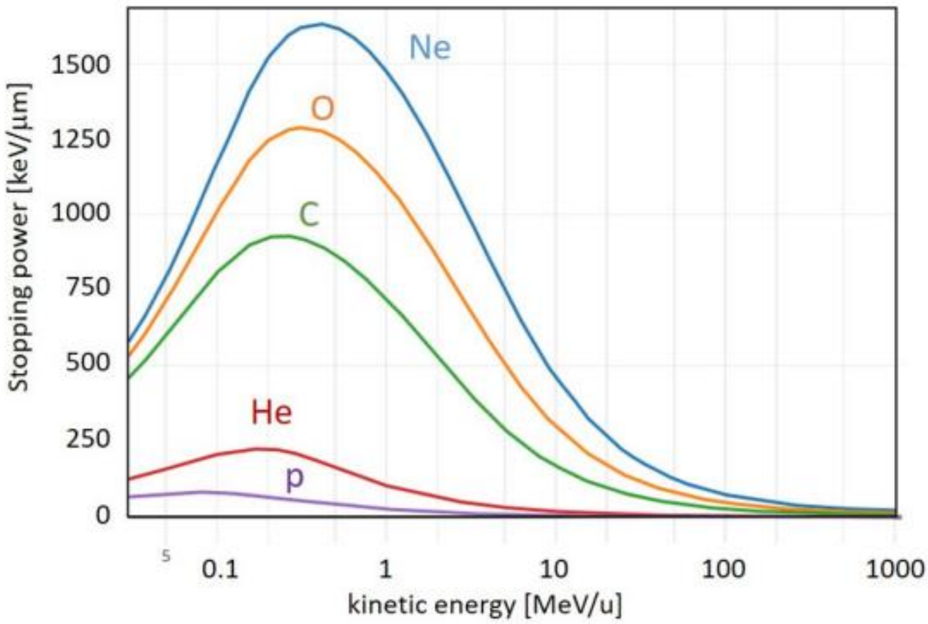

Figure 9 - Stopping power of different light ions as function of energy [31].

As those inelastic Coulomb interactions still occur with those two particles beams, the particle induced x-ray emission is also expected to happen, however not with the same magnitude, as the charge of the carbon and helium are different the probability of ionizing the medium is higher. Also, a consequence of the different stopping power factor is the equivalent dose (H) will be different from the particles.

2.2.2.2. CSDA Range

As mentioned above the range depends on the stopping power. Therefore, the range of the same energy Helium beams and carbon beams are going to be different from the proton beam once they have different stopping powers. Figure 10 shows the range correlation between the particles studied in this thesis.

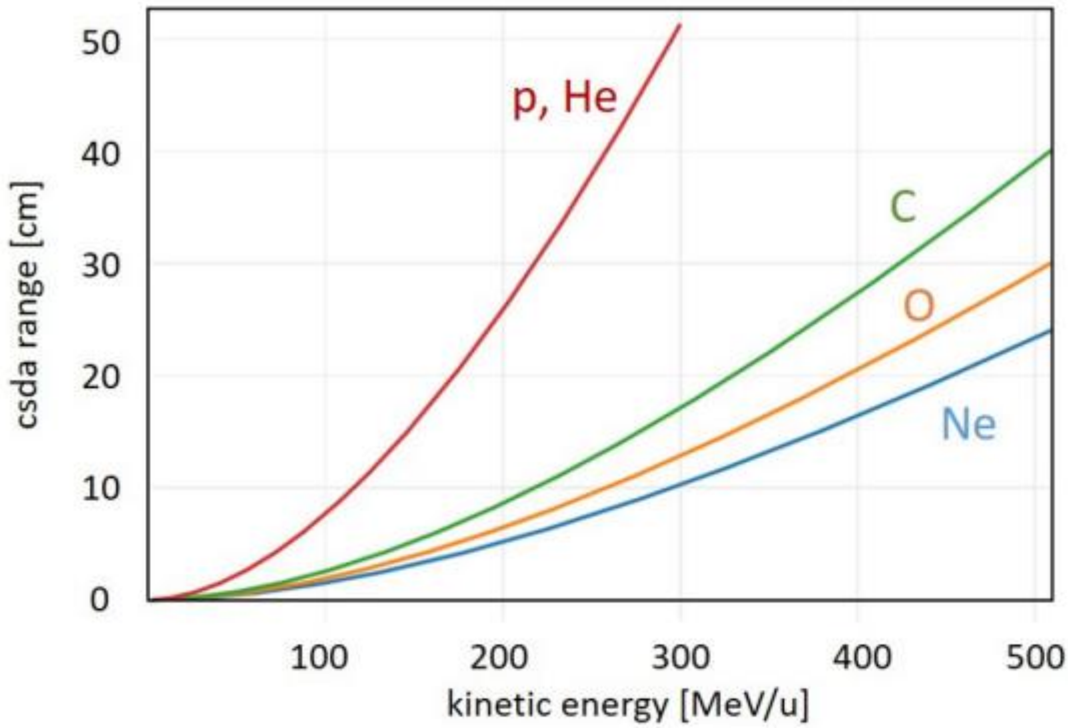

Figure 10 - Range of different ions in water as function of energy per nucleon [31].

Figure 10 shows that the range for protons and helium are the same, however this is an approximation, once that the range scales approximately with: $R \sim \frac{m}{Z^2}$, therefore the range for same energy protons (A = 1 , Z = 1) would be 1, and the helium (A = 3 , Z=2) , would be 0,75. And the carbon (A = 12, z=6) would have the 1/3 range compared to protons at the same energy [31]. As a consequence, when accelerating carbon ions, it would be necessary to deliver a three times higher initial energy per nucleus component to accomplish the same range as a proton beam. This results physically in the need for a significantly larger accelerator and in a simulation to multiply the energy of the proton beam by 12 to get the same range in carbon beams.

2.2.2.3. Nuclear reactions

In this context, protons can be classified as elementary particles. When a proton beam interacts with matter, the resulting nuclear reactions predominantly produce target fragments [4]. However, interactions involving helium and carbon nuclei can disrupt the binding forces between nucleons, leading to the generation of nuclear fragments from both the projectile and the target nucleus [12]. Due to the principles of conservation of momentum and energy, heavier fragments produced in these interactions exhibit lower energy and momentum compared to lighter fragments. Consequently, the secondary particle spectrum resulting from proton beam interactions is primarily composed of secondary protons, neutrons, and a limited number of heavier fragments, such as deuterons, tritons, and helium nuclei [31]. For heavier ions, projectile fragmentation significantly influences the resulting spectrum. This occurs because the projectile fragments can maintain velocities comparable to those of the primary ion. For instance, a secondary proton generated in a carbon beam may exhibit a greater range than the primary ion itself [14]. This phenomenon accounts for the tail observed in the carbon ion percent depth dose (PDD) curve (see Figure 8) beyond the Bragg Peak. Secondary particles produced during this process can have atomic numbers up to that of the primary ions. In the case of a carbon ion, the fragmentation can yield protons, helium, lithium, beryllium, and boron [14]. Figure 11 illustrates the potential nucleon-nucleus reactions in proton therapy, where neutron production occurs, in contrast to nucleus-nucleus reactions in heavy ion therapy, which result in the formation of light fragments.

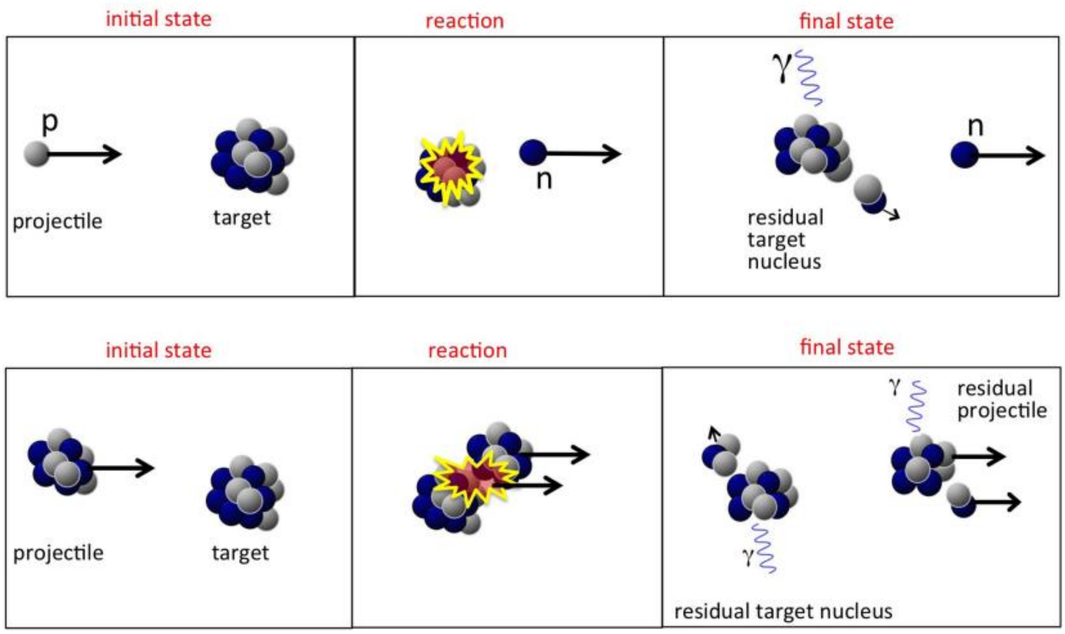

Figure 11 - Sketch of two possible nuclear reactions. Top: nucleon-nucleus. Bottom: Nucleus-Nucleus. Taken from [22].

Uncollimated experiments were realized by [26] to observe the de-excitation reactions caused by carbon and helium beams (figure 12). Those shows the prompt gamma lines that were observed in the spectrum of different ions beams. Is possible to see that most of the proton peaks appear on the carbon and helium beams with additional to some states that only can be seen at the heaviest particle spectrum. That means that the generation of secondary protons has enough energy to undergo a nuclear reaction with the target atom creating an excited state atom. It affects the spectrum once the emission of gamma and x-rays will be higher bringing a bigger fluence of photons created by the heavy particle’s interactions with the medium.

			Reactions induced by:		
E_γ [MeV]	Target nuclei	De-excitation reactions	p	^{4}He	^{12}C
6.1	^{16}O	$^{16}\text{O}^*_{6.13} \rightarrow {}^{16}\text{O}_{g.s.}$	✓	✓	✓
	^{16}O	$^{15}\text{O}^*_{6.18} \rightarrow {}^{15}\text{O}_{g.s.}$			
	^{16}O	$^{15}\text{O}^*_{5.18} \rightarrow {}^{15}\text{O}_{g.s.}$			
5.2	^{16}O	$^{15}\text{O}^*_{5.24} \rightarrow {}^{15}\text{O}_{g.s.}$	✓	✓	✓
	^{16}O	$^{15}\text{N}^*_{5.27} \rightarrow {}^{15}\text{N}_{g.s.}$			
	^{16}O	$^{15}\text{N}^*_{5.30} \rightarrow {}^{15}\text{N}_{g.s.}$			
	^{16}O	$^{12}\text{C}^*_{4.44} \rightarrow {}^{12}\text{C}_{g.s.}$			
4.4	^{16}O	$^{11}\text{B}^*_{4.45} \rightarrow {}^{11}\text{B}_{g.s.}$	✓	✓	✓
	^{12}C	$^{12}\text{C}^*_{4.44} \rightarrow {}^{12}\text{C}_{g.s.}$			
	^{12}C	$^{11}\text{B}^*_{4.45} \rightarrow {}^{11}\text{B}_{g.s.}$			
3.68	^{16}O	$^{13}\text{C}^*_{3.68} \rightarrow {}^{13}\text{C}_{g.s.}$	×	✓	✓
	^{12}C	$^{13}\text{C}^*_{3.68} \rightarrow {}^{13}\text{C}_{g.s.}$			
3.21	^{16}O	$^{12}\text{C}^*_{7.65} \rightarrow {}^{12}\text{C}^*_{4.44}$	×	✓	✓
	^{12}C	$^{12}\text{C}^*_{7.65} \rightarrow {}^{12}\text{C}^*_{4.44}$			
	^{16}O	$^{16}\text{O}^*_{8.87} \rightarrow {}^{16}\text{O}^*_{6.13}$			
	^{16}O	$^{14}\text{N}^*_{5.11} \rightarrow {}^{14}\text{N}^*_{2.31}$			
2.7	^{16}O	$^{11}\text{C}^*_{4.80} \rightarrow {}^{11}\text{C}^*_{2.00}$	✓	✓	✓
	^{16}O	$^{10}\text{B}^*_{3.59} \rightarrow {}^{11}\text{B}^*_{0.718}$			
	^{12}C	$^{11}\text{C}^*_{4.80} \rightarrow {}^{11}\text{C}^*_{2.00}$			
	^{12}C	$^{10}\text{B}^*_{3.59} \rightarrow {}^{10}\text{B}^*_{0.718}$			
2.31	^{16}O	$^{14}\text{N}^*_{2.31} \rightarrow {}^{14}\text{N}_{g.s.}$	✓	✓	✓
2.12	^{12}C	$^{11}\text{B}^*_{2.12} \rightarrow {}^{11}\text{B}_{g.s.}$	✓	✓	✓
	^{16}O	$^{11}\text{C}^*_{2.00} \rightarrow {}^{11}\text{C}_{g.s.}$			
2.0	^{16}O	$^{15}\text{O}^*_{7.28} \rightarrow {}^{15}\text{O}^*_{5.24}$	✓	✓	✓
	^{12}C	$^{11}\text{C}^*_{2.00} \rightarrow {}^{11}\text{C}_{g.s.}$			
1.88	^{16}O	$^{15}\text{N}^*_{7.16} \rightarrow {}^{15}\text{N}^*_{5.27}$	✓*	✓	✓
	^{12}C	$^{15}\text{N}^*_{7.16} \rightarrow {}^{15}\text{N}^*_{5.27}$			
1.64	^{16}O	$^{14}\text{N}^*_{3.95} \rightarrow {}^{14}\text{N}^*_{2.31}$	✓	✓	✓
	^{12}C	$^{14}\text{N}^*_{3.95} \rightarrow {}^{14}\text{N}^*_{2.31}$			
1.38	^{16}O	$^{15}\text{O}^*_{7.56} \rightarrow {}^{15}\text{O}^*_{6.18}$	✓*	✓	✓
	^{12}C	$^{15}\text{O}^*_{7.56} \rightarrow {}^{15}\text{O}^*_{6.18}$			
		$^{46}\text{Ti}^*_{3.29} \rightarrow {}^{46}\text{Ti}^*_{2.01}$			
1.3	^{48}Ti	$^{47}\text{Ti}^*_{1.44} \rightarrow {}^{47}\text{Ti}^*_{0.159}$	✓	✓	✓
		$^{48}\text{Ti}^*_{2.29} \rightarrow {}^{48}\text{Ti}^*_{0.983}$			
1.1	^{48}Ti	$^{46}\text{Ti}^*_{2.01} \rightarrow {}^{46}\text{Ti}^*_{0.889}$	✓	✓	✓
		$^{47}\text{Ti}^*_{1.25} \rightarrow {}^{47}\text{Ti}^*_{0.159}$			
1.02	^{16}O	$^{10}\text{B}^*_{1.74} \rightarrow {}^{10}\text{B}^*_{0.718}$	✓	✓	✓
	^{12}C	$^{10}\text{B}^*_{1.74} \rightarrow {}^{10}\text{B}^*_{0.718}$			
0.937	^{16}O	$^{18}\text{F}^*_{0.937} \rightarrow {}^{18}\text{F}_{g.s.}$	×	×	✓
0.983	^{48}Ti	$^{48}\text{Ti}^*_{0.938} \rightarrow {}^{48}\text{Ti}_{g.s.}$	✓	✓	✓
0.889	^{48}Ti	$^{46}\text{Ti}^*_{0.889} \rightarrow {}^{46}\text{Ti}_{g.s.}$	✓	✓	✓
0.718	^{16}O	$^{10}\text{B}^*_{0.718} \rightarrow {}^{10}\text{B}_{g.s.}$	✓	✓	✓
	^{12}C	$^{10}\text{B}^*_{0.718} \rightarrow {}^{10}\text{B}_{g.s.}$			

Figure 12 - Multiple de-excitation reactions for different ion beams [26].

2.3. Dosimetry

Dosimetry in radiotherapy is a critical field focused on the precise measurement, calculation, and assessment of the ionizing radiation doses administered to patients undergoing cancer treatment [8]. This discipline ensures that the prescribed dose is accurately delivered to the zone of interest while minimizing exposure to surrounding healthy tissues. Advanced techniques and sophisticated instruments, such as ionization chambers, thermoluminescent dosimeters, and modern software, are employed to measure and verify the dose distribution [32]. Accurate dosimetry is essential for optimizing treatment efficacy, enhancing patient safety, and improving clinical outcomes in radiotherapy. The use of ionizing radiation in medicine requires the capability of measuring accurately the quantity and quality of radiation produced by a source, natural or radiation-producing machine. There are many physical quantities that are determined by a radiation dosimetry process, among them there are radiation source activity, beam fluency, air Kerma, however, the principal is absorbed dose, imparted or to an absorber [32].

Radiation dosimetry is mainly divided into two categories, absolute dosimetry and reference dosimetry. The first refers to measurements of radiation dose directly without requiring calibration in a known radiation field. The most used absolute dosimeter is a calorimeter that works with the amount of heat created by the radiation and converse it dose [32]. Relative dosimetry is based on dosimeters that require calibration of their signal in a known radiation field. The gold standard for it is the ionization chambers. They are calibrated in the primary laboratory and then go to different places with a conventional factor used to calculate the correct dose of different beams. There is also another kind of technique, called In vivo Dosimetry. It refers to the direct measurement of radiation doses received by patients during radiotherapy, providing real-time verification of the delivered dose [33]. This technique involves placing dosimeters on or within the patient’s body, allowing for immediate assessment and correction of any discrepancies between the planned and actual doses. Methods such as thermoluminescent dosimeters (TLDs), diodes, and electronic portal imaging devices (EPIDs) are commonly used. In vivo dosimetry enhances treatment accuracy by identifying and compensating for variations caused by patient movement, anatomical changes, or equipment errors, thus ensuring the prescribed dose is accurately delivered to the target area while protecting healthy tissues.

A scintillator is also a detector with potentially capacity of doing in vivo dosimetry, it has a sensitive area made of a material that can interact with x-ray and γ-ray photons emitted from the target when irradiated. Those interaction are divided in five types [8]:

- Compton effect
- Photoelectric Effect

- Pair production
- Rayleigh scattering
- Photonuclear interactions.

The last two interactions are less important for the detector used in this work, Rayleigh scattering only redirects the photons through a small angle with no energy loss, and it means that the detector won't acknowledge its presence. Photonuclear interactions are significant for photons energy above few MeV, it could be important to detect prompt gamma rays created by the atoms in the organic tissue interactions with the particle beam. As a result of the transfer of energy generated by the first 3 interactions makes them the most important to the detector in this work. The importance of those effects depends on the medium atomic number as well as the energy of the incident photon, and it is shown in figure 13 [8].

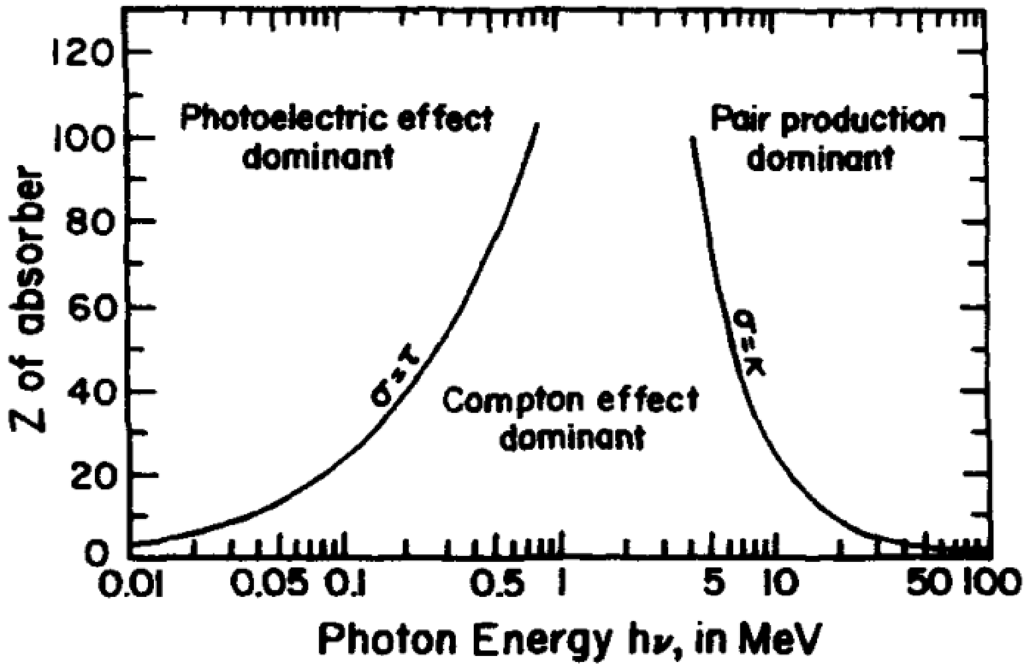

Figure 13 - Relative importance of the three major types of gamma-ray interactions [8].

When a photon goes through a medium it experiences exponential attenuation, caused by the interactions cited above. The attenuation is defined by [8]:

$$\frac{N_a}{N_b} = e^{-\mu . L} \tag{10}$$

Where N_a is the number of photons after the attenuation, N_b is the number of photons before, L is the length of the material thickness and μ is the linear attenuation coefficient that when divided by the material density turn into the mass-attenuation coefficient measured in $^{cm^2}/_{g}$. That equation represents an approximation on the process once it considers a narrow monoenergetic beam. The total mass- attenuation coefficient is a sum of the contributions from the different interactions processes, therefore $= \mu_{phot.E} + \mu_{comp} + \mu_{pair} + \mu_{Rs} + \mu_{N.I}$ [8]. It shows that the atomic number and the energy of the photons will impact directly which process is the most predominant and which will happen with higher probability. As the detector will use those interactions to count the particles in it, the geometry of the beam will not be a problem to consider.

2.4. Gadolinium (G_d)

Gadolinium, a rare earth element, holds a pivotal role in both physics and medicine due to its unique properties. Within the realm of physics, gadolinium possesses magnetic characteristics, making it a vital component in the construction of various magnetic materials and devices, such as magnetic resonance imaging (MRI) machines [34]. In medicine, gadolinium is most used in enhancing the quality of MRI scans. When administered as a contrast agent, the ion Gd^{3+} interact strongly with the main magnetic field, shortening the tissue relaxation times (t1 and t2), it improves the visibility of internal structures and abnormalities within the body during imaging procedures [35]. This enhancement enables healthcare professionals to accurately diagnose and monitor a wide array of medical conditions, ranging from tumors and vascular abnormalities to neurological disorders. One of the key advantages of gadolinium-based contrast agents is their relatively low toxicity and high biocompatibility, making them safe for use in medical treatments ang imaging [34].

Natural Gadolinium (**^{Nat}Gd**) has seven stable isotopes described in the table 4 along with your percentage composition [3].

Isotope	Percentage in ^{Nat}Gd
^{152}Gd	0.2%
^{154}Gd	2.18%
^{155}Gd	14.8%
^{156}Gd	20.47%
^{157}Gd	15.65%
^{158}Gd	24.84%
^{160}Gd	21.86%

Table 4 - Natural Gadolinium composition [3].

In the field of nuclear medicine this element is used in the one of the emerging concepts, the theragnostic approach. One of the most interesting elements for this field is the Terbium (Tb), which offers a several radionuclides with suitable characteristic for medical applications (^{149}Tb, ^{152}Tb, ^{155}Tb, ^{161}Tb) [36]. Those elements can be acquired by proton bombardment on natural Gd. Those proton inducted reactions are most of them either $^{x}Gd(p$,Zn)P or $^{x}Gd(p,\gamma)P$, where x represent the atomic mass of the gadolinium isotope, Z is a natural number from 1 to 9 and P is the representation of the Isotope created after the reaction [37]. Is important to notice that the first reaction produces neutrons that will be released and most likely interact again, creating new reactions in the medium. There are two of those reactions caused by that free neutrons that have extremely high thermal neutron capture cross sections, ^{155}Gd$(n,\gamma)^{156}$Gd* and ^{157}Gd$(n,\gamma)^{158}$Gd* [38], respectively 60900 and 254000 barns, it represents nearly 99.99% of the elemental cross section for this neutron range of energy [39]. It means that they have high probability of occurring when gadolinium (^{Nat}Gd) is being bombard with free thermal neutrons (E=0.025ev). Those excited states decay by prompt gamma ray emission to their stable state's isotopes. The prompt gamma rays emitted in these reactions will be showing as peaks at the irritation spectrum of gadolinium. The peaks from that reactions will have most of the values on 43, 88.97, 199.21 keV 79.5132 and 181.943 keV [40] [41]. Therefore, the spectrum of ^{Nat}Gd, showed in figure 14, when irradiate by heavy particles is expected to have those gammas-rays' energies and also the characteristic x-ray lines from the element among the other peaks from the same reactions on the different isotopes, however as the cross sections for those are not that relevant, those peaks in the spectrum will be low fluency.

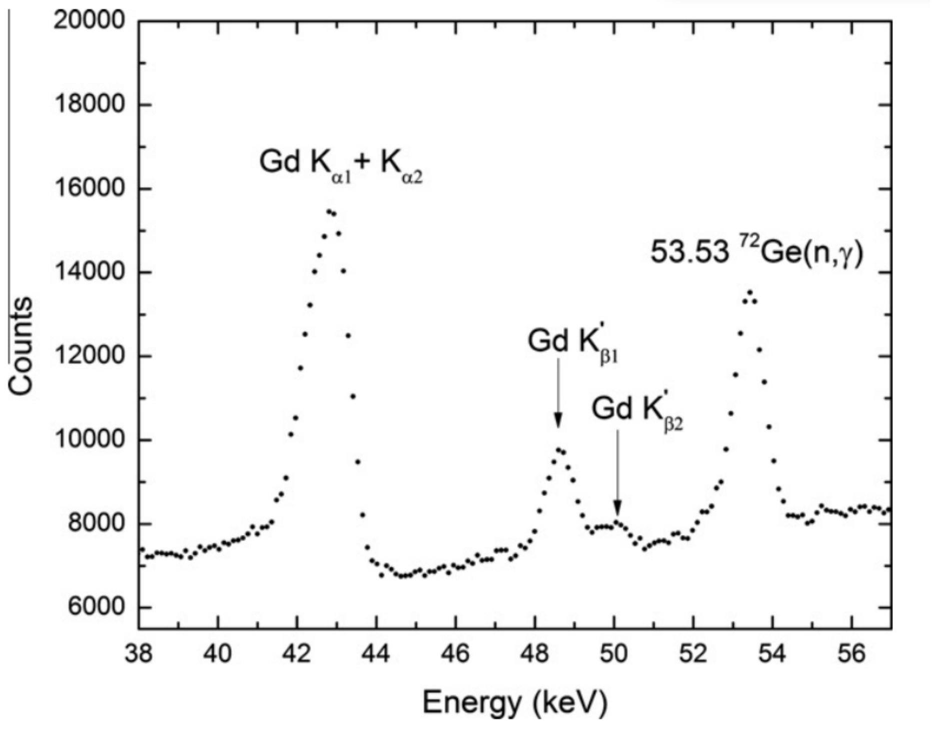

Figure 14 - A representative characteristic X-ray spectrum from Gd natural [39].

Figure 14 shows that the peaks of the characteristic x-ray of gadolinium spectrum are approximately 43 keV, 48.7 keV and 50 keV, representing the mean value of the $\alpha 1{,}2$ and $\beta 1{,}2{,}3$ transitions. Is also possible to see that the 43 keV peak has the highest fluence in the region, among other factors it can be explained by the fact that two processes are responsible for the appearance of those energy photons. When the heavy particles get through the medium, it removes electrons from the gadolinium atom, creating an excited atom that later will reorganize itself by moving an electron from an outer to an inner shell. At this process a photon is emitted to balance the energy in the atom [35]. The neutron capture made by the ^{155}Gd and ^{157}Gd also contributes to the characteristic x-ray production as this process creates Auger electrons through to the internal conversion, what makes the atom go through the same process as mentioned before [38]. Is possible to see in table 5 the most important neutron capture cross sections from the Gd^{Nat} atom along with the main spectral photon emission probabilities.

Isotope	Thermal neutrons capture cross section [b]		Photon emission energy [keV]	Photon Emission probabilities [%]
^{157}Gd	254000 ± 800	γ-ray	181.9	18.33 ± 1.69
		γ-ray	79.5	9.75 ± 0.69
		K_α	43	18.2 ± 1.0
		K_β	49	4.5 ± 0.3
^{155}Gd	60900 ± 500	K_α	43	29.1 ± 3.8
		K_β	49	7.1 ± 0.9

Table 5 - Photon Emission probabilities for the Gd isotopes interested in this study [38].

2.4.1. In Vivo Dosimetry with Gadolinium

As Gadolinium is an element with unique properties, among them it has the largest thermal neutron cross sections of all the stable elements. As seen before those neutron cross sections emit prompt-gammas that are specifically for Gd. It has been shown by J.L. GRAFE evidence that in vivo detection of gadolinium by prompt gamma neutron activation analysis is feasible, as detection limits agree concentrations previously assayed by biopsy measurements [42].

2.5. Monte Carlo Method

The Monte Carlo method is a computational technique that employs random sampling to solve mathematical problems [43]. The Monte Carlo method, named after the renowned Monte Carlo Casino in Monaco due to its reliance on random sampling akin to games of chance, is a sophisticated statistical technique used to approximate complex mathematical systems and phenomena [43]. This method involves simulating a substantial number of random samples, allowing statisticians to calculate probabilities and make predictions regarding various outcomes through repeated simulations. In the field of radiation physics, Monte Carlo simulations are crucial, particularly in radiation therapy, where precise dose delivery is essential [22]. These simulations meticulously model the transport of radiation particles through different media, accurately capturing their interactions with biological tissues and treatment devices [43]. This capability enables clinicians to design personalized treatment plans tailored to individual patient anatomies, thereby optimizing therapeutic outcomes while minimizing collateral damage to healthy tissues [39]. Moreover, Monte Carlo methods are vital in dosimetry and quality assurance (QA), ensuring the reliability and consistency of radiation dose delivery in clinical practice. They also facilitate the design of radiation shielding materials and configurations, significantly enhancing radiation safety in medical facilities and other environments where radiation exposure poses a risk. Overall, Monte Carlo simulations are indispensable tools in radiation therapy, equipping clinicians with precise dose calculations and enabling safer, more effective treatment strategies for patients undergoing radiotherapy [43].

From its entrance into a medium and it`s disappearance, a particle in contact with matter undergoes a series of random interactions. The individual probabilistic events that constitute a particle's history are simulated sequentially, and often in parallel, utilizing Monte Carlo methods [43]. These simulations rely on statistical sampling of the probability distributions that govern these events to accurately represent the overall phenomenon. The number of trials required to adequately characterize a particle beam traversing a medium, such as a water phantom or a patient, is typically substantial. This necessity underscores the importance of computational resources for performing these simulations. To ensure the randomness of events, the statistical sampling process employs pseudo-random number generation [38]. Consequently, to enhance the realism of Monte Carlo simulations, the program utilizes randomly sampled probability distributions derived from nuclear data to determine the outcome at each stage of the particle's lifecycle.

An illustrative example is presented in Figure 15, which depicts various random walks of particles. The program tracks the trajectory of numerous particles from their source until their termination in specific categories, such as absorption, escape, or annihilation.

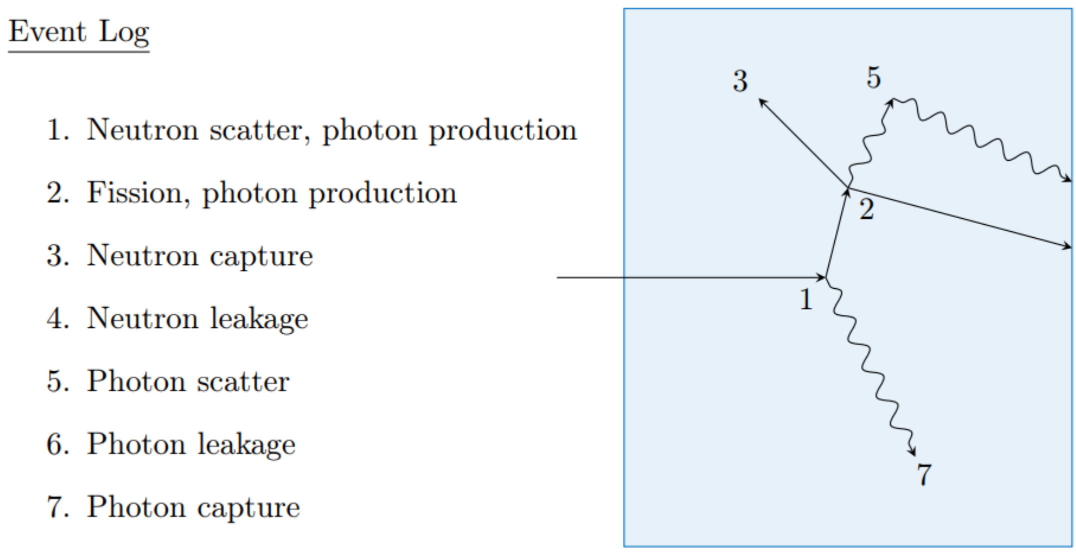

Figure 15 - Event log of a life particle throughout its life in a medium [43].

Figure 15 illustrates the trajectory of a neutron incident on a slab of fissile material. In the MCNP6 program, the neutron's path is modeled as a straight line. The program generates pseudo-random numbers between 0 and 1, which determine the nature and location of interactions based on the underlying physical principles and nuclear data that govern these processes [43]. In the example presented, the neutron initially undergoes fission, resulting in the emission of a secondary neutron and a photon. The numerical data associated with this process indicates that the photon's trajectory is recorded for subsequent analysis. The program continues to track the history of the particles throughout their interactions. Once all relevant events are generated, the neutron's history is considered complete. This process is repeated for a large number of particles, each exhibiting distinct interaction histories. Some particles may share similar histories, while others may diverge significantly [43]. As more histories are analyzed, the distributions of neutrons and photons become increasingly well-defined [43].Consequently, the quantities of interest specified by the user are computed along with estimates of statistical precision (uncertainty) regarding the results. However, it is important to note that simulating a larger number of particles requires more computational time, which may not always be feasible, especially when developing treatment plans for patients [38].

2.5.1. Monte Carlo Method vs Deterministic Method

The most common deterministic methods are the discrete ordinates ones, it means that they solve the transport equations for the average particle behavior getting the results typically missing information (for example flux) [43]. On the other hand, Monte Carlo methods simulate individuals' particles and record some aspects, solicited by the operator, of their average behavior. With this information, the average behavior of the many particles in the physical system is then inferred from the average behavior of the simulated particles using the Central limit Theorem [43]. Monte Carlo is suited to work on complicated three-dimensional, time-dependent problems, because it does not use phase space regions, there are no averaging approximations required in space, energy, and time [43].

2.5.2. MCNP Code

The MCNP (Monte Carlo N-Particle Transport Code) has a rich history in the field of nuclear engineering and radiation physics. Developed initially in the late 1960s by researchers at the Los Alamos National Laboratory, MCNP was designed to simulate the behavior of particles, such as neutrons, photons, and electrons, as they interact with matter [43]. Over the decades, MCNP has undergone numerous updates and enhancements, evolving into a powerful tool for a wide range of applications, including nuclear reactor design, radiation shielding, medical physics, and homeland security. Its robustness, accuracy, and versatility have made it a cornerstone in the toolkit of scientists and engineers working in the nuclear and radiation sciences [44]. The community's high confidence in the MCNP code's predictive capabilities is based on its performance with verification and validation test suites, comparisons to its predecessor codes, underlying high quality nuclear and atomic databases, and significant use by its users across the world in hundreds of applications [45]. The code is a general-purpose, continuous-energy, generalized-geometry, time dependent code designed on your latest version to track 37 particle types over a broad range of energies [43]. It is currently written using a mixed Fortran/C/C++ programming paradigm. The user creates an MCNP input file containing information about the problem in areas such as:

- Geometry Specifications.
- The description of material and selection of cross-sections evaluations.
- Location and characteristics of the source.
- The type of answers or tallies desired.
- Any variance reduction techniques used to improve efficiency.

In the realm of developing and executing Monte Carlo particle transport calculations, five fundamental principles serve as guiding lights [43]. These principles become increasingly significant with familiarity of the MCNP code. Regardless of expertise, these points should always remain at the forefront: Firstly, meticulous definition and sampling of geometry and sources are paramount. Secondly, once information is lost, it cannot be regained. Thirdly, scrutinize the statistical convergence, stability, and reliability of results. Fourthly, exercise caution in implementing variance reduction techniques, erring on the side of conservatism. Lastly, the quantity of histories run does not necessarily correlate with the accuracy or quality of the obtained solution. These principles, when upheld, contribute to the integrity and precision of Monte Carlo simulations.

2.5.2.1. Nuclear Data and Reactions

The MCNP code package has in its general features nuclear data tables that are used to calculate the probability of reactions to occur. The proper way MCNP code uses this data table is described in the next session 1.3.3.2. Physics.

According to the MCNP6 theory manual, there are ten classes of data tables on MCNP[46]:

- Continuous-energy neutron interactions data.
- Discrete reaction neutron interaction data.
- Continuous-energy photoatomic interaction data.
- Continuous-energy photonuclear interaction data.
- Neutron dosimetry cross sections

- Neutron S(α, β) thermal data.
- Multigroup neutron, coupled neutron/photon, and charged particles masquerading as neutrons.
- Multigroup photon.
- Electron interaction data
- Charged particle interaction data.

Choosing different data tables in MCNP can significantly impact the accuracy and reliability of the simulation results. The choice of data tables affects how the code models the interactions of particles with matter, including scattering, absorption, and other nuclear processes [43]. For example, selecting different nuclear cross-section data libraries, such as ENDF/B, JEFF, or JENDL, can lead to variations in the calculated neutron flux, reaction rates, and energy deposition. Similarly, using different atomic data tables may influence the handling of photon interactions, affecting dose calculations and radiation transport [46]. Therefore, the selection of appropriate data tables should be made based on the specific requirements of the problem being simulated and the desired level of accuracy. Additionally, is possible to see that limitations and uncertainties are associated with different data libraries [46] what makes the users have caution when interpreting the results obtained with them.

2.5.2.2. Physics

MCNP offers a comprehensive array of physics options that allow users to tailor simulations to their specific needs across diverse fields such as nuclear engineering, radiation protection, and medical physics [47]. These options encompass a wide range of phenomena, including neutron transport, photon transport, electron transport, and thermal scattering. By selecting appropriate physics models and parameters, users can accurately simulate particle interactions with matter, encompassing processes like elastic and inelastic scattering, nuclear reactions, radioactive decay, and electromagnetic interactions [47]. The importance of these physics options lies in their ability to capture the complex physical behavior of particles in various materials and environments. Moreover, they enable researchers and engineers to investigate critical aspects of radiation transport, such as shielding design, reactor analysis, radiation therapy optimization, and nuclear security applications [48]. Through the careful selection and utilization of physics options within MCNP, users can obtain reliable and insightful results crucial for advancing scientific understanding and practical applications in the realm of nuclear and radiation physics.

3. Methodology

This chapter outlines the methodology employed in this study to achieve the defined objectives. It will be divided according to the two objectives outlined in Section 3.4, with a focus on analyzing the variations in production associated with each.

3.1. Practical Dosimetry studies

In the first phase of this study, practical dosimetry assessments were conducted at Atrys Health Portugal – Advanced Medical Center, located in Santa Maria da Feira, Portugal (Atrys). The radiotherapy center at Atrys is equipped with two linear accelerators, and there it was possible to practice and understand the clinical and dosimetry requirements for X-ray beams applications. The usage of water phantoms and ionization chambers enabled the measurement of percentage depth dose, dose profiles and output factors for photon and electron beams.

3.2. Experimental Setup

Located in Germany, the Heidelberg Ion-Beam Therapy Center (HIT) (Figure 16) has facilities for treating patients with low-LET modalities, such as proton and helium ion beams, as well as high-LET modalities, including carbon and oxygen ion beams.

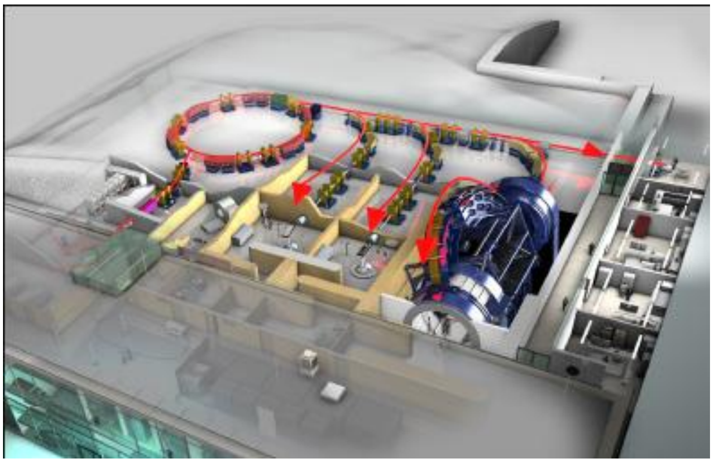

Figure 16 - HIT treatment facility 3D scheme. Source: https://www.klinikum.uni-heidelberg.de/

The ion beam process begins with a two-stage linear accelerator, which accelerates ions to 12% of the speed of light before they enter the synchrotron. The synchrotron consists of six 60º magnets that bend the ion beams into a circular path. Over approximately one million orbits, the ions are accelerated to 75% of the speed of light. To direct the beam into treatment rooms, additional magnets guide it through vacuum tubes. Some treatment rooms feature a fixed beam direction, while another room includes a gantry that allows the beam to move. In the upper-right corner of Figure 16, a dedicated experimental room for beam testing is visible.

An experimental setup was built in the testing room using two different detectors, as shown in Figure 17. Three different ion beams were used to irradiate a flask containing $Dotarem^{(R)}$, a Gd-based contrast agent. This compound consists of 280mg of Gadoteric acid ($C_{23}H_{42}GdN_5O_{23}$) with a density of 1.74 g/cm^3 and 850mg of H_2O with a density of 1.0 g/cm^3, all held in a flask measuring 40 mm in length and 31.5 mm in radius. The particles used for irradiation included Protons with an energy of 51.8 MeV/u, Helium at 51.8 MeV/u, and Carbon at 95.7 MeV/u. The flask was positioned 100 cm from the beam source, while the detectors were placed 25 cm from the flask at a 90º angle relative to the beam source.

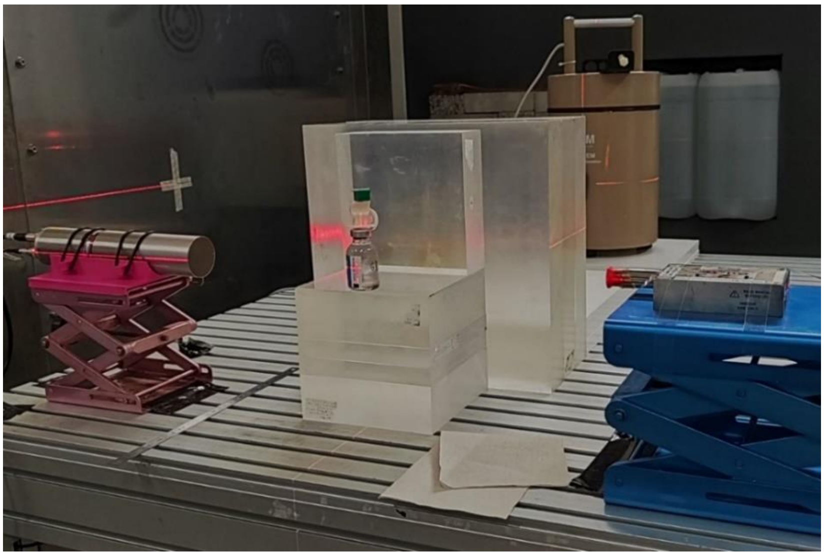

Figure 17 - Experimental Setup. On the Left the Cerium Bromide Detector at the center the Dotarem.

In enable comparison of the spectra, a bottle of pure water (H_2O) was also used as a target in a subsequent irradiation. Table 6 summarizes the irradiation procedures.

Particle	Energy [MeV/u]	Intensity [Particles/s]	Time of irradiation [s]	Focus [mm]	Flask
1H	51.8	8.00×10^7	150	30.7	Gadolinium
1H	51.8	8.00×10^7	150	30.7	Water
4He	51.8	2.00×10^7	250	18.2	Gadolinium
4He	51.8	2.00×10^7	250	18.2	Water
12C	95.7	2.00×10^7	250	9.3	Gadolinium
12C	95.7	2.00×10^7	250	9.3	Water

Table 6 – Total of irradiations performed at the HIT institute.

3.2.1. Detectors

To detect the photon produced by the $Dotarem^{(R)}$ and water, two different detectors were used: a scintillator and semiconductor diode.
The scintillator operates primarily through a crystal in its sensitive area that interacts with incoming radiation [49]. When radiation interacts with the crystal, its atoms absorb energy, causing an electron to transition from the valence band to the conduction band and create an electron-hole pair. This excited state is unstable, leading to de-excitation and the emission of a low-energy photon by the atom. The choice of scintillator crystal is critical, as it depends on the type and energy of the radiation being detected. The crystal properties influence the cross-sections of interactions, thereby determining the detector's absolute efficiency for the experiment [49].
Once light photons are produced, they reach the scintillator's photocathode, a material capable of undergoing the photoelectric effect. As photons strike the photocathode, they emit photoelectrons, which are then amplified by a photomultiplier tube (PMT) to generate the final signal (Figure 18).

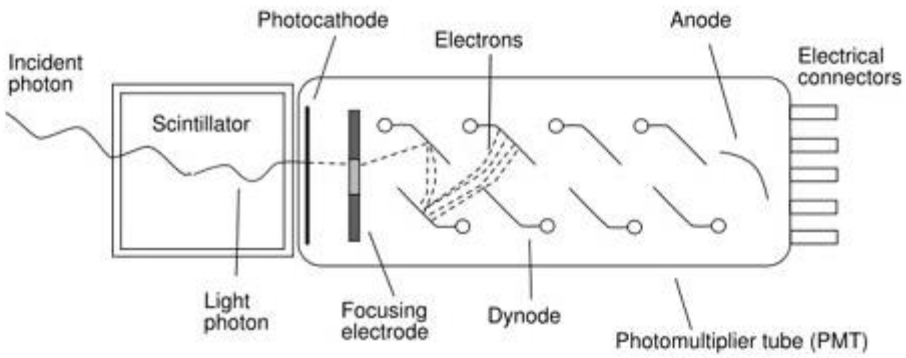

Figure 18 - Schematic diagram of a scintillation detector along with the photomultiplier tube (PMT) data from: web.stanford.edu/groups/scintillators/scintillators.html, accessed 15/07/2024.

3.2.1.1. Cerium Bromide ($CeBr_3$) Scintillator

The aim of this work is to investigate the low-energy photons emitted by gadolinium and to assess the ability of a spectrometer to detect these photons. This ability depends on several factors: energy resolution, detection efficiency, and the presence of interfering background noise, which can originate from environmental sources or even the detector itself. Previous studies have examined the energy resolution of Cerium Bromide ($CeBr_3$) scintillators in comparison with other detectors for low-energy photons, revealing that $CeBr_3$ has a significant advantage in detecting low-intensity emissions. [49].

$CeBr_3$ is a crystal known for its relatively high density and proportional response to gamma radiation. It features a fast light pulse rise time, enabling the detector to provide sub-nanosecond time resolution. Additionally, the material exhibits a fast decay time on the order of 20 ns.

The $CeBr_3$ crystal scintillator used in the experiment has a cylindrical shape with a diameter of 3.81 cm and length 7.62 cm length and is protect by an aluminum casing. As shown in figure 17, the detector was positioned at a 90º angle from the beam direction, facing the $Dotarem^{(R)}$ flask at a distance of 25 cm.

3.3. Experimental Results

The irradiations detailed in Table 6 resulted in a PGS spectra ranging from 35 keV to a maximum of 700 keV for every different irradiation (Figure 19). The purpose of irradiating water flask was to establish a reference spectrum for comparison with the $Dotarem^{(R)}$ spectrum. At the time of this study, only data from the $CeBr_3$ scintillator was available; therefore, the spectrum from the semiconductor diode is not presented or considered in this work.

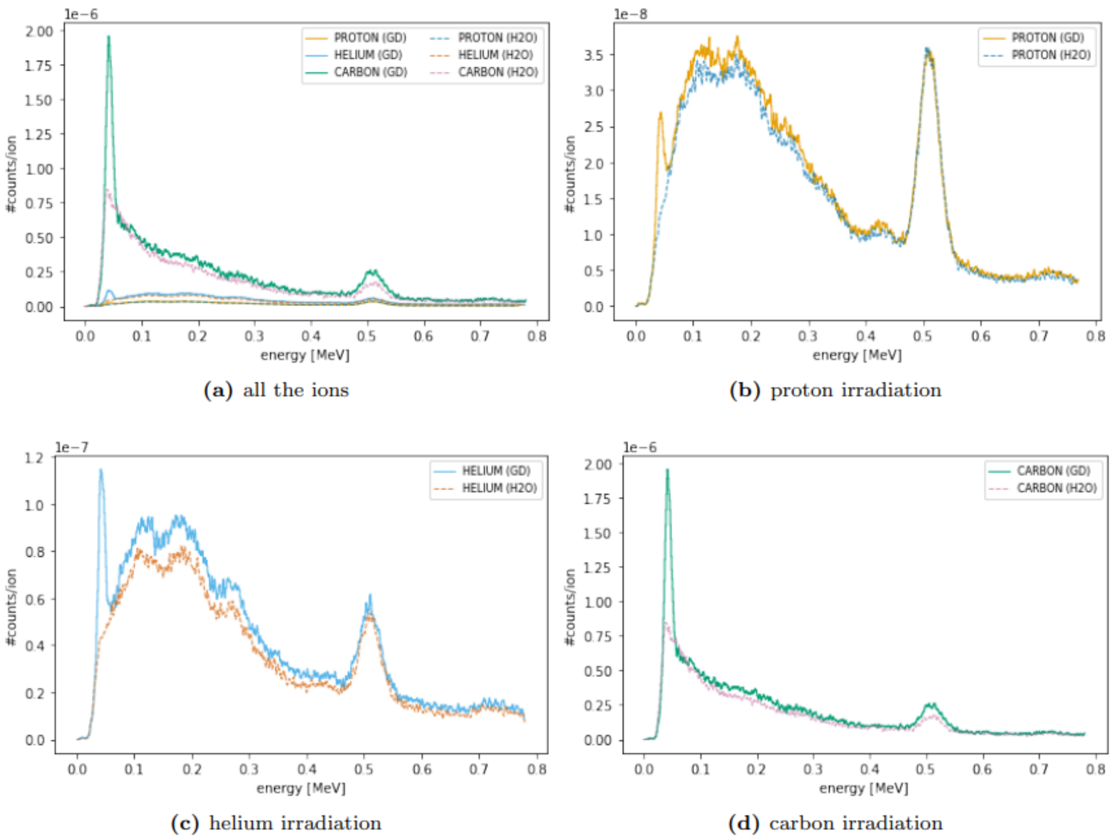

(a) all the ions (b) proton irradiation (c) helium irradiation (d) carbon irradiation

Figure 19 - Full range PGS spectra for proton, helium and carbon irradiation of a vial either filled with GD or water [50].

To obtain the plots shown in Figure 19, an analytical procedure was conducted on the GD signal, following the steps [50]:

1. Determination of a region of interest: In this case, the 43 keV peak region. This peak consists of the $Gd\ K_{\alpha 1}$ + $K_{\alpha 2}$ lines which contribute to the 43 keV single peak flux as well as the $Gd\ K_{\beta 1}$ + $K_{\beta 2}$ lines, which correspond to the 48 keV single peak flux (Figure 14)
2. Baseline restoration in the spectrum: After analyzing the background radiation, a baseline was established to distinguish the region of interest from the background (Figure 20).
3. Identifying the Peak and Fitting a Gaussian Curve: The next step involves locating the peak and fitting a Gaussian curve to it.
4. Analyzing the Gaussian Area: After fitting the curve, the area under the Gaussian was evaluated.

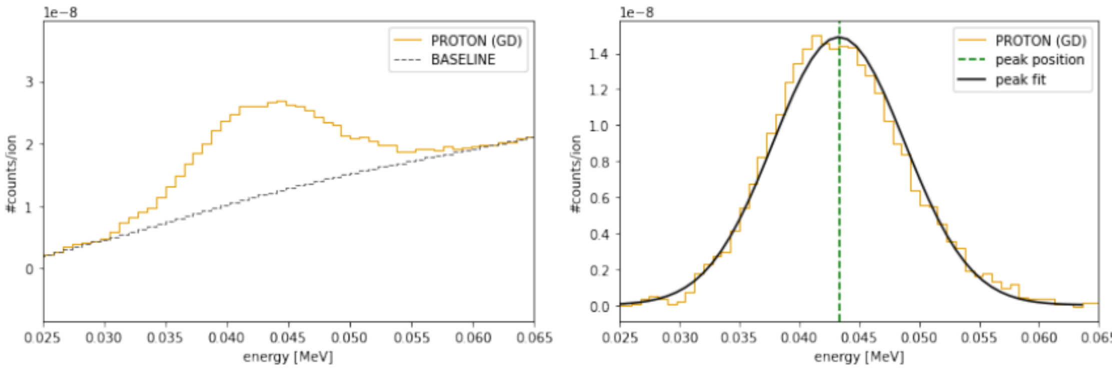

(a) ROI + baseline restoration (b) *Gaussian* fit

Figure 20 - PGS spectra of the steps used to quantify the GD peak. a: Selection of region of interest and baseline restoration. b: Gaussian fit to the GD peak and area determination [50].

The steps were applied to all ion spectra to compare the GD signals from each of them. Figure 21 displays the comparison of the measured region areas in particle counts (#) for each ion. Using the proton as a baseline, the Carbon exhibited approximately 100 times stronger GD signal, while the Helium showed about 5 times more strength.

Those areas were calculated after a filter was applied to the experimental data. To enhance the resolution of the results, this filter was used, resulting in smaller area values compared to the original data. The filter processes a percentage of the photon flux in each simulated graph area.

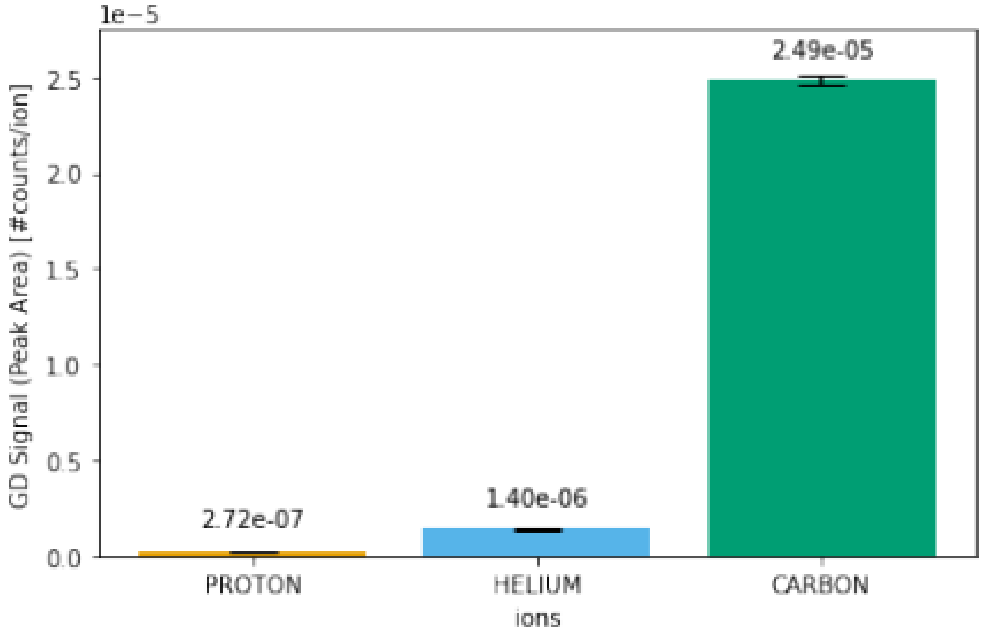

Figure 21 - GD signal as function of ion for irradiation of a vial filled with GD [50].

3.4. MCNP code

The MCNP code requires adaptation to fulfill specific objectives. Therefore, this chapter details all concepts incorporated into the code to elucidate particular phenomena and minimize simulation time. Additionally, many resources developed for the spectroscopic analysis of the 43 keV peak were also employed in the codes for comparing equivalent doses. However, it is important to note that some differences will be highlighted in this section.

3.4.1. 43 keV peak region spectrum MCNP code validation

The MCNP (Monte Carlo N-Particle Transport Code) software provides a range of physics models and variables that users can select to concentrate on specific phenomena of interest [47]. This capability is essential, as time is a critical resource in simulation processes. By modifying program parameters, users can disregard certain events to highlight others or to facilitate a more detailed examination of specific interactions.

The peak region at 43 keV arises from multiple processes. As previously noted, these photons are generated from the interaction of heavy ions with target medium atoms, a process known as Particle Induced X-ray Emission (PIXE) and the neutron capture. To ensure that the MCNP program adequately emphasizes these interactions, specific tools within the MCNP6 framework must be utilized.

3.4.1.1. Physics Model

Since the 43 keV peak region consists of photons produced through several steps, an internuclear cascade model is ideal for simulating the experiment. These models are essential for understanding the complex interactions that occur during high-energy collisions between nucleons and atomic nuclei. They simulate the sequential collisions and interactions of incoming particles, such as protons or neutrons, with nucleons within a target nucleus, resulting in the emission of secondary particles and the formation of residual nuclei.

By tracking the individual trajectories and interactions of particles, internuclear cascade models provide detailed insights into energy deposition, fragmentation processes, and particle yields [51]. This becomes particularly crucial when simulating helium and carbon ion beams, as the fragmentation process generates secondary particles that can also possess sufficient energy to induce new nuclear interactions, leading to the production of additional photons. This is reflected in the experimental results, which show a stronger signal for these ions compared to proton beams. These models enable researchers to predict and analyse the outcomes of nuclear reactions. Among the various physics models available in MCNP6, the Cascade-Excitation Model (CEM03.03) is the best option for this work, especially given the range of energies applied in the experiment [52]. Developed in response to increased interest in intermediate nuclear reactions, the CEM code calculates nuclear reactions induced solely by nucleons, pions, and photons, specifically at incident energies below approximately 5 GeV [51]. The model assumes that nuclear reactions occur generally in two stages:

- **First Stage: Intra-Nuclear Cascade (INC)**: Primary particles can be re-scattered and produce secondary particles multiple times before they are absorbed by or escape from the nucleus. Once the cascade stage is complete, CEM03 generates high-energy deuterons, tritons, and helium, as applicable. It is essential for this work to note that the emitted cascade particles initiate their own histories. The model emits these particles and determines their configuration, including the atomic number (Z), mass number (A), and excitation energy.
- **Second Stage:** This stage begins when the atom is excited by the energy of the incident particle. If, after the Intra-Nuclear Cascade (INC), the atom has an atomic mass number (A) of 12 or less, the model employs the Fermi breakup model to calculate its subsequent disintegration. This approach is significantly faster, and yields results that closely resemble those obtained from more detailed models.

However, some inconsistencies were found in the Fermi breakup model when used with CEM03.02, particularly when the excitation energy of the fragments was below 3 MeV. The event generators could produce unstable products via very asymmetric fission. This issue was resolved with the release of version CEM03.03 [51]. A schematic outline of a nuclear reaction calculation using CEM03.03 is shown in Figure 22. The model has been verified and validated, demonstrating that MCNP6 describes various reactions induced by particles ranging from 18 MeV to about 1 TeV, measured on both thin and thick targets. Since the irradiation used in the experimental part was at energies of 51.5 MeV/u and 95.7 MeV/u, this model represents a good match for the simulation.

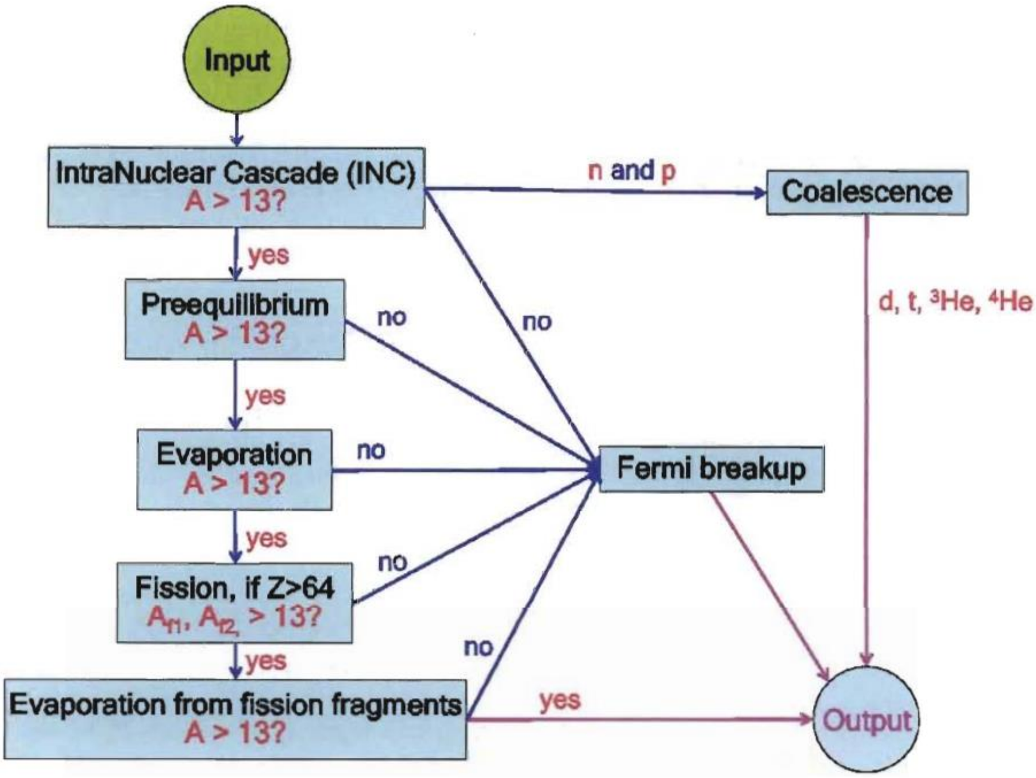

Figure 22 - Flow chart of nuclear-reaction calculations by CEM03.03 [53].

For proton irradiation, the CEM03.03 cascade model operates effectively and is the default physics model in MCNP6 [43]. The initial validation was conducted by comparing simulation results with experimental data and results from other software. Comparisons of the total cross-section and double differential energy spectra for neutrons, protons, and light fragments produced during proton irradiation show satisfactory agreement [37]. This is important for this work, as the neutrons generated will contribute to the production of 43 keV peak photons through interactions with gadolinium atoms. This indicates that the selected physics model has been verified as efficient for neutron production. Additionally, there is currently no published work addressing the production of PIXE during proton irradiation.

To simulate nucleus-nucleus interactions, CEM03.03 is not the best option because it does not consider the timing of interactions, specifically the so-called "trawling effect." [51]. When high-energy particles are used in radiotherapy, they can collide with the nuclei of atoms in the tissues. This interaction can cause secondary reactions, leading to the emission of secondary particles, such as neutrons or other nuclear fragments [54]. These secondary particles can travel some distance from the initial point of interaction and may interact with other nuclei in the surrounding tissues. This creates a "trawling" effect, where energy deposition and radiation damage are spread over a wider area than originally intended. This effect is particularly evident with Helium and Carbon beams, as the fragmentation of these ions can produce many more secondary particles than protons [54].
The Los Alamos version of the Quark-Gluon String Model, known as LAQGSM03.03, is a cascade model that accounts for fast cascade particles along with nucleon spectators from both the target and projectile nuclei [51]. This makes the model particularly useful for simulating heavier ions [22]. Figure 23 presents a plot of experimental data for a neutron spectrum compared with simulations using MCNP6 LAQGSM03.03 for a carbon beam. The agreement in neutron production for carbon beams establishes it as the best physics model for the two irradiators of the heaviest beams in this study [51].

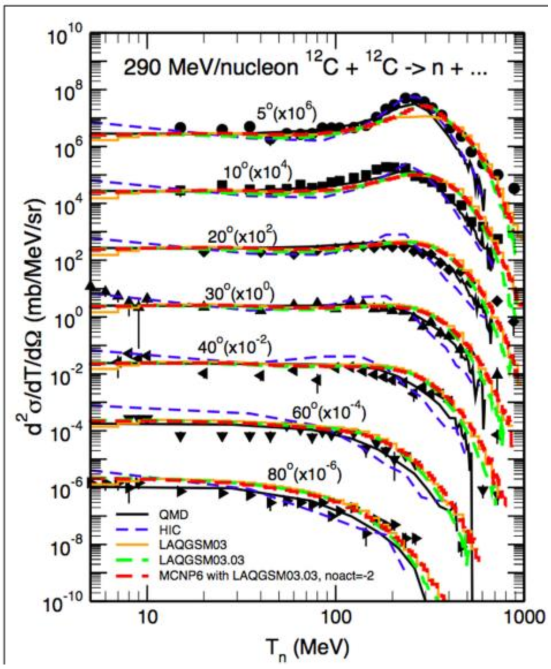

Figure 23 - 2D Neutron Spectra at different angles from a thin 12C target bombarded with 290 MeV/u 12C beam. taken from: [22].

3.4.1.2. Geometry

The geometry environment created in the MCNP6 code is shown in Figure 24. It represents the experimental setup and distances. The source is positioned along the y-axis, 100 cm away from the flask, which is bisected in the Z=0 plane.

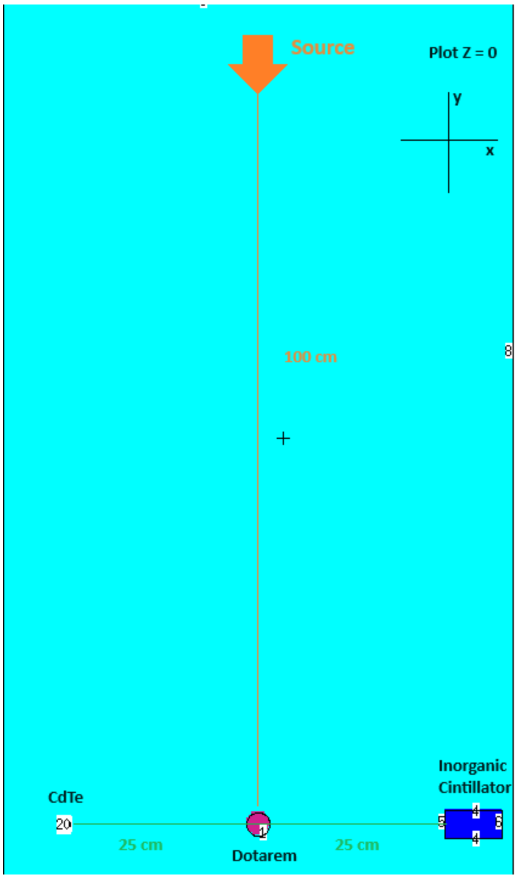

Figure 24 - MCNP6 output geometry file.

3.4.1.3. Materials

The $Dotarem^{(R)}$ is made of 280 mg of Gadoteric acid $C_{23}H_{42}Gd\ N_5O_{13}$ with 1.74 g/cm³ density and 850 mg of H_2O with 1,0 g/cm³ density. The isotopes fractions are already calculated by the MCNP6 code, using the atomic mass equals to 000, the program has in their libraries which percentage of each isotope is present in that natural atom, so the gadolinium atoms will follow the percentage of isotopes listed in table 4. To represent this molecule in the code the atom fraction of each atom present on it was used.

Considering that the total compound weights 1130 mg it has 24.78% of $Dotarem^{(R)}$ and 75.22% of water. The distribution of each atom is presented in table 7.

	Gadoteric acid molecule [%]	*Total compound [%]*
Carbon (Z=6)	**27.38**	**6.84**
Hydrogen (Z=1)	**50**	**62.5**
Gadolinium (Z=64)	**1.19**	**0.30**
Nitrogen (Z= 7)	**5.96**	**1.49**
Oxygen (Z= 8)	**15.47**	**28.87**

Table 7 - Percentage of $Dotarem^{(R)}$ compound.

The composition and density of the sensitive area of the detector play critical roles in determining the number of interactions that occur and the overall efficiency of the detector. Consequently, a meticulous calculation of the atomic fractions was performed. The scintillator material is cerium bromide ($CeBr_3$), composed of 25% cerium and 75% bromide. The composition and density of the flask material remain unknown; thus, this object was excluded from the simulations. As a result, the expected photon flux in the simulations is anticipated to be higher than that observed in the experimental setup, as the glass attenuates photons before they reach the detector. Given that the objective of this study is to compare the flux among proton, helium, and carbon beams, as illustrated in Figure 21, the absolute value of the flux is not critical for the comparison between the beams. However, it does provide insights into the limitations of the simulation regarding the phenomenon.
An approximation of the attenuation of the flask glass can be calculated using Equation 10 and data from the National Institute of Standards and Technology (NIST). Assuming the flask is constructed from Pyrex material, NIST reports a mass-attenuation coefficient of 0.39453 cm²/g for 43 keV photons and a density of 2.23 g/cm³. The thickness of the glass, measured using computed tomography (CT) images, is approximately 0.3 cm. Applying Equation 10 yields the following results:

$$\frac{N_a}{N_b} = e^{-0.39453\,.\;1.1\,.x\,2.23}$$

$$N_a = N_b\,.\,0{,}76$$

Approximately 76% of the photons in this energy range are expected to be attenuated. This estimate is an approximation derived from an equation that assumes a narrow beam configuration, which implies that secondary particles produced during photon interactions will not reach the detector located 25 cm away from the flask. The detector's sensitive area is relatively small compared to the range of the incident photons, thereby validating the assumption that secondary particles will not significantly contribute to the detected flux.
Another critical parameter is the mass-attenuation coefficient. In the calculations, only the value at 43 keV was utilized. However, it is important to note that the peak area spans from 37 keV to 50 keV. According to data from the National Institute of Standards and Technology (NIST), lower-energy photons experience greater attenuation due to their larger mass-attenuation coefficients.

Nevertheless, the contribution of these lower energy values to the peak region is relatively minor, thus using the 43 keV energy level provides a reasonable approximation of the actual attenuation behavior.

3.4.1.4. Source

All the beams used to irradiate the flask can be classified as charged particle beams. In this context, a Gaussian beam distribution is often employed to describe the beam due to various fundamental and practical reasons related to the physical and statistical properties of the beam [55]. The Central Limit Theorem (CLT) states that the sum of a large number of independent and identically distributed random variables tends to be normally distributed, regardless of the original distribution of those variables. For a particle beam, the position, momentum, and energy of individual particles can be influenced by numerous small, independent factors, such as random thermal motions, interactions with other particles, and imperfections in the beam-generating equipment. As these small random effects accumulate, the resulting distribution of particle positions, velocities, and energies will approximate a Gaussian distribution. Additionally, empirical observations and experiments frequently demonstrate that particle beams exhibit a Gaussian-like distribution in position, angle, energy, and other parameters [12].

As the fit of a Gaussian function to experimental data often provides a good approximation, has been validated the use of this model. To introduce this distribution in the beam source on MCNP6 has to be used the focus listed in the table number 6. Following the manual the density function of the position Gaussian distribution is defined by [43]:

$$p(x',y') = \left(e^{-\frac{\frac{1}{2}\left(\left(\frac{x'}{a}\right)^2 + \left(\frac{y'}{b}\right)^2\right)}{2\pi ab(1-exp\frac{(-c^2)}{2}}} \right) \tag{11}$$

The parameters a and b are the standard deviation of the Gaussian in x and y. That can be determined using the focus (full width at half-maximum - FWHM) by the following equations [43]:

$$Focus\ (x) = (8\ln 2)^{\frac{1}{2}}\, a = 2.35482. a \tag{12}$$

$$Focus\ (y) = (8\ln 2)^{\frac{1}{2}}\, b = 2.35482. b \tag{13}$$

By collecting the data for Table 6 and applying it, it is possible to create the Gaussian distribution. MCNP6 only requires the FWHM to generate it successfully.

3.4.1.5. Tally detector

For a photon to be detected by a scintillator or a diode, it must interact with the atoms present in the sensitive region of the detector. The probability of such interactions is influenced by several factors, including the photon's energy, the angle of incidence with respect to the detector surface, the interaction cross sections with the atoms in the medium, as well as the density and thickness of the sensitive area [49]. To achieve precise simulations of these interactions, the use of a pulse height tally is essential. This tally captures the energy deposited in a designated cell by each incident photon and its secondary particles, enabling a more accurate representation of the microscopic events that occur during the detection process [43]. Consequently, the energy bins of a pulse height tally reflect the total energy deposited in a cell bin by all associated particle tracks for a specific event history. The F8 tally, configured by energy bins, produces two key columns in its output file. The first column represents the number of particles that deposited a specified amount of energy as described in the beam. This value is expressed as the ratio of the number of photons that intersected the surface to the number of source particles simulated. The second column provides the relative error associated with the flux value [43]. The MCNP is used to perform repeated calculations of a problem, it can be combined using a batch-statistics approach. Considering *M* the number of repeated calculations and the variable *x* going from *1* to *M*, the mean can be calculated by:

$$\bar{x} = \frac{1}{M}\sum_{k=1}^{M} X_k \tag{14}$$

And the standard deviation consequently is:

$$\sigma_x = \sqrt{\frac{1}{M-1}\sum_{k=1}^{M}(X_k - \bar{x})^2} \tag{15}$$

And then, the error is:

$$\epsilon_{\bar{x}} = \frac{\sigma_x}{\sqrt{N}} \tag{16}$$

Therefore, the relative error is:

$$RE_{\bar{x}} = \frac{\epsilon_{\bar{x}}}{\bar{x}} \tag{17}$$

For normal Monte Carlo calculations where the problem specifications are fixed, as it is in this work, the statistical uncertainty in the results decreases as $\frac{1}{\sqrt{N}}$, where N is the number of histories run in the problem [56].

To reduce simulation time, the cluster from the DKFZ was used in the simulations. There are 200 CPU cores available to work at the same time per user, therefore the input files were divided by 200 input files with different initial seeds to guarantee a good statistic result. MCNP mactal files were created in every input file ran at the cluster, to combine the files the input code must have two requests, they are: identical geometry, cross-sections, code options, and the number of initial seeds must be also different.

The MCNP merge mactal tool merges the tallies information into one single file. The new information is based on the following calculations [57]:

$$\bar{x}(comb) = \frac{1}{N_1 + N_2}\left[\sum_{k=1}^{N_1} X_{1,k} + \sum_{k=1}^{N_2} X_{2,k}\right] \tag{18}$$

As N_1 and N_2 being the number of particles from the first and the second simulation. The new value will sum the two means acquired in simulations described in equation 18 as well as the new relative error, given by [57]:

$$\sigma_x(comb) = \sqrt{\frac{1}{N_1 + N_2}\left[\frac{1}{N_1 + N_2}\left[\sum_{k=1}^{N_1} X_{1,k} + \sum_{k=1}^{N_2} X_{2,k}\right] - \overline{x^2}(comb)\right]} \tag{19}$$

The relative error will be calculated using Equation 17, with the new values obtained from Equations 18 and 19. These equations demonstrate that the relative error decreases as the number of particles increases, which is why using as many particles as possible is essential to this work.

The detectors are placed 25 cm away from the flask, and the gamma-ray production can be considered isotropic [50], meaning it is distributed uniformly over the surface of a sphere with a radius of 25 cm, as represented in Figure 25. By comparing the total superficial area of the sphere with the sensitive area of the detectors, it is possible to calculate the percentage of photons emitted by $Dotarem^{(R)}$ that will reach the detector. Using basic geometry, the surface area of the sphere is $7.85.10^3\ cm^2$. The scintillator has a cylindrical sensitive area of 1.9 cm radius facing the flask; therefore, the total area is $11.34\ cm^2$.

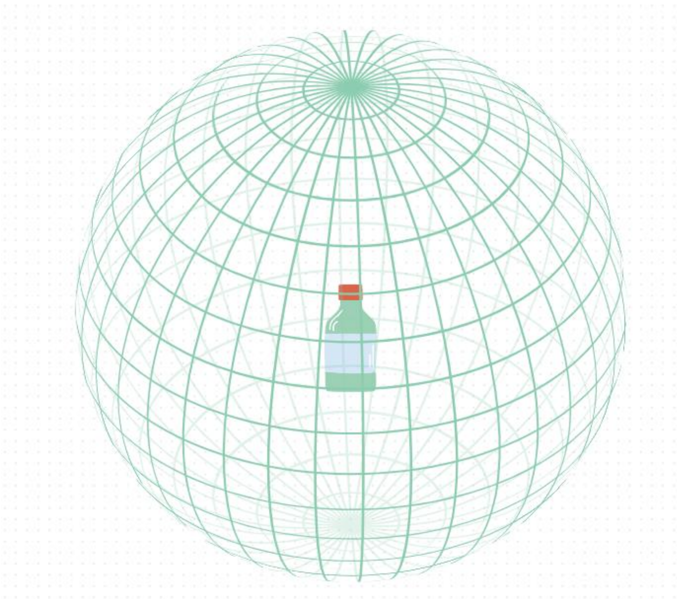

Figure 25 - Isotropic distribution of prompt-gamma and X- ray area around the Dotarem Flask

This indicates that only 0.14% of the photons produced will reach the scintillator. Since the photons in the peak region have a higher flux than those in the background, a large number of particles are necessary to obtain good statistics and reliable information from the background radiation. After several simulations, a satisfactory statistical result was achieved by running 10^{11} particles, which requires a significant amount of simulation time.

3.4.1.6. Single Track card

Particle Induced X-ray Emission (PIXE) is a phenomenon that occurs when an electron transitions from an outer shell to an inner shell following ionization by a high-energy particle. Accurate analysis of these electron interactions is crucial for obtaining reliable PIXE estimations, which is where the Monte Carlo N-Particle Transport Code (MCNP) plays a significant role.

MCNP employs a condensed history algorithm to simulate the transport of charged particles effectively [43]. This algorithm approximates the cumulative effects of numerous small-angle scattering events and energy losses over a short path segment, rather than simulating each individual interaction. By consolidating multiple interactions into larger, more manageable steps, the algorithm significantly reduces computational complexity while still capturing the essential characteristics of particle transport accurately [47]. This approach achieves a balance between accuracy and efficiency, allowing for the simulation of complex physical phenomena within a practical time frame, which is vital for effective analysis in radiation transport studies. The first simulation was done using only with a proton beam to verify the difference between using the condensed history algorithm and the single-track event. By default, the MCNP only takes a single-

event track for electrons under 1 keV, what represents no impact on the 43 keV photons at study [43]. The region of interest is made by photons produced manly from neutron capture or for medium ionization [34]. To investigate the impact of the algorithm, the neutron transport was canceled meaning that the 43 keV peaks will be made only by PIXE photons. The geometry for figure 24 was used to do the simulation with 10^7 protons being irradiated from the source.
Figure 26 shows the results of the simulations using the $CeBr_3$ scintillator as detector. It is important to mention that, because it was only to see the flux of the 43 keV peak, this simulation isn't done with many particles in order to save time, what explains the low statistics in the background. The difference was that the single track increased the flux of 43 keV peak in 7.14%.

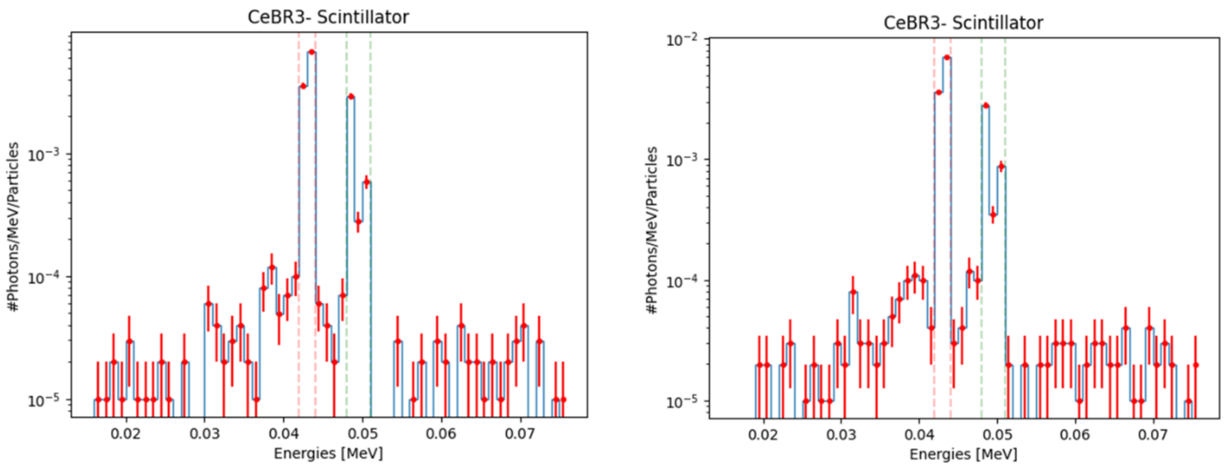

Figure 26 - 2D spectrum from 0.01 MeV to 0.07 MeV. On the left neutron free without single track on the right neutron free with single track for electrons under 70 keV for Proton beam.

This tool can only be used when it is also uploaded the Electron/Photon/Relaxation data library (EPRDATA14) that is based on the EPICS2014 (electron and photon interaction Cross Section) data from the International Atomic Energy Agency (IAEA) [58]. This data table brings many new improvements to the simulations, with the ones more important for this work: New data for electron interactions such as subshell-specific electro ionization, and atomic excitation, a much more detailed representation of atomic relaxation.

3.4.1.7. Coarse Grained Multiscale (CGM)

Another card used in MCNP code is the CGM method to correlate neutron and gamma emission in cascade mode. It is a computational approach that integrates detailed, fine-scale simulations with more approximate, larger-scale models. The effectiveness of this method is because it focuses on critical regions or processes, while using simpler models for less critical areas [43]. Activating this card on the neutron physics area, the tool produces photons by neutron interactions with high accuracy. It also increases the time of simulation.

3.4.2. Equivalent Dose calculation

For the second part of the work, the written code uses many sets discussed in the previous section. Although the contribution for the dose of the secondary particles is less important than the medium ionization, the physics of CEM03.03 and LAQGSM03.03 was kept in the dose calculations, as longitudinal and lateral dose distributions in MCNP6 have been validated for heavy ion therapy by various research groups [22]. The geometry of the experimental setup is as mentioned in figure 24, and the materials and source configuration were kept the same.

The CGM card was also used as the neutron's interactions determine prompt-gammas that have enough energy to ionize the medium and contribute to the dose. The single-track event is not necessary – the Gadolinium PIXE is not the particle that wanted to be detected – so it was not included as it increases the time of simulation by several days and would not show a big difference on the dose deposition.

3.4.2.1. Tally Detector

An *F8 pulse height tally was placed in the $Dotarem^{(R)}$ flask. As previously explained, this tally detects only the particles that interact with the medium. However, energy bins were not set, it represents that the tally will accumulate all energy deposited by any particles energies interacting with the material within the flask. The source particles and the ones created by the nuclear reactions will do an energy deposition in the flask, therefore multiple *F8 tallies were used to separately collect energy from photons (p), electrons (e), neutrons (n), protons (h), deuterons (d), tritons (t), helions (s), and alpha particles (a). As those particles will have different radiation weighting factors.

The output file of the tally *F8 gives 10 statistical checks for the estimated answer of the tally. One of them is the relative error (as mentioned in the 43 keV peak region spectrum) others are the variance, figure of merit (FOM) and pdf Slope [47]. All the results of the tests come in the output file, and a tally is considered to be converged with high confidence only when it passes all ten statistical checks [43]. The results table of this tally gives the mean value of the energy deposited in the surface in MeV/#, as well as the relative error. Add to that there are the variance of the variance value and the FOM.

The variance of the variance (VOV) is a statistical measure used to assess the consistency of the variability within a set of data [43]. Mathematically, it quantifies the extent to which individual sample variances differ from the overall variance of the population or the expected variance. This is crucial in determining whether the observed variability is due to random chance or if there is a systematic difference in the spread of data across different samples. The VOV is particularly important in hypothesis testing because it helps to evaluate the robustness of

assumptions about homogeneity of variance, ensuring that conclusions drawn from the data are reliable.
The figure of merit (FOM) test is a crucial metric used to evaluate the efficiency of a simulation in terms of statistical accuracy and computational performance [43]. Mathematically, the figure of merit is defined as the inverse of the product of the variance (σ) and the computation time (τ). Represented as follows [47]:

$$FOM = \frac{1}{\sigma \times \tau} \quad (20)$$

This measure allows users to compare different simulation setups, where a higher FOM indicates a more efficient simulation, achieving lower statistical uncertainty for a given amount of computation time. In practical terms, the FOM test helps in optimizing simulations by balancing the trade-off between accuracy and computational resources, guiding users to a most effective use of their computational efforts in achieving reliable results.
The dose simulated in MeV/# will be converted to Gray/# in the following steps:

- 1 MeV = 1× 10^6 eV (a) = 1.6022× $10^{-19}\,J\ (b)$, therefore the value in MeV will be multiply by (a) and by (b) for converting value into Joules.
- As the goal is to compare the dose between beams, all of them will be divided by 1 kg to turn the value into Gray.

3.4.2.2. Equivalent Dose Calculations.

Getting the absorbed dose is the first step to calculate the equivalent dose. Is possible to use the concept of equivalent dose defined by the International Commission on Radiological Protection (ICRP) as follows [59]:

$$H_{T,R} = W_R . D_{T,R} \quad (21)$$

Where $D_{T,R}$ is the absorbed dose averaged over a tissue or organ T, due to radiation type R and the W_R is a dimensionless factor used to account for different biological effects of various types and energies of radiation. It is defined by the ICRP to provide a way to compare the potential biological damage caused by different types of radiation when absorbed by the body. A table is published in ICRP Publication 103 with all values related to the radiation incident on the body [60]. An adaptation of this data is shown in table 8 containing all the particles considered in this work.

Radiation Type	Radiation weighting factor W_R
Photons and Electrons	1
Protons	2
Alpha particles, fission fragments, heavy ions	20
Neutrons	$* \, 2{,}5 \, + 18.2 \exp\left[\frac{-(\ln (E_n))^2}{6}\right], E_n < 1 \, MeV$ $* \, 5 \, + 17 \exp\left[\frac{-(\ln (2E_n))^2}{6}\right], 1MeV \, < E_n < \, 50 \, MeV$ $* \, 2{,}5 \, + 3.25 \exp\left[\frac{-(\ln (0{,}04E_n))^2}{6}\right], \, E_n > \, 50 \, MeV$

Table 8 - Weighting Factor for particles used in this work [60].

According to ICRP 103, the neutron function has been derived empirically and has consistency with physical knowledge. It is recommended that the weighting factor for neutrons will be calculated by this function. The neutron exposure on this work involves a range of energies and the low energy range takes a large contribution of secondary photons to the absorbed dose in the human body so the radiation weighting factor will be used to calculate an equivalent dose for the radiation biological effects, meaning that no equivalent dose will be calculated, once the organs will not be considered [60].

3.5. Spectrum Analysis

The F8 output mctal file can be utilized to determine the flux, provided that the bin intervals specified in the simulation input file are included [57]. The resulting file is a three-column text document, where the first column lists the bin intervals, the second column indicates the number of particles that interacted with the detector material and released energy corresponding to the specified bin interval. This value is expressed as the ratio of the number of particles that crossed the surface to the total number of source particles simulated. The third column presents the relative error of this measurement, which is contingent upon the number of particles that traversed the surface area. The data generated from the mctal file are initially unnormalized; thus, a normalization process is necessary prior to plotting the spectrum. To ensure data integrity, 1 keV bin was employed throughout all simulations. However, it is important to note that the detectors exhibit poorer resolution than this bin size. Consequently, a convolution process is required to facilitate the comparison between experimental data and simulation results.

3.5.1. Normalization of the Spectrum

Normalizing the spectrum obtained from MCNP simulations is essential for facilitating comparison with experimental data, as it ensures that the results are presented on a consistent and comparable scale. Without normalization, variations in bin widths and total counts can result in erroneous interpretations of the data. The experimental spectra referenced in the report further underscore the importance of this normalization process, as it allows for a more accurate evaluation of the simulation outcomes in relation to observed experimental results [50].

A Python script was developed to normalize the spectral data. Initially, bin width normalization was performed using the results obtained from the MCNP6, which are presented in histograms with counts distributed across bins of varying widths. Each bin in the spectrum possesses a defined width ΔE. The raw tally, T, for each bin is divided by the corresponding bin width, resulting in a density that can be interpreted as counts per unit energy. This process is mathematically represented by the following equation:

$$T_{(normalized)} = \frac{T}{\Delta E} \tag{22}$$

The spectrum is also normalized by the total number of simulated source particles, enabling the representation of the spectra shown in Figure 26. The y-axis corresponds to the total number of photons per MeV per total source particles. Let N_s denote the number of simulated source particles; thus, the normalization is defined as follows:

$$T_{(normalized2)} = \frac{T_{(normalized)}}{Ns} = \frac{T}{\Delta E . N_s} \tag{23}$$

3.5.2. Signal Convolution

The detector resolutions, defined as the ability of a detector to distinguish between two closely spaced energy or wavelength values within a spectrum [49]—a measure that reflects the detector's precision and accuracy in identifying and measuring distinct signals. Higher resolution enables the detector to more effectively separate and identify closely spaced spectral lines, resulting in more detailed and accurate spectral data. Detector resolution is commonly quantified by the full width at half maximum (FWHM) of its response to a monochromatic source; a lower FWHM value corresponds to higher resolution. In particular, the resolution of a scintillator detector is characterized as a function of the photon energy, indicating how resolution changes with photon energy levels [49].

$$R(\%) = 108.E^{-0.498} \quad (24)$$

The R(%) is the percentage resolution of the photon and E is the energy in keV. Therefore, as the 43 keV peak region is the photon of interest, the percentage will be R(%) = 16.59% meaning that the resolution for the scintillator for that energy photon is approximately 7.13 keV.
In simulations, spectra are frequently generated under idealized conditions with theoretically infinite resolution, which fail to capture the practical limitations of real-world instrumentation. Experimental spectra, in contrast, are affected by instrumental broadening, noise, and other factors that can alter or distort the signal. Convolution, a mathematical operation, is used to combine two functions, producing a third function that characterizes how the shape of one function is modified by the other [61]. This process improves the accuracy of simulated spectra in representing experimental data by incorporating instrumental effects. Let $f(t)$ denote the spectrum function with a resolution of 1 keV, and $g(t)$, a Gaussian-distributed function with a resolution of 7.13 keV. Mathematically, the convolution of these two functions is expressed as [61]:

$$(f * g)(t) = \int_{-\infty}^{\infty} f(t).g(t-\tau).d\tau \quad (25)$$

The result of this operation is a new function $(f * g)(t)$ which describes the combined effect of $f(t)$ and $g(t)$. An example of convolution operation can be seen in figure 27. The original data with a 1 keV resolution created in the bins of the simulation and the convolve curve created turning the resolution 7.13 keV. Error bars in the convolve curve are also shown.

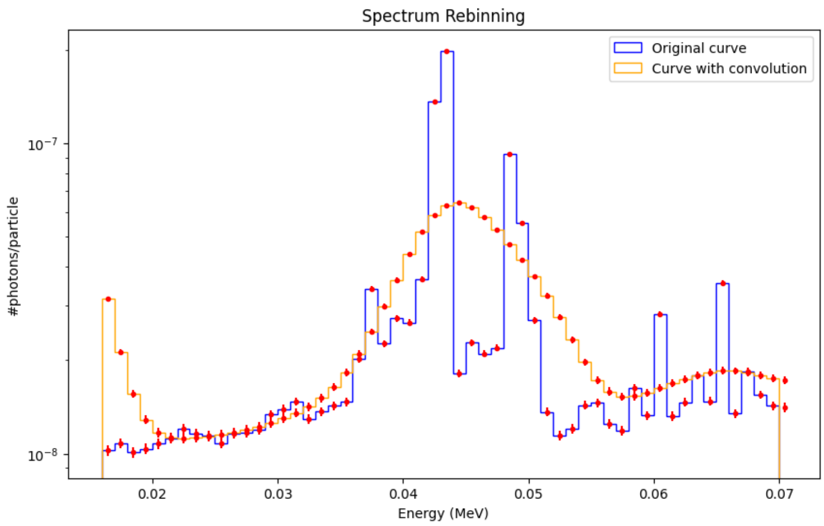

Figure 27 - 2D spectrum of a proton irradiation into da Gadolinium Flask.

To calculate it from the new spectrum, an error propagation method was applied in the python code. Mathematically the uncertainty of the convolve spectrum will be calculated as follows [61]:

$$\sigma_{f*g}(t) = \sqrt{\left(\frac{\partial(f*g)(t)}{\partial f}\sigma_f\right)^2 + \left(\frac{\partial(f*g)(t)}{\partial g}\sigma_g\right)^2} \tag{26}$$

3.5.3. 43 keV Peak Area calculation

To validate the MCNP code, an area calculation was performed in the convolve spectrum using a sum method, described mathematically as:

$$Peak\ Area = \sum_{i=A}^{B} C_i - (B-A).\frac{C_A + C_B}{2} \tag{27}$$

The equation represents the sum of the y-axis values from limit A to B, subtracting the background radiation represented by the trapeze $(B-A).\frac{C_A+C_B}{2}$. An example is shown in figure 28, where it is possible to see the point (A,C_A) and (B,C_B) choosing by the user and represented in the graph as the red vertical lines.

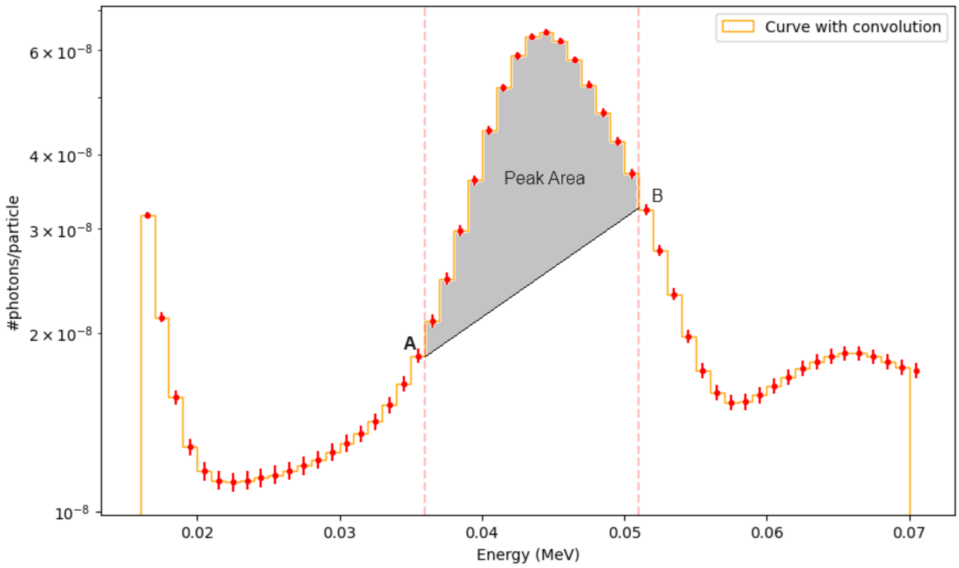

Figure 28 - 2D spectrum of a convolve curve representing the Peak area sum.

The limits A and B are decided by user, in order to compare the experimental data to the simulation in the same range of energy as the experimental analysis was chosen. It is possible to see in figure 20.a that the peak region ranges from 30 keV to 60 keV.

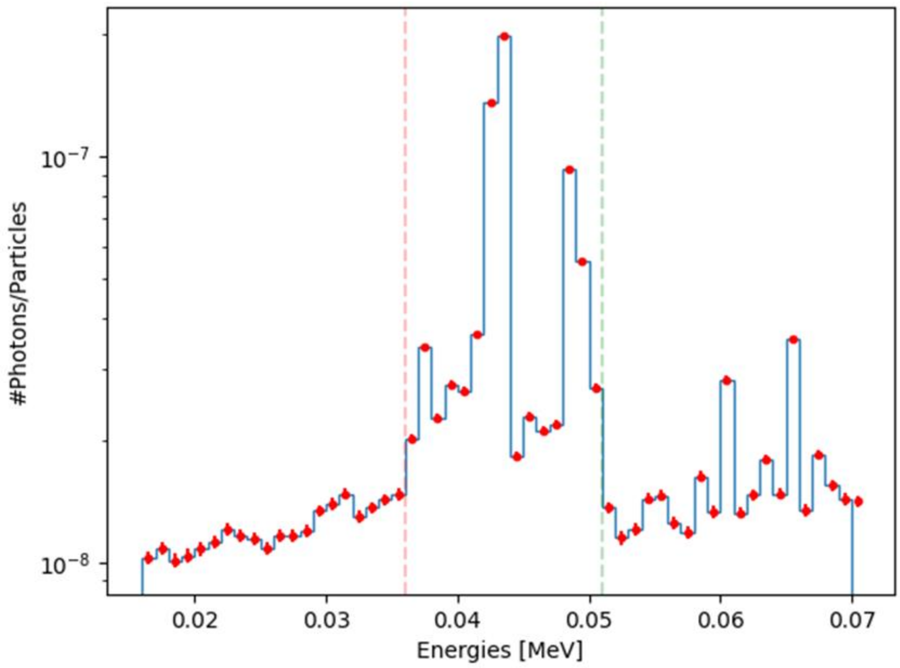

Figure 29 - 2D spectrum of a proton irradiation on a Gadolinium flask with 1 keV bin.

Comparing figures 28 and 29 is possible to see that the peak with a better resolution has a clear beginning and ending. After convolution, it mixes with background radiation. The background has an influence on the peak region, it´s possible to see that the convolved curve has a larger beginning and finishing as it does in the experimental results.

3.6. Equivalent Dose Analysis

The pulse-heigh tally F8* gives an output file with the total Dose generated in the volume along with the statistical error associated with the measurement. As mentioned above, will be converted to Gray and then represented in Sievert when multiplied by the weighting radiation factor. 9 different *F8 tallies were simulated in order to collect the dose from the different particles, necessary because the weighting factor from those fragments is different and therefore, the equivalent dose will be also related to that (table 8). One tally refers to all particles together in order to check if 100% of the dose in the material is equal to the sum of individual tallies. After that, the percentage of each contribution will be multiplied by table 8 factor and then summed to find the total equivalent dose.
The tissue weighting factor will not be considered. The goal is to compare the RBE of the absorbed dose with experimental data of the radiation flux to realize which different beam species could work in vivo dosimetry, so there is no reason to investigate the tissue contribution to the dose.
Table 8 shows that ICRP 103 calculates the neutron weighting factor based on its energy, therefore it will be placed a flux tally, on the $Dotarem^{(R)}$ flask during the dose simulation. This tally will reflect the flux of all neutrons inside the recipient from 0.01 keV to 10 MeV energy range. The bins will be interpolated

and the flux for each energy will be detected and saved. It is important to mention that the flux tally F4 does not need the particle to interact with the medium, it means that some neutrons will be created but will not contribute with dose. The aim of this tally is to detect the percentage of neutrons created in the flask, to distribute this value through the different equations shown in table 8 and then give the approximate contribution of the different energy neutrons to the total equivalent dose. F4 tally is perfect for this simulation because it collects the flux or particles per area of the surface. As the low energy neutrons would interact very shortly close to the place where it was created, a pure flux tally, such as F4, wouldn't be able to record them, because they won't cross the surface area.

4. Simulation Results

Simulation results are presented in this chapter beginning with proton, followed by Helium and Carbon ion spectrum and equivalent dose simulation outputs. All the materials and geometry described in the previous chapter were applied to every beam. The only difference between the simulations was the source particle and its energy, as it was in the experiment. The simulations were done with 10^{11} particles from the source in the 43 keV peak region spectrums, in order to guarantee good statistical results. In the equivalent dose analysis, a total of 10^{8} particles were simulated, as this quantity is sufficient to yield statistically reliable results.

4.1. 43 keV peak simulations

To check the capacity of the MCNP6 to simulate the gamma and x-rays for the Gadolinium, a comparison using data from the experiment was performed, (figure 21). The area is calculated as described in the methodology chapter.

4.1.1. Proton Beam

Figure 30 is a plot of energy going from 10 keV to 7 MeV. It is crucial to determine whether the lines corresponding to the prompt gamma and the expected X-ray were successfully detected.

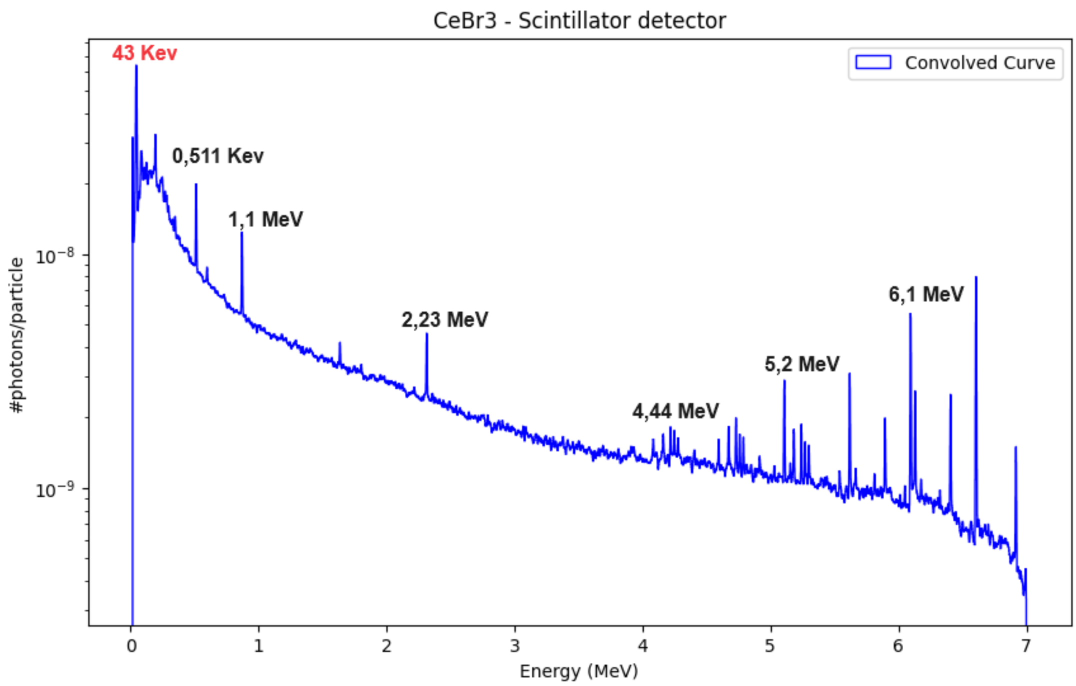

Figure 30 - 2D Convoluted Spectrum for a proton beam irradiation on DOTAREM from the MCNP6 Simulation.

Figure 12 shows the experimental deexcitation data from a proton beam that can be compared with the simulated results from figure 30. MCNP6 is simulating the deexcitation process of the atoms successfully. The single-track event was only activated for electrons under 75 keV, as the goal is the 43 keV peak region, to reduce simulation time, that can lead to less accuracy for the high energy prompt gamma rays or characteristic x-ray. The flux of the 43 keV peak photons is the highest in the spectrum due to the elevated thermal neutron cross section from the Gadolinium, making the neutron capture process more likely to happen plus the PIXE process from the beam itself.

Error bars were calculated after the curve convolution (figure 31). The relative error (denoted as $RE_{\bar{x}}$)), represented by the red dots and also provided in table 9, remains below 0.1 (10%) within the region of interest, which aligns with reliable findings reported in the literature [52]. The higher the number of particles interacting in the detector by each bin, less relative error and on the 43 keV peak, is possible to see that the uncertainty is 0.9%, it is therefore considered a reliable data. It is also important to collect information from the background and the background photons relative error goes around 3.2%, what is also considered a reliable data.

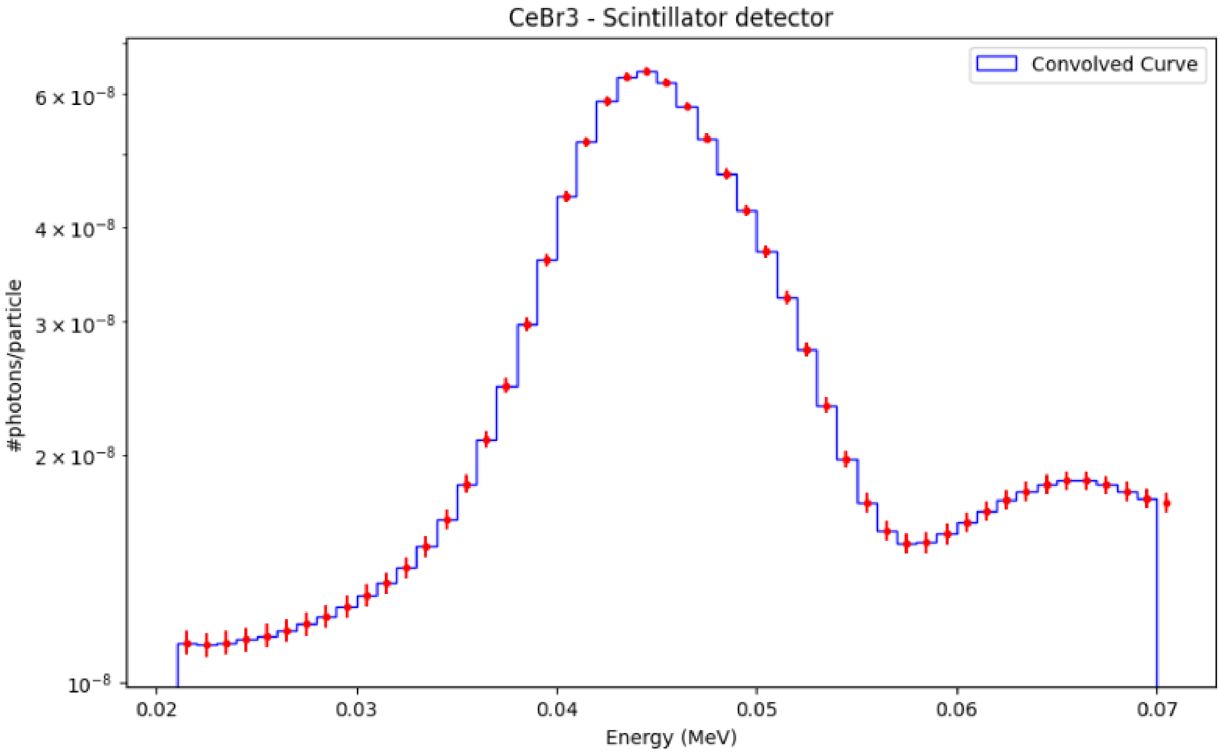

Figure 31 - 2D convoluted Spectrum with error bars from the MCNP6 simulation for a proton beam of the interested zone.

To calculate the area, we used the range of energy from the experimental data analysis. The peak region was defined by the interval from 30 to 60 keV, as shown in Figure 32. We can then calculate the area according to Equation 27.
The calculated area is $9.52.10^{-7}$ #photons/ion.

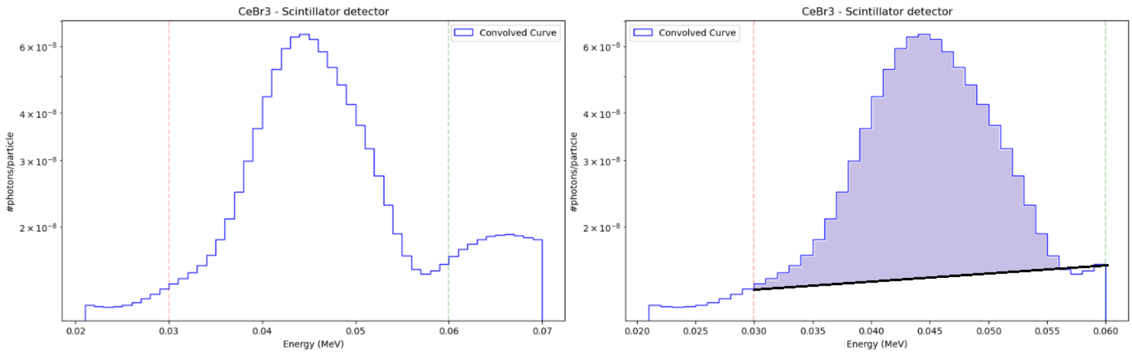

Figure 32 – Left: The spectrum selection from 0.03 to 0.06 MeV marked in the red and green lines respectively. Right: the calculated area delimited over the baseline.

Photon Energy [keV]	Relative Error ($RE_{\bar{x}}$)	Percentage
10	0.0026	0.2%
15	0.0348	3.5%
20	0.0376	3.7%
30	0.0337	3.3%
35	0.0326	3.2%
40	0.0237	2.3%
43	0.0096	0.9%
45	0.0287	2.9%
50	0.0161	1.6%
55	0.0323	3.2%
60	0.0234	2.3%
65	0.0208	2.1%

Table 9 – Zone of interest bins relative errors for the Proton beam simulation

4.1.2. Helium Beam

Same procedure was done for the Helium Beam, first checking the whole spectrum (Figure 33):

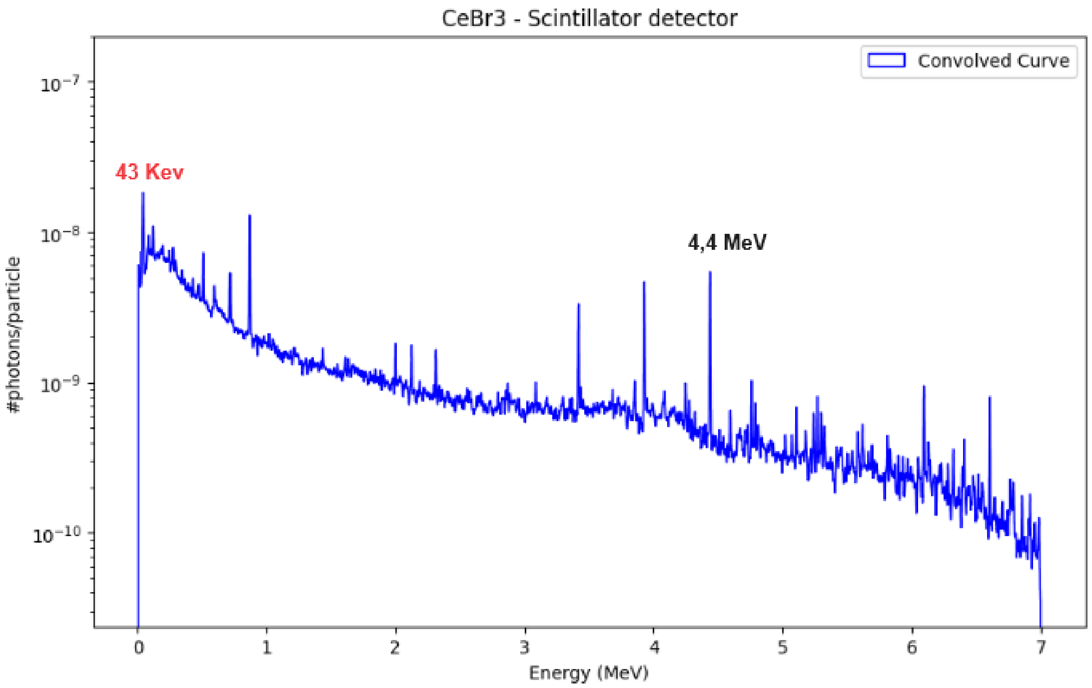

Figure 33 - 2D Helium beam spectrum.

Comparing the lines with those from in Figure 12, it can be seen that the de-excitation is also well simulated in the helium beam. Analyzing the errors in Table 10 and Figure 34 reveals that, for the same reasons as with the proton beam, the data is reliable

Photon Energy [keV]	Relative Error ($RE_{\bar{x}}$)	Percentage
10	0.0033	0.3%
15	0.0848	8.5%
20	0.0913	9.1%
30	0.0828	8.3%
35	0.0846	8.5%
40	0.0647	6.5%
43	0.0258	2.6%
45	0.0755	7.6%
50	0.0596	6.0%
55	0.0729	7.3%
60	0.0726	7.3%
65	0.0822	8.2%

Table 10 – Zone of interest bins relative errors for the helium beam simulation.

The relative errors increased in the helium simulation, indicating that the flux of photons was lower than in the proton irradiation. However, the errors remain below 10%, which suggests that the results are reliable. This can also be observed in Figure 34, where the red dots are thicker than those for proton irradiation

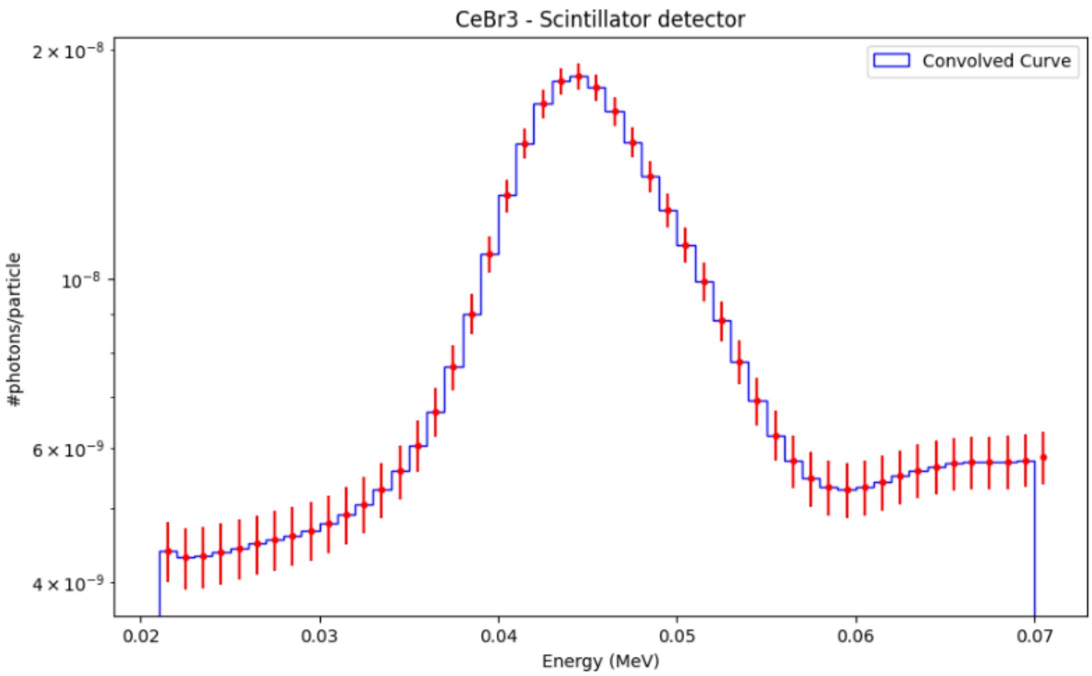

Figure 34 - 2D convoluted spectrum with error bars from MCNP6 simulation of helium beam of the interested zone.

Area calculation was done in the same range as protons and experiments results (figure 35). The calculated area is $2.99.10^{-7}$ #photons/ions.

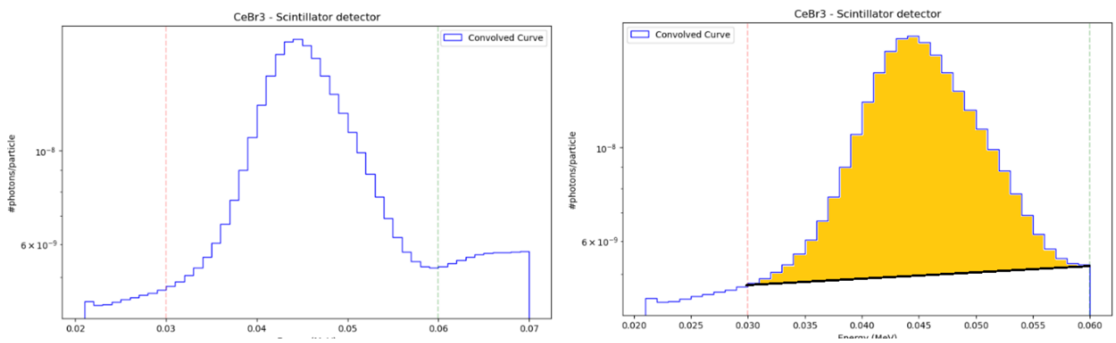

Figure 35 - Left: The spectrum selection from 0.03 to 0.06 MeV marked in the red and green lines respectively. Right: The calculated area delimited over the baseline.

4.1.3. Carbon Beam

Figure 36 shows the total spectrum of the carbon beam simulation.

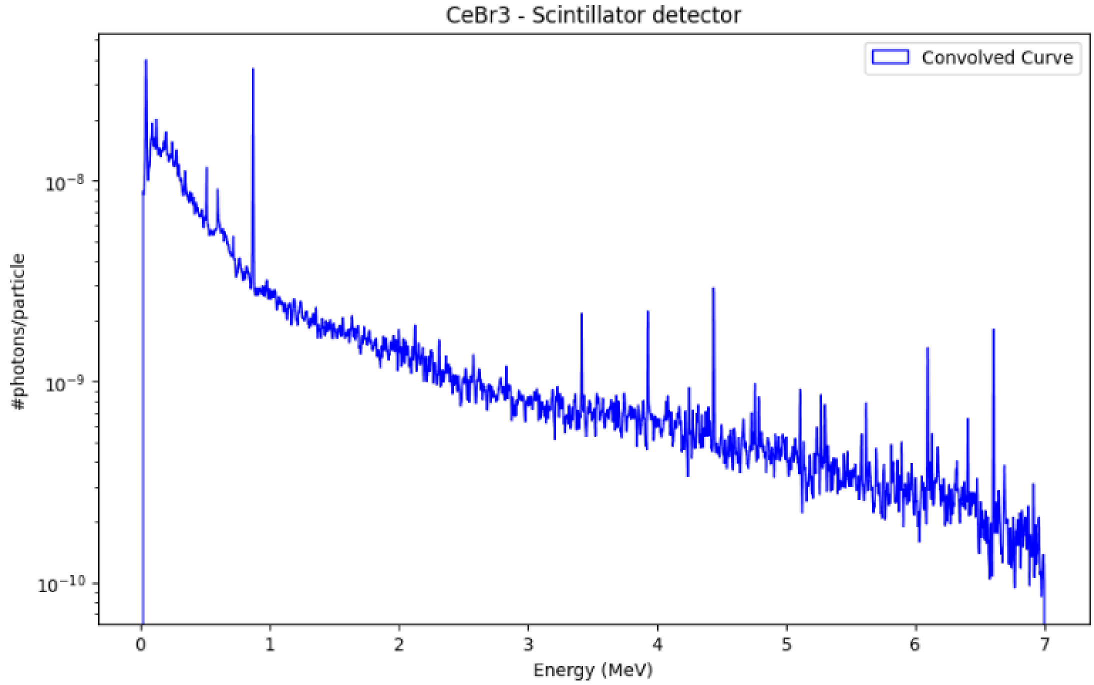

Figure 36 - 2D convoluted spectrum for a carbon beam irradiation on DOTAREM from the MCNP6 simulation.

By examining the relative errors for the carbon beam in Table 11, we can see that the values are still below 10%. Similar to the helium beam simulation, the errors are slightly higher than those for the proton beam, indicating that fewer particles were detected. This is also reflected in Figure 37, where the error bars for the carbon beam are longer than those for the proton beams.

Photon Energy [keV]	Relative Error ($RE_{\bar{x}}$)	Percentage
10	0.0032	0.3%
15	0.0884	8.8%
20	0.0933	9.3%
30	0.0942	9.4%
35	0.0864	8.6%
40	0.0616	6.2%
43	0.0318	3.2%
45	0.0840	8.4%
50	0.0627	6.3%
55	0.0776	7.8%
60	0.0924	9.2%
65	0.0783	7.8%

Table 11 - Some bins relative errors for the carbon beam simulation

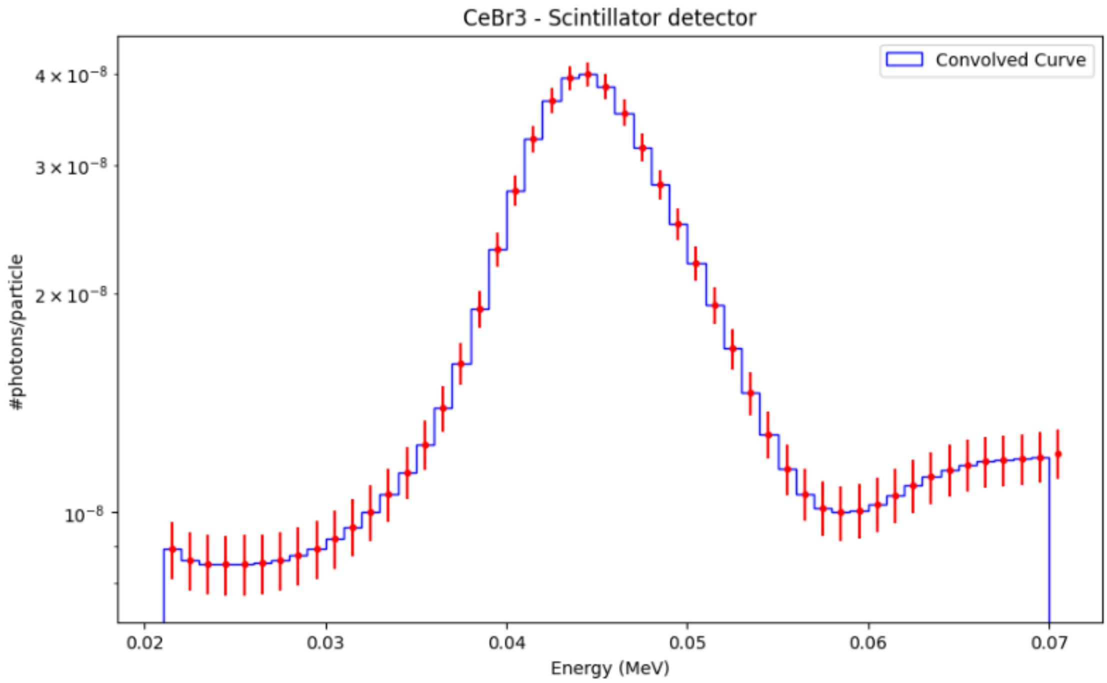

Figure 37 - 2D convolved spectrum with error bars from the MCNP6 simulation.

The same range of energy was used in order to keep the experimental comparation right. It is shown in figure 38. The calculated area is $5.99.10^{-7}$ #photons/ions.

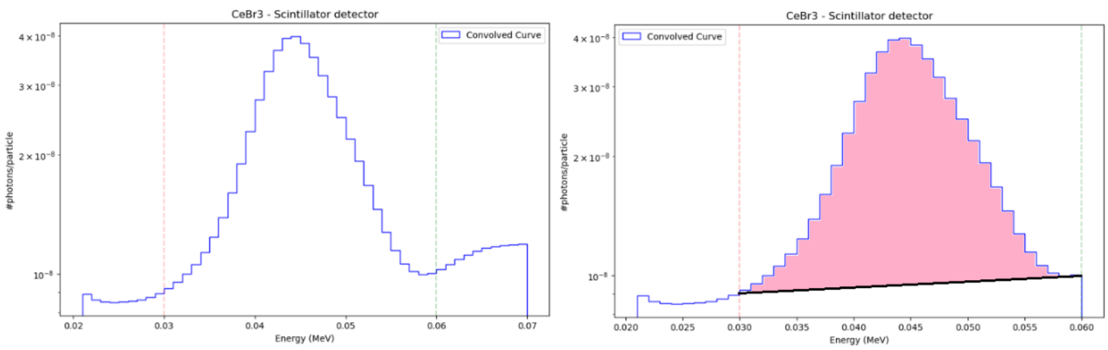

Figure 38 - Left: The spectrum selection from 0.03 to 0.06 MeV marked in the red and green lines respectively. Right: The calculated area delimited over the baseline.

4.2. Equivalent Dose

In this section all the simulation results are presented followed by the value transformed in Gray and then Sieverts after applying the data in table 8. In the neutron calculations it was necessary to use an F1 tally on the simulation. F1 tally is a flux tally and gives the amount of particles that cross the surface [47]. It was used for collecting the neutron spectra and then, using a python code was possible to divide the percentage of neutrons in the 3 different range of energy and it contributions to the total neutron dose.

4.2.1. Neutrons Calculations:

Table 12 shows the calculations of the creation of different energy neutrons during the irradiation. The absolute value of neutrons created is not an important factor in this analysis, therefore the results are shown in percentages.

Energy	10^{-8} to 1 MeV	1 to 50 MeV	< 50 MeV
Proton	60.76%	39.24%	0%
Helium	5.36%	85.13%	9.51%
Carbon	5.52%	63.27%	31.22%

Table 12 - Results of the Neutron Spectra analysis of its energy on different ion species.

As neutron energy is described as an interval of energy, the value used in the equations will be the higher value in the interval, in order to minimize calculation complexity. This decision will create a systematic error in the absolute values of simulated absorbed dose; however, the goal of the present work is comparing the different ion species equivalent dose, therefore, it will not have a significant effect on the conclusions of this study.
For protons the value $E_n = 0.99\ MeV$; Helium, $E_n = 25\ MeV$ and Carbon, $E_n = 100\ MeV$.
Using the percentages described in table 12 and the equations in table 8, the radiation weighting factor for the neutrons will be:

- Protons: $20.69 \times 0.6076 + 6.3265 \times 0.3924 + 0 = 15.05$
- Helium: $20.69 \times 0.0536 + 6.3265 \times 0.8513 + 2.725 \times 0.0951 = 6.75$
- Carbon: $20.69 \times 0.0552 + 6.3265 \times 0.6327 + 2.725 \times 0.3122 = 6.0$

4.2.2. Energy deposition and Measured Dose

The following tables (13, 14 and 15) summarize all the results from protons, Helium and Carbon. The first column shows the tally measured of energy deposition in MeV/source ion of all the different contributions from the different particles in the same surface, it was collected directly from the output file of the *F8 tally. Second, is the conversion of the energy deposited per source ion into Gray. Third, the radiation weighting factor described in table 8 that will be used to determine the last column the equivalent dose of all different ion species. Additionally, a *F8 tally was placed to collect all the dose from the particles together in order to compare the total summed from the initial tallies and the total acquired from a single one.

PROTON BEAM	Absorbed Energy [MeV]/#	Absorbed Dose [Gray]/#	Radiation weighting factor.	Equivalent Dose [milli-Sieverts]/#
Photons (p)	6.08×10^{-2}	9.73×10^{-15}	1	9.73×10^{-12}
Electrons (e)	6.11×10^{-2}	9.77×10^{-15}	1	9.77×10^{-12}
Neutrons(n)	2.54×10^{-2}	4.06×10^{-15}	15.05	6.12×10^{-11}
Protons (h)	5.01×10^{1}	8.02×10^{-12}	2	1.60×10^{-8}
Deuteron (d)	5.27×10^{-5}	8.44×10^{-18}	20	1.69×10^{-13}
Triton(t)	2.01×10^{-6}	3.21×10^{-19}	20	6.42×10^{-15}
Helion (s)	1.63×10^{-5}	2.60×10^{-18}	20	5.21×10^{-14}
Alpha Particle(a)	5.40×10^{-5}	8.64×10^{-18}	20	1.73×10^{-13}
Heavier ions (#)	1.03×10^{-5}	1.66×10^{-18}	20	3.31×10^{-14}
Total summed	5.03×10^{1}	8.04×10^{-12}	-	1.61×10^{-8}
Total from Tally *F8	5.01×10^{1}	8.01×10^{-12}	-	-

Table 13 - Proton Beam simulated energy deposition at the flask.

Helium Beam	Absorbed Energy [MeV]/#	Absorbed Dose [Gray]/#	Radiation weighting factor.	Equivalent Dose [milli-Sieverts]/#
Photons (p)	9.66×10^{-3}	1.55×10^{-15}	1	1.55×10^{-12}
Electrons (e)	9.66×10^{-3}	1.55×10^{-13}	1	1.55×10^{-12}
Neutrons(n)	1.13	1.80×10^{-13}	6.75	1.22×10^{-9}
Protons (h)	4.76×10^{-2}	7.62×10^{-15}	2	1.5210^{-11}
Deuteron (d)	2.21×10^{-3}	3.54×10^{-16}	20	7.07×10^{-12}
Triton(t)	1.55×10^{-5}	2.48×10^{-18}	20	4.97×10^{-14}
Helion (s)	1.49×10^{2}	2.38×10^{-11}	20	4.77×10^{-7}
Alpha Particle(a)	1.79×10^{-3}	2.86×10^{-16}	20	5.71×10^{-12}
Heavier ions (#)	2.61×10^{-5}	4.18×10^{-18}	20	8.35×10^{-14}
Total summed	1.50×10^{2}	2.40×10^{-11}	-	4.8×10^{-7}
Total from Tally *F8	1.49×10^{2}	2.38×10^{-11}	-	-

Table 14 - Helium beam simulated energy deposition at the flask.

Carbon beam	Absorbed Energy [MeV]/#	Absorbed Dose [Gray]/#	Radiation weighting factor.	Equivalent Dose [milli-Sieverts]/#
Photons (p)	2.82×10^{-2}	4.52×10^{-15}	1	4.52×10^{-12}
Electrons (e)	2.82×10^{-2}	4.52×10^{-15}	1	4.52×10^{-12}
Neutrons(n)	6.58	1.05×10^{-12}	6	6.31×10^{-9}
Protons (h)	2.43	3.89×10^{-13}	2	7.78×10^{-10}
Deuteron (d)	2.05	3.28×10^{-13}	20	6.57×10^{-9}
Triton(t)	1.14	1.82×10^{-13}	20	3.64×10^{-9}
Helion (s)	2.11×10^{-1}	3.36×10^{-14}	20	6.76×10^{-10}
Alpha Particle(a)	2.85	4.56×10^{-13}	20	9.12×10^{-9}
Heavier ions (#)	1110	1.72×10^{-10}	20	3.56×10^{-6}
Total summed	1130	1.81×10^{-10}	-	3.60×10^{-6}
Total from Tally *F8	1120	1.79×10^{-10}	-	-

Table 15 - Carbon Beam simulated energy deposition at the flask.

5. Discussion

In this chapter will be presented the discussion of the simulation results and analysis with the experimental data.

5.1. 43 keV peak region

Figure 39 combines the MCNP6 simulated areas in plot bars as figure 21 does for the experiment areas.

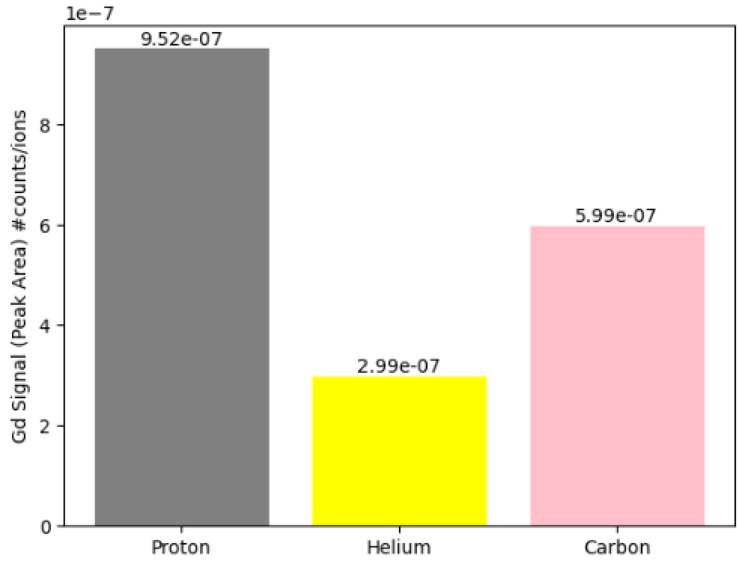

Figure 39 - GD signal as function of ion for irradiation of a vial filled with GD simulated in MCNP6.

In Figure 39, it is evident that the MCNP6 simulation exhibits significantly different behavior compared to the experimental data. The experiment demonstrated that the interaction regions for the Helium and Carbon beams were significantly larger than those for protons, with areas approximately 5 and 100 times greater, respectively. In contrast, the simulation results indicated that the Helium beam had an area 3.2 times smaller, and the Carbon beam had an area 1.6 times smaller than that of the proton beam. Additionally, the relationship between helium and carbon was also different; the experimental data showed the carbon beam area to be 17.8 times larger than that of helium, while the simulation suggested this difference was only 2 times.
Before making comparisons, it is important to note that the glass of the flask was not included in the simulation. Therefore, the area values should be corrected according to the attenuation calculation dose in the methodology. It is worth mentioning that these calculations provide a good approximation of the attenuation, although the actual density and composition of the flask are unknown. The corrected areas are presented in Figure 40, alongside the experimental areas. The relative error was calculated in:

$$Relative\ error\ (RE) = \left|\frac{Simulated\ Area - Experimental\ Area}{Simulated\ Area}\right| \tag{28}$$

The error is normalized for the experimental value because it is the considered the right value, therefore it is used as the base for the comparation.

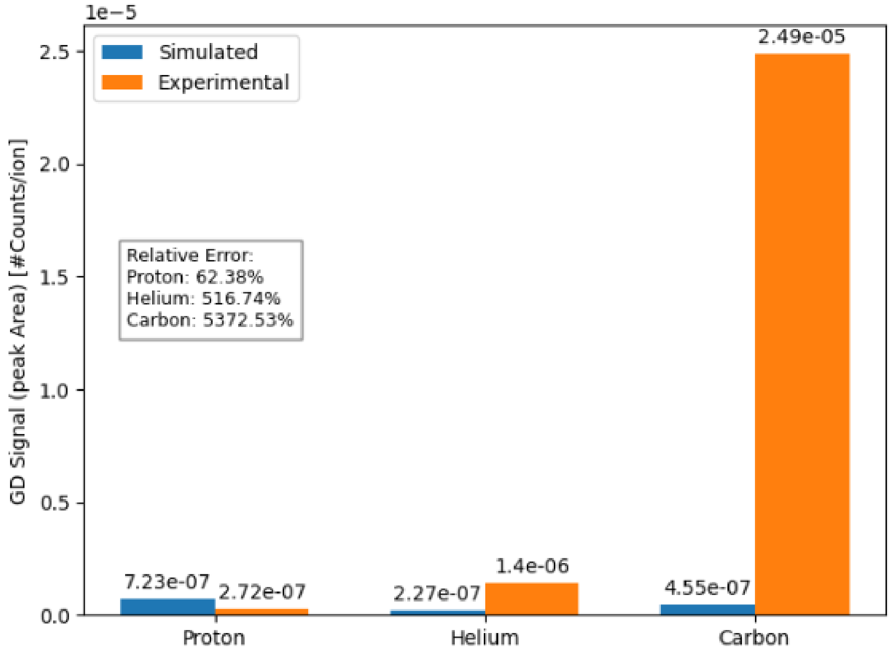

Figure 40 - Comparison areas of the simulation and the experimental data.

After correcting for attenuation, the relative error for Helium and Carbon indicates that there may be an issue with the simulation. The relationship now shows that for the proton beam, MCNP6 predicts an area approximately 2.7 times larger than the experimental results. This value is considered acceptable, as the quantum efficiency of the detector is not incorporated into the software, and the experimental conditions introduce uncertainties that are not accounted for in the simulation. However, for the helium and carbon beams, the areas are approximately 6.2 and 54.7 times smaller, respectively, than those observed experimentally. These discrepancies suggest that the MCNP6 simulation significantly underestimates the flux. Further investigation will be conducted in the next section to understand the source of these discrepancies.

5.1.1. Spectrums analysis

Plotting the experimental and simulated spectra on the same graph allows us to assess whether the analysis of the simulated data matches the behavior of the experimental spectrum. Figure 41 summarizes the spectra of all three ion species along with the experimental data. All spectra were normalized to their respective areas, ensuring that the total integral of each spectrum equals one. This was achieved by calculating the areas under the curves for both the experimental and simulated spectra. Subsequently, each flux value was divided by the corresponding total area. As a result, the normalized spectra represent the probability density, expressed in units of 1/MeV.

The proton simulation yields better results, indicating that MCNP6 effectively simulates neutron capture and Particle-Induced X-ray Emission (PIXE) for protons. The cascade mode also accurately represents the de-excitation of the atoms, as evidenced by the representation of all peaks in the simulation. However, one notable difference is the amount of background radiation; the simulation lacks the same background observed in the experiment. This discrepancy can be attributed to the experimental setup, including the materials supporting the detector, as well as the walls and tables in the laboratory, which likely increased backscattering radiation detected. Consequently, the baseline drawn to account for background radiation in area calculations is elevated, resulting in smaller peak areas. This helps to explain why the simulation predicts an area approximately 2.7 times larger than the experimental data.

The thickness of the 43 peak also aligns well with the experimental data, indicating that the convolution process is functioning effectively for this energy range. However, the flux of the 43 peak is significantly higher in the simulation. This discrepancy arises because the glass flask attenuates the photons, which were not simulated, along with the filter used in the experiment that reduces the peak's flux for better resolution.

For the helium and carbon beams, Figure 41 shows that while the peaks are simulated, the flux differs substantially from the experimental results. This suggests that while MCNP6 can simulate the physics of de-excitation from nuclear interactions and PIXE, further investigation is necessary to determine whether both phenomena are accurately represented. The large difference in flux indicates that either MCNP6 is not simulating one of the phenomena or is not doing so at the correct frequency. The reasons for these discrepancies will be discussed in the next section, which includes a comprehensive investigation.

The larger discrepancy in background radiation is understandable, as the helium and carbon beams possess higher beam energies than protons. This means that the materials surrounding the detector in the experimental room experience significantly more irradiation from higher-energy secondary particles. This is evident in the blue curve of the plots, where the flux difference from the background is notably large.

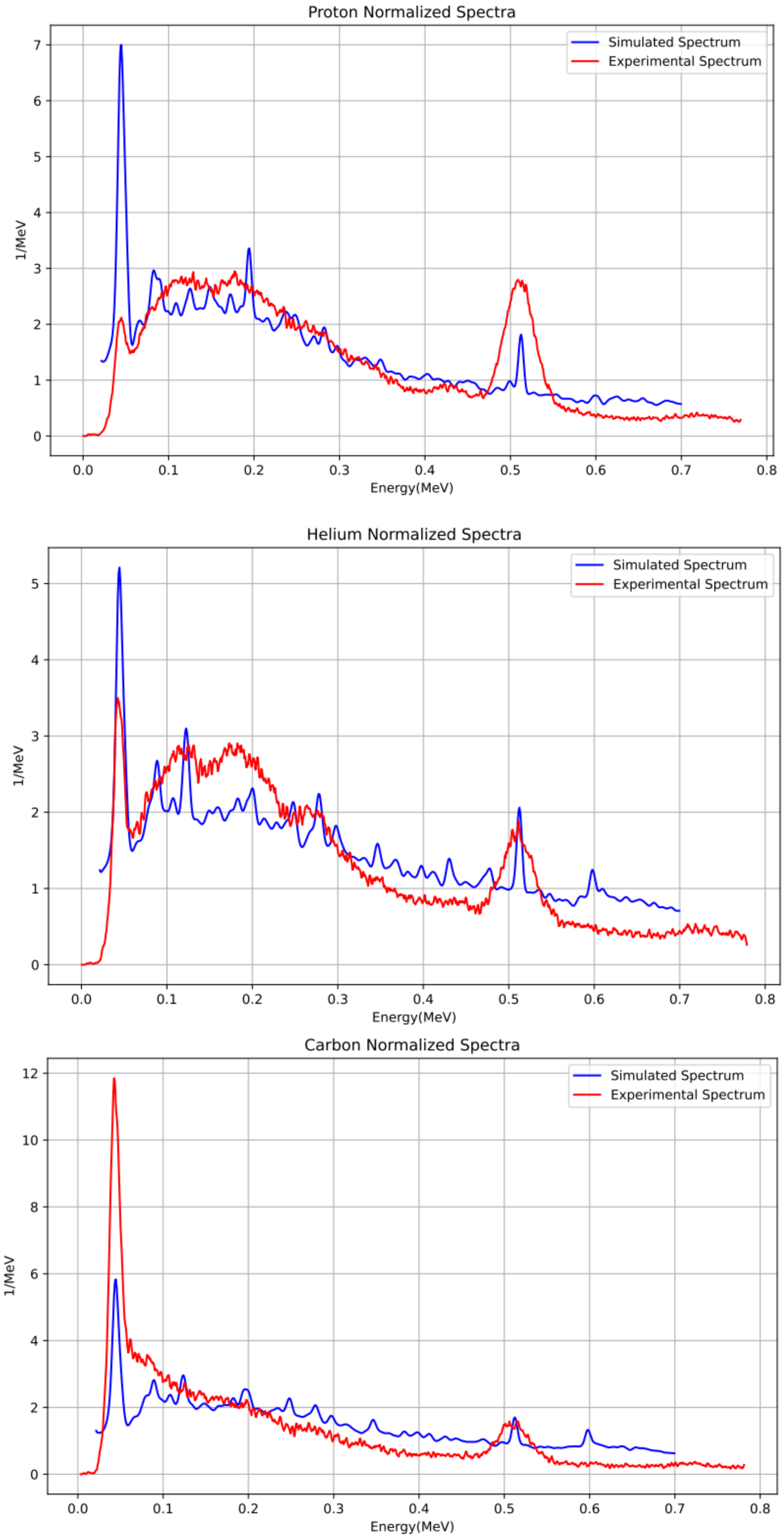

Figure 41 - Plot Crossing the simulated data from MCNP6 and the experimental data for Proton (top), Helium (medium) and Carbon (bottom).

5.1.2. Neutron Production vs Peak signal

The physics models chosen for this work have been tested and validated many times in neutron production and for different geometries. To certify that the neutrons are being well produced from the different ion species, some calculations are performed in this section.
Carbon beams having a bigger area than Helium's is an important factor to consider for trying to understand the MCNP6 discrepant simulation values.
At the output file of the MCNP6 simulation there are information about the different particles' creation, that can be used to investigate the physics phenomenon. Using the neutron creation section on the output file, is possible to see that the simulations for the carbon beam had approximately 19 times more neutrons created than the proton's, and the helium beam had 6 times more. This was expected because Carbon and Helium are bigger atoms than protons, what makes them produce more nuclear reactions and therefore more neutrons. As mentioned in section 2.4 the two main processes responsible for the 43 keV peaks are the PIXE and neutron capture, mostly from the **^{157}Gd** and **^{155}Gd**, owing to its high thermal neutrons capture cross section. But those are not the only kind of neutrons that interact with gadolinium atoms. As shown in figure 42, the neutron capture cross sections depends on its energy, and the highest cross sections goes to neutron from 10^{-5} eV to 0,1 eV, once gadolinium absorbs well thermal neutrons that have a cross section over 10^{4} barns [30].
Considering that, a deeper investigation is necessary to see if those neutrons are produced for each ion species. With that goal in mind, a tally F4 was placed in the flask to collect neutrons from 10^{-12} eV to 1 eV, and then a python code was written to analyze the spectrum and make the calculations of the percentage of neutrons produced from 10^{-5} eV to 0,1 eV to understand if the MCNP6 simulates well the most important kind of neutron for the 43 keV peak region. The total neutron production values demonstrate consistency and have been previously reported in several published studies [30]. However, the analysis of thermal neutrons may provide a novel perspective on the MCNP6 code when utilizing these specific physics setups.

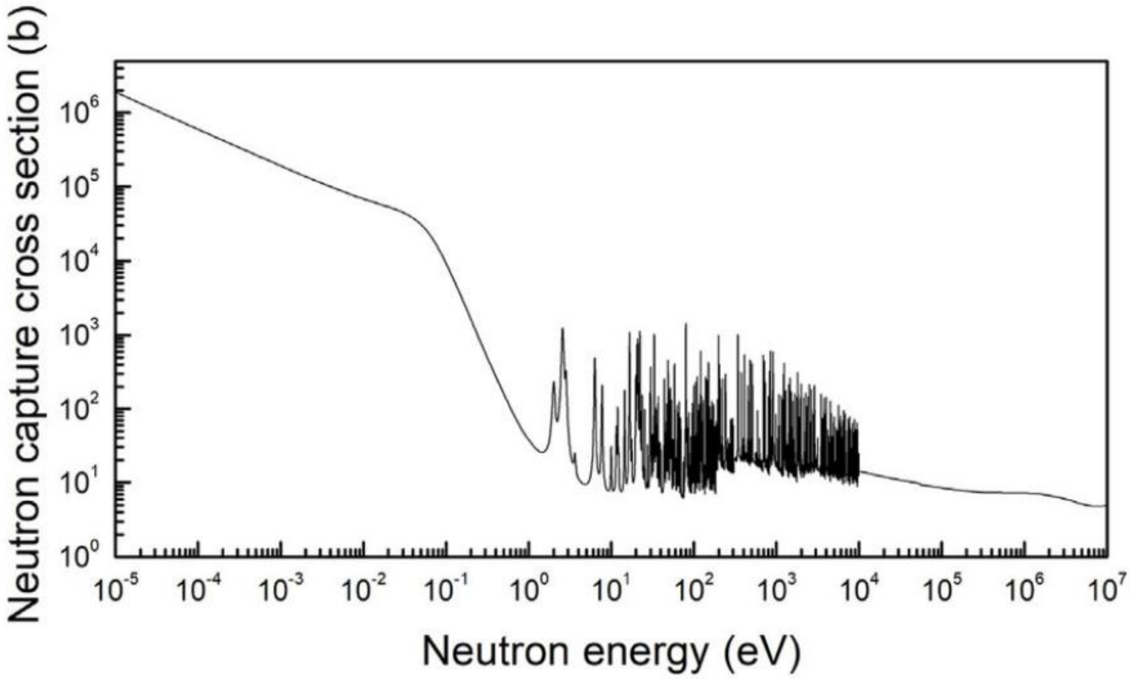

Figure 42 - Neutron cross-section of gadolinium depending on energy of irradiated neutron. [62]

Using data from the neutron spectrum simulation, it is possible to determine the percentage of neutrons produced in the energy range where the cross-section for gadolinium exceeds 10^4 barns. Table 16 summarizes all the relevant information obtained from the F4 output file for the three ion species. Additionally, the same simulation file used to collect the areas also provides the total number of neutrons generated during the procedure. This allows us to relate the total number of neutrons produced in the high cross-section energy range to the areas of the 43 peak regions identified.

	Total of neutrons created.	**Percentage of Neutrons with energy from $\mathbf{0}\ \boldsymbol{ev}$ to $\mathbf{0,1}\ \boldsymbol{ev}$**	**Total of high probability of absorption Neutrons created.**	**Total of Neutrons that went through nuclear reactions**	**Total of neutrons that suffer N.I between $\mathbf{0}\ \boldsymbol{ev}$ to $\mathbf{0,1}\ \boldsymbol{ev}$**
Proton beam	122815	1.57%	1928.19	3537	55.53
Helium beam	739218	0.87%	6431.20	31958	278.03
Carbon beam	2338640	1.40%	32740.96	88620	1240.68

Table 16 - Total of Neutrons created in the MCNP6 simulation with cross-sections higher than 10000 b.

Table 16 shows that the total of neutrons from the high probability of interaction from carbon is approximately 17 times bigger than protons and from helium is 3 times. Its show conformity with the previous analysis, the high probability neutrons produced in the heavier ions had bigger value. The carbon was almost the same, and the helium was half of the total number of neutrons. These results are expected once the carbon and helium have more energy and therefore undergo more nuclear reactions than protons. Additionally, the MCNP6 output file gives the total of neutrons that went through a nuclear reaction. Although is important to mention that this reaction may be happening anywhere in the simulation area, outside of the flask for example. It gives a good approximation because the cross section from the neutron in the water and gadolinium are considerably higher than the air, especially for low energy neutrons, as result of the hydrogen present in the Dotarem® compound [63]. That being said, when compared the neutrons that went through nuclear reactions carbons shows approximately 22 times and helium 5 times more nuclear interactions than protons. It also goes along with the two previous results. By this analysis is possible to verify that the neutron capture is not the one phenomenon causing the discrepancy on the peak area. If the 43 peak area depended only on neutron capture, the values would show carbon and helium with a bigger area than protons. It makes the work turned the eyes of the PIXE phenomenon, discussed in the next section.

5.1.3. PIXE production vs Signal

The previous section checked the neutron production, and the results showed that is being simulated well by the MCNP6. In order to investigate the PIXE, new simulations with the exact same code as described in section 3.3.1. were made but with no neutron transport allowed. It then will show only the PIXE contribution of the areas by the tree ion species. Figure 43 shows the calculated areas from the neutron free simulations, after the same analysis described in section 3.4. As the goal is compare two different simulations, the calculation for the attenuation from the flask wasn’t done, that would increase the uncertainty in the results with no practical use.

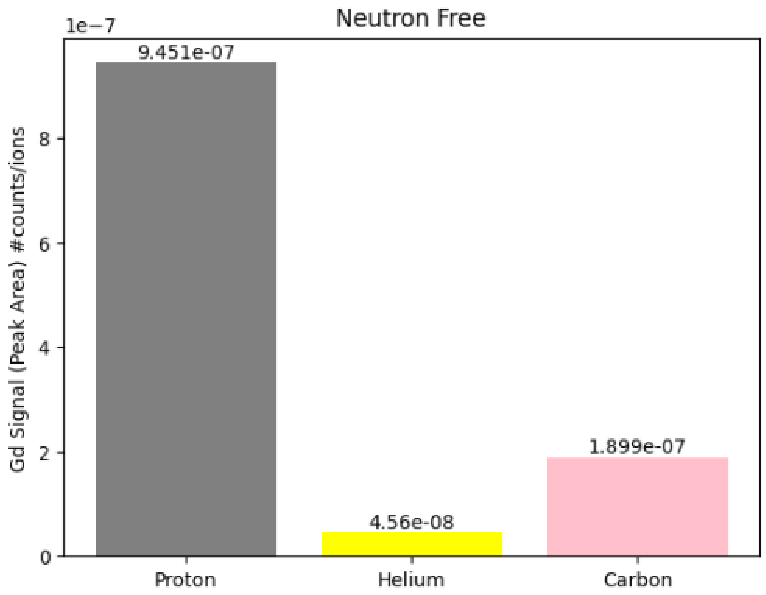

Figure 43 - Neutron Free simulated areas.

Figure 43 shows that the areas without the neutrons have the same problem as a full particle simulation. The proton area is approximately 5 times bigger than the carbon's and 21 times bigger than helium's. Comparing the neutron free values with the total particles values brings the importance of the PIXE to the area of those ion species. Figure 44 shows that compare to the full particle simulation, the discrepancies increased significantly. Initially, the Helium beam had an area 3.2 times smaller, but this difference has now escalated to 21 times smaller. Similarly, the Carbon beam's area, previously 1.6 times smaller, has now increased to 5 times smaller.

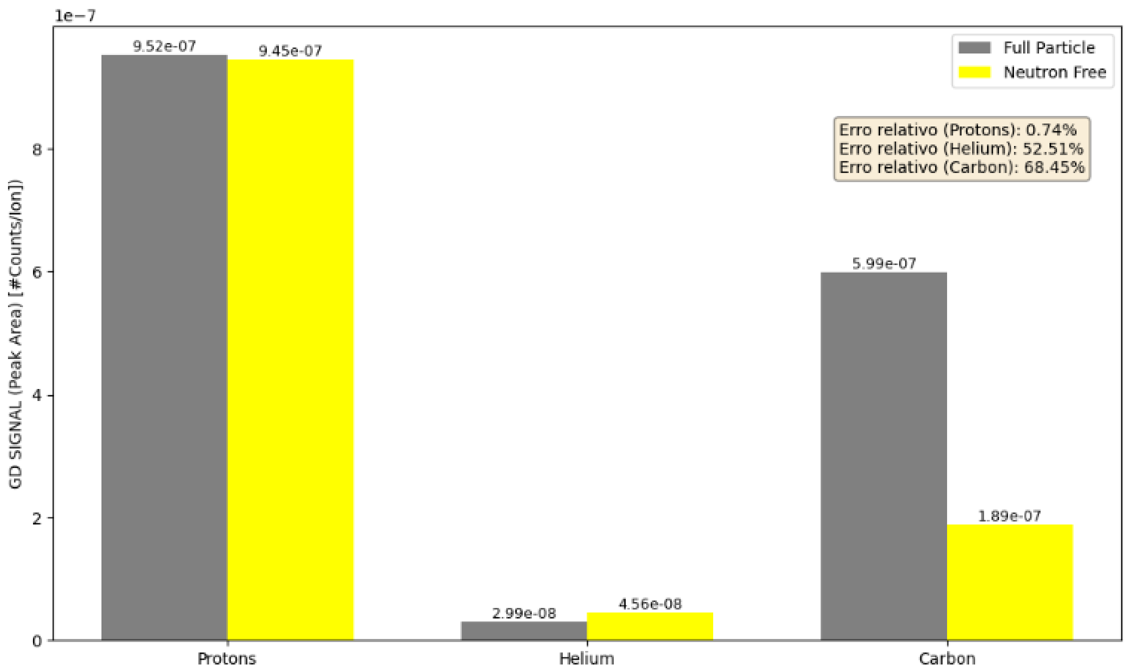

Figure 44 - Bar plot of the calculated 43 peak region area from a full particle simulation vs neutron free particle free simulation on MCNP6

Figure 44 shows that the contribution of the neutron capture for the 43-peak area of the proton beam is not as important as the PIXE, and the area values have a 0.74% relative error. It is confirmed by the previous sections that shows that the neutron production on the proton beam is considerably smaller than helium and carbon, not being it the reason the proton beam has a bigger area than the others. From the same figure, is possible to conclude that the MCNP6 is simulating the PIXE from those particles, however it is doing with less frequency than it is supposed to. Helium has a 6.5 smaller area and carbon 3.1. As discussed previously, the secondary particles of the helium and carbon beams create projectile fragments that can continue with approximately the same velocity as the primary ion. Additionally, those beams may produce many more particles, because protons are considered elementary particles, but carbon and helium are capable of fragmentation of other many others. Those secondary particles also interact with the medium and generate PIXE, it is one of the explanations of why in the experiment the Helium and Carbon areas are bigger than protons. As the peak exists in the neutron free spectrum the particle induced x-ray emission is happening, however, is not possible to know if the secondary particles contribution of it is being counted. Then another identical neutron free simulation was made without any transportation of heavy secondary particles (figure 45), to understand their contribution to the peak area. It means that the proton, helium and carbon simulation will have the source particle electrons and photons only being transported, once they are necessary to the PIXE procedure.

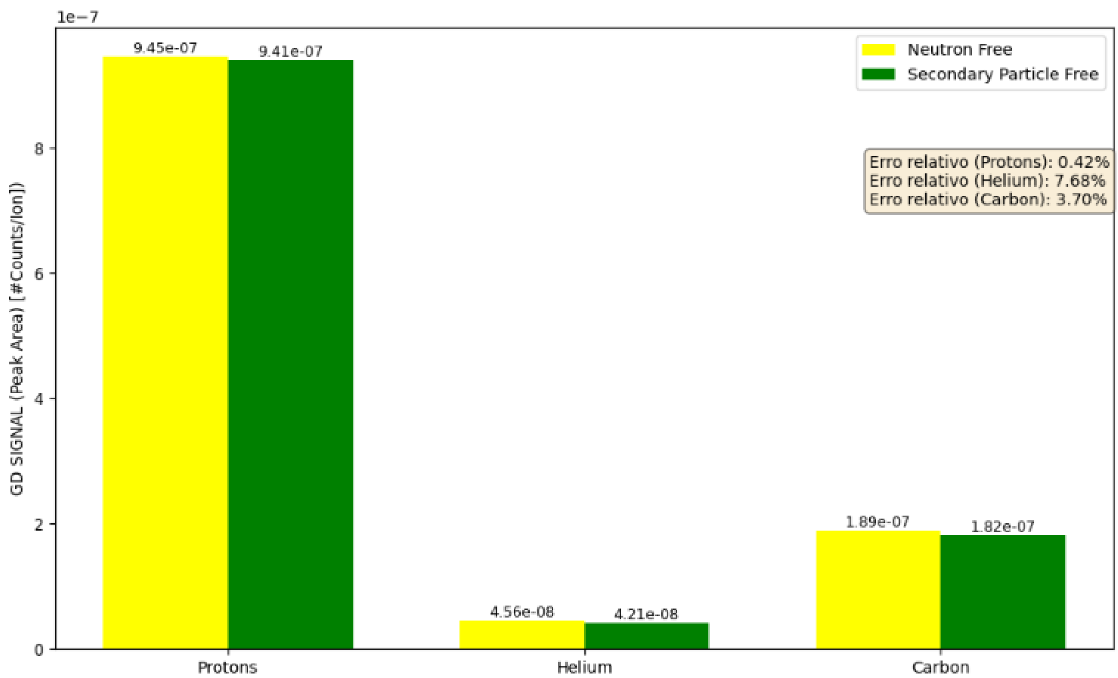

Figure 45 - Bar plot of the calculated 43 peak region area from a full particle simulation vs secondary particle free simulation on MCNP6

Figure 45 shows that the secondary particle contribution on the area is not making any difference on the 43 keV region. For protons the results show that those are not indeed relevant, because proton is considered an elementary particle, in this case, the secondary will not have much energy due to the momentum conservation. And it is also the reason why protons have not tail on the PDD. However, from the same section it would be expected that the free secondary particles simulation of the helium and carbon should be smaller than the full particles neutrons free simulation. It indicates that the secondary particles contribution of PIXE is not being simulated by the cascade mode in MCNP6. From the output file is possible to see that the particles are being simulated, and they interact with the matter, once the *F8 tally presented in table 13, 14 and 15 shows its energy deposition in the medium. The inelastic Coulomb interaction in carbon and helium ions should have a bigger energy deposition on account of its greater atomic number, leading to a bigger charge going through the medium, it is confirmed from results on session 4.2.2., where is possible to see that the energy deposited by the carbon and helium beam are approximately 223.6 and 29.8 times bigger than protons respectively. More energy deposited means more ionizing of the medium and therefore a bigger photon production. However, the results from only source particles, photons and electrons show that the proton beam has still the bigger area, what demonstrates that the MCNP6 simulates the interactions from heavier ions with the medium but does not simulate the PIXE.

After the study of the simulations is possible to notify that the MCNP6 is able to simulate the 43-peak region for the heaviest particles, however with more contribution from the neutron capture process. For the helium beam, when the neutrons were taken out of the simulation, the area become only 15% of the total particle area. Indicating that the neutron capture phenomena contribution for this peak is 85%. If compared to protons, the neutron capture process represents 0.73% of the peak area. It is correct that the neutron contribution for the proton peak must be smaller than helium, but the PIXE phenomenon has to have a greater contribution than the neutron capture. Taking the neutron production as correct it indicates that to simulate helium and its secondary’s PIXE, is necessary to use an increase correct factor of 3.2 with this code setup to adjust to the experimental data.

The carbon analysis goes similarly to the helium’s. When the neutron free simulation showed the area without neutrons were 31 % of the full particle area, it indicated that the neutron capture phenomenon is contributing to 68.6 % of the 43-peak region. The total of neutrons produced in carbon is bigger than the others, however as the experimental plot shows it is not the dominant effect for the peak area creation. Therefore, considering one more time that the neutron creation from MCNP6 simulations with similar physics and cascade model, were tested and validated, it indicates that the MCNP6 need a correct factor of 54.7 to adjust the PIXE production to the experimental data.

Is important to mention that the carbon correct factor is bigger than helium's, it confirms the lack of production of PIXE, because the neutron production from carbon is 19 times bigger, and if the neutron capture would be the dominant phenomenon on the peak creation, the experimental area from carbon should have a smaller difference from the simulated area than helium's. And what happened is the opposite, even though the neutron production is higher for carbon, the area still gets more discrepancy. Additionally, carbon has more charge, more atomic number and consequently bigger LET, what makes it interact with the medium more likely than the others. Is expected to have more PIXE from bigger ions due to this theoretical statement

5.2. Equivalent Dose

The tables listed in session 4.2.2. summarize all the dose deposition registered by the *F8 tally placed in the Dotarem® flask. Is possible to see the contribution of each particle for the absorbed dose and the equivalent dose, this one calculated using the radiation weighting factor listed in the ICRP 103, shown in table 8. The first analysis is made by the absorbed dose perspective and then for the equivalent dose after. And as the goal is compare the impact of the energy deposition with the signal from the 43 peak region area, is more accurate to understand the damage caused from the ion on the human tissue.

5.2.1. Proton Beam

As mentioned in session 2, the proton beam produced low energy secondary particles that have no considerable impact in the total dose of the medium. However, every proton that goes under a nuclear reaction is taken out of the beam, making the flux smaller. From the results placed in table 13 is possible to see this behavior, where the absorbed dose from proton particles represents 99.71% of the total dose, and the photons and electrons are the second bigger with 0.12% each. The heavier fragments summed represent 0.000269% of the total dose and the neutrons 0.05%. Observing the flux from the previous sessions, the total area of the 43 peak region is barely decreased when the simulation was neutron free and secondary particle free, what agrees with the data in this session. Despite the small contribution of heavier particles and neutrons particles for the absorbed dose, due to the radiation weighting factor from neutrons, when calculated the equivalent dose, the contribution of protons to it decreases to 99.49 % because the neutrons increase to 0.37%. It explains figure 8 why proton beams have no tail after the Bragg-peak, there are not secondary particles with energy enough to make a deposition of a considerable amount of dose. Additionally, protons interact less compared to the heavier ions that have the same energy, owing to its smaller LET, that is why the range of the protons are higher (figure10) and then, if consider that this simulations ran 1×10^8 particles, the total dose absorbed in the flask is $8.04 \times 10^{-12}\,Gy$, approximately 3 times smaller than helium and 22.5 times than carbon. When the comparison takes place in the equivalent dose, the values go even higher, the total value for the proton beam is $1.61\ mS_v$, approximately, 30 times smaller than helium and 224 time than carbons.

5.2.2. Helium Beam

The output from the helium beam, placed in table 14, brings almost the same pattern as protons. 99.20 % of the energy deposit come from hellions, being the second higher contribution coming from neutrons 0.74%, making the rest of the particles summed a total of 0.05% approximately. However, the neutron creation from helium beams is mostly placed in the range of 1 to 50 MeV, what represents neutrons with smaller cross-sections to the medium. The reason neutrons contribute higher to the Helium Beam is that the production of this particle is approximately 6 times bigger than protons beams, as shown in table 16. Even though the production is that high, the contribution for the doses only increased about two times, due to the range of energy and the smaller cross sections for those neutrons. The LET for the helium particle is 4 times greater than protons with the same velocity. It means that the helium ions will have a greater deposition of energy than protons, what can be seen in table 14, again considering the simulation with 1×10^8 particles, it shows the total absorbed dose from helium being $2.40 \times 10^{-3} Gy$, about 3 times bigger than protons. However, this greater atomic number and interactions creates secondary particles, including secondary protons, that are able to deposit dose themselves, and that is the reason why figure 8 proton beams show a tail. When the comparation takes place in the equivalent dose, the total from helium is $48\ mS_v$, the difference increases to 30 times because the heavier particles have heavier radiation weighting factors.

This discrepancy of values is well represented in the peak area from the experiment, where the helium gadolinium signal was 5 times greater than protons. As mentioned, the dose contribution comes mostly from ionizing the medium, same procedure that make the particle induced x-ray emission from gadolinium, therefore as 3 times more dose was deposited it suggest that the 43-photon emission would also increase more less at the same number, because the emission of secondary's is calculated using a probability function for the LAQGSM03.03 cascade model, more interactions more probability of emission. Additionally, the neutron production was 6 times higher, and the neutron contribution for doses was 2 times higher, meaning that this particle interacted approximately 2 times more with the medium, also increasing the chances of neutron capture phenomena to happen.

5.2.3. Carbon beam

As carbon ions have more atoms, 12 to be exact, the probability of fragmentation and creation of high energy secondary is greater than protons and helium. It can be seen in table 15, where the total absorbed dose contribution of heavier ions represents 98,64% percent of the total dose, it represents that the contribution of the other particles, beside the source, is greater than the two ions species analyzed before. The neutrons made 0.58% contribution, because even though the creation of neutrons in the carbon beam is 19 times greater, most of these particles are created over 50 MeV of energy, making their cross-section the smallest among all the ion species. The other contributions come from proton 0.21%, deuterium 0.18%, triton 0.10%, alpha particles 0.25%, all those particles resulted from the fragmentation process after the carbon ion nuclear interaction with the medium. It represents more than the other two ion species, and that is the reason carbon ions show a big tail in the PDD, because those particles have energy enough to ionize the medium. As result of carbon bigger atomic number, the interaction of these particle is way more frequent than the others, therefore the total dose deposited from this is $1.81 \times 10^{-1} Gy$, 224 times bigger than protons and 7 times bigger than helium. For the same reason as helium, more absorbed dose represents more interactions and therefore more 43 photons production would be expected. When the equivalent dose takes place the difference between them increases, as the particles created in the carbon beam have a greater radiation weighting factor. The total equivalent dose is $360\ mS_v$, it represents 7.5 times the helium's and 224 times protons.

5.2.4. Physics absorbed dose comparation

The data from table 19 shows the details used in the gadolinium irradiation for the experimental setup. Is possible to see that the carbon and helium beams had a 4 times bigger intensity (particles/s) than protons. The total absorbed dose depends on the flux of particles as well as the energy of it. These factors must be taken into account in the comparative analysis. For that reason, the peak area on the experimental setup has to be normalized for the number of particles, it will bring all the data for the same scale. The normalized Area (N.A.) of the tree ions is calculated as follows:

- $N.A. = \frac{Measured\ Area}{\frac{Particle}{second} \times time\ of\ irradiation} = Normalize\ area. \left[\frac{\#counts}{ions^2}\right]$

- $Nornalized\ area\ (protons) = 1.36 \times 10^{-17}\ \frac{\#counts}{ions^2}$
- $Nornalized\ area\ (helium) = 2.80 \times 10^{-16}\ \frac{\#counts}{ions^2}$
- $Nornalized\ area\ (carbon) = 4.98 \times 10^{-15}\ \frac{\#counts}{ions^2}$

Additionally, to compare the emission of the signals the area has also to be normalized per dose. The total absorbed dose per particle simulated, shown in the second of table 13, 14 and 15 will be used to normalize the area:

- $N.A1 = \frac{N.A.(ion\ species)}{Absorbed\frac{Dose}{ion}} = Normalized\ area.\left[\frac{\#counts}{ions.Gy}\right]$
- $Nornalized\ area1\ (protons) = 1.36 \times 10^{-17}\ \frac{\#counts}{ions.Gy}$
- $Nornalized\ area1\ (helium) = 2.80 \times 10^{-16}\ \frac{\#counts}{ions\ .Gy}$
- $Nornalized\ area1\ (carbon) = 4.98 \times 10^{-15}\ \frac{\#counts}{ions.Gy}$

Those values are plotted in figure 46 to represent the normalized signal of gadolinium with the ions species at the same scale. The bar plot shows that the signal for protons beams is approximately 20.6 and 366 times smaller than helium's and carbon's respectively. The difference between the ion species after the normalization got bigger for two reasons, first the dose deposited by the helium and carbon is 22.5 and 3 times bigger than protons respectively. It indicates that less particles of those heavier ions are needed to emit 43 keV photons. And the second reason is the number of particles used in protons beams were 4 times greater than the others, it because protons itself have a small area and charge, so they interact less with the medium and generate less signal. Only considering physical dose, the carbon signal would be the biggest if all of those tree beams were supposed to deliver the same dose to a target.

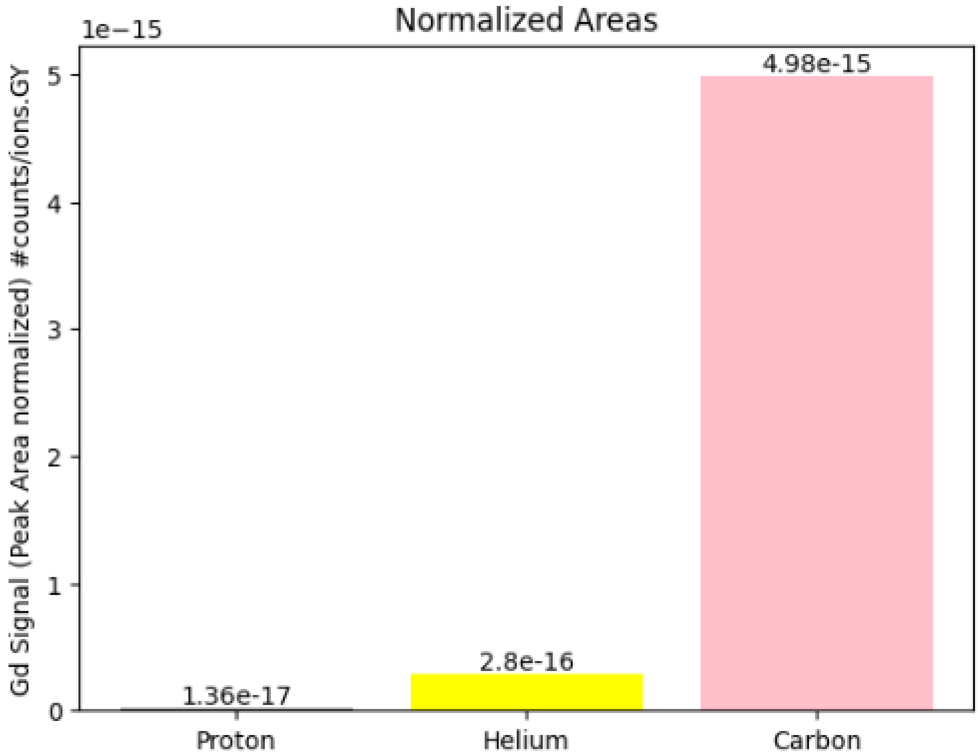

Figure 46 - Normalized area for particles/second and Gray.

5.2.5. Equivalent dose comparation

When the comparison is made in terms of the RBE, the results create a bigger importance on the future of in vivo dosimetry per hadrons radiotherapy. Once the biological effect from different radiation is considered, the situation becomes more realistic in the clinic context. It is because the cell in the human body feels the effects of the radiation differently, and when a treatment is done with this technique, this factor is considered. For the total equivalent dose calculation, the normalization process done in the previous section will be the same. Taking information from the simulation on tables 13, 14 and 15 for the tree ion species, considering now the last column, the procedure goes as follows:

- $N.W.A. = \frac{N.A.(ion\ species)}{Weighted\ absorbed\frac{Dose}{ion}} = N.A.weighted.\left[\frac{\#counts}{ions.mS_v}\right]$
- $Nornalized\ Weighted\ area(protons) = 8.44 \times 10^{-10}\ \frac{\#counts}{ions.mS_v}$
- $Nornalized\ Weighted\ area\ (helium) = 5.84 \times 10^{-10}\ \frac{\#counts}{ions.mS_v}$
- $Nornalized\ Weighted\ area\ (carbon) = 1.38 \times 10^{-9}\ \frac{\#counts}{ions.mS_v}$

The heavier the particles are the more contribution to the equivalent dose due to its bigger radiation weighting factor, as it is shown in table 8. As explained in the previous chapter the carbon ion doses contribution comes mostly (98,64%) for heavier ions and the rest is generally divided by the other heavier ions. It represents that the carbon beam has a greater power of damage in the human tissue than the others, therefore, less physical dose is necessary to accomplish the damage wanted in the treatment. Generally, it would represent less particles interacting with the medium and less signal for the 43-peak region. However, the fragmentation and the bigger let makes a balance of this count helping the heavier particles to have more peak fluence, as it is seen in the experiment bar plot. The investigation of this section is summarized in figure 47, where this balance mentioned is measured and a quantitative number shows the most efficient radiation for the in vivo dosimetry technique mentioned in this work.

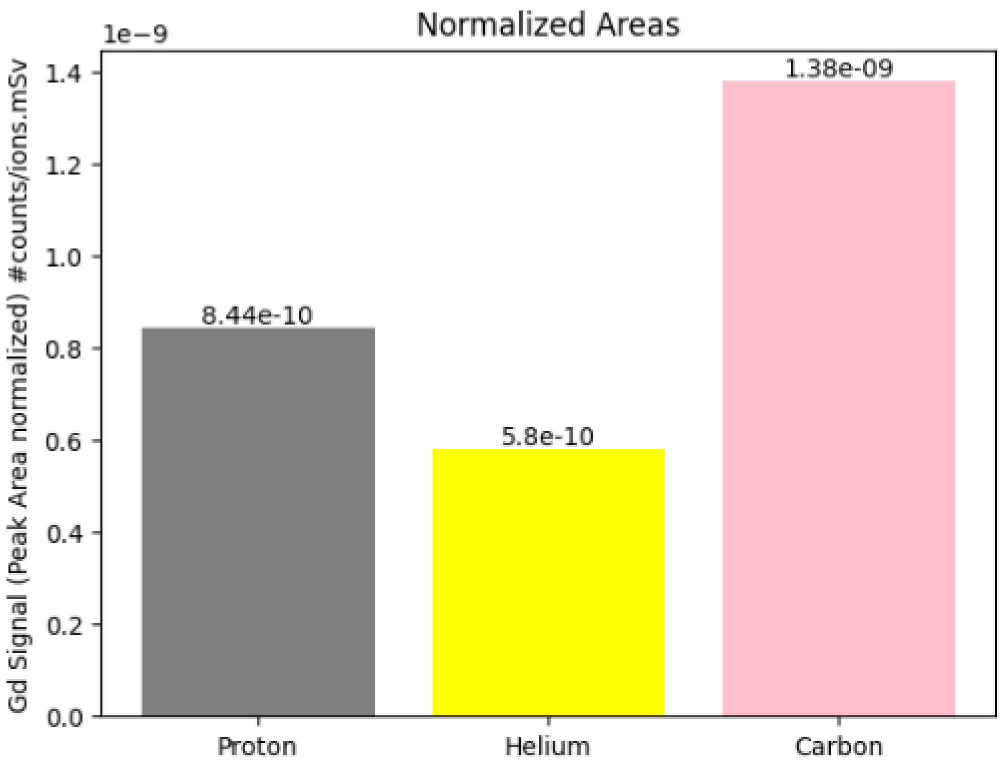

Figure 47 - Normalized weighted area of the 3 different ion species.

When considered the total equivalent dose the proton's area becomes approximately 1.5 times bigger than helium's. It means to deposit 1 mSv of dose, a single proton particle from the source beam would emit 1.5 bigger signal than helium's. It makes the proton beam a better candidate for in vivo dosimetry than helium. Even though the area generated in the experiment by the Helium beam was 5 times bigger, the total dose absorbed, checked in the simulation, was not big enough to overcome the greater *LET* and consequently the greater equivalent dose from the helium particles. On the other hand, the carbon beam showed a 1.6 times greater signal per ion per mSv than protons, it means that the total dose absorbed dose generated by the carbon beam and the heavier secondary fragments overcome the fact of its LET being bigger. The total area got in the experiment from carbon was approximately 92 times stronger, and the total dose deposition was even stronger, the normalized area at figure 46 showed the carbon ion having a 366 times stronger signal per Gray of absorbed dose. This huge difference in that signal was the reason that even though the particles in the carbon beam have bigger radiation weighted factor, it would be still a 1.6 bigger signal generated from a single source particle of carbon to deposit one mSv of dose.

It is important to mention that the normalized weighed area showed less difference between the ion species, showing that in vivo dosimetry may work for them all with no further modification in the geometry setup. It is important to clinic experience that this result shows less difference because it represents less modification in the treatment area during the procedures.

6. Conclusion

The Monte Carlo code has been used in medical physics since the 1960s and has become increasingly important over the decades. Monte Calor N-Particle 6 has been verified and validated many times for different studies for many different tasks. The opportunity of testing the MCNP6 capacity to simulate the secondary prompt gamma-ray and characteristic x-ray emissions for proton beam has been done before, however for Helium and Carbon ions is the first time. The program simulates well the neutron production and its contribution to the 43-peak, however the PIXE phenomenon needs an increase factor of 3.2 for helium and 54.7 for carbon, to adjust to the experimental data. The reason is the lack of PIXE production of the ion source itself and the secondary's. It represents that for in vivo dosimetry technique using prompt gamma-ray and x-ray emission from helium and carbon, the MCNP6, with this configuration, wouldn't be a trustful tool to work with. A further investigation has to be done on the code possibility's to see it can be overcome.

The secondary goal of the work to verify which technique is more favorable to work with in vivo dosimetry showed that the carbon ion overcomes it's bigger LET and would emit the bigger signal when compared at the same circumstances of the others. Followed by protons and helium. It makes the carbon ions a good candidate to this technique in further clinic treatments. The results showed that the difference between the signals would not change much from the ion species, it might represent no bigger adaptation on the setup for one beam to another during the clinical day to day treatment schedule.

Further investigation on the MCNP6 code is necessary to determine if the software is not capable of simulating well the PIXE. The total of possibilities presents in the code make possible to overcome the lack of photons present in this work simulations. A big investigation was conducted to build this code, however always using previous work and theoretical statements to maximize the results reliability but turning the time of simulation smaller. This efficiency seeks limited the work, as the time to seek for new ways of simulating the phenomenon was short.

Further investigations into in vivo dosimetry techniques could build upon the findings and recommendations presented in this study. A water thank experiment with the scintillator detector and a dosimeter can show the dose relationship with the area of the peak, plotted in this work and confirm the possibility of having the in vivo dosimetry technique for those heavier ions.

This study introduces new opportunities for comparing ion species, facilitating their application in in vivo dosimetry techniques. For heavier ions than protons it has never been checked they capacity of working with it. The bigger LET of those particles would suggest that the peak signal would be smaller than protons, but the results showed otherwise. Additionally, the MCNP6 capacity of helping with the technique proposed in this work was tested and showed that it needs to be adjusted yet.

In vivo dosimetry plays a critical role in radiation therapy by ensuring that the dose delivered to a patient matches the prescribed dose, directly enhancing both safety and treatment efficacy. The present work helped to understand the capacity of MCNP6 helping with prompt gamma-ray and x-ray techniques of in vivo dosimetry as well as showed the difference signals of Gadoliniums' 43 keV peak area for the different ion species, bring information that will help a future implementation of the technique.

Reference

[1] G. R. W. U. L. J. T. G. L. Gianfaldoni S, “An Overview on Radiotherapy: From Its History to Its Current Applications in Dermatology.,” 2017.

[2] L. K. H. Y. C. J. Z. J. Tian X, “The evolution of proton beam therapy: Current and future status,” 2018.

[3] K.Hesketh, “Gadolinium,” em *Comprehensive Nuclear Materials*, 2012.

[4] Newhauser WD, Zhang R, “The physics of proton therapy,” *PMC PubMed Central,* pp. 155-209, 24 Mar 2015.

[5] Joost M Verburg; Helen A Shih; Joao Seco1, “Simulation of prompt gamma-ray emission during proton radiotherapy,” *Physics in Medicine & Biology,* 3 August 2012.

[6] S. G. Mashnik, “Validation and Verification of MCNP6 Against Intermediate and High-Energy Experimental Data and Results by Other Codes,” *Los Alamos National Laboratory,* 2013.

[7] E. H.Grubbé, “Priority in the Therapeutic Use of X-Rays,” 1933.

[8] E. Podgorsak, Radiation Oncology Physics: A Handbook for Teachers and Students, 1 ed., Viena: IAEA, 2005.

[9] Ashraf Muhammad Ramish; Rahman Mahbubur; Zhang Rongxiao; Williams Benjamin B; et. al., “Dosimetry for FLASH Radiotherapy: A Review of Tools and the Role of Radioluminescence and Cherenkov Emission,” *Frontiers in Physics,* p. 8, 21 August 2020.

[10] R. R. Wilson, “Radiological Use of Fast Protons,” *Radiology,* 1 Nov 1946.

[11] M. R., “A Review of Proton Therapy - Current Status and Future Directions.,” 2022.

[12] Michiko G. Minty, Frank Zimmermann, Measurement and Control of Charged Particle Beams, Springer Verlag, 2003.

[13] I. p. 26, “Recomendations of the ICRP,” 1977.

[14] Durante M, Debus J, Loeffler JS., “hysics and biomedical challenges of cancer therapy with accelerated heavy ions.,” *Nat Rev Phys.,* 3 Dec 2021.

[15] P. P. R. J. A.Wambersie(a)(b), “Biological weighting of absorbed doses in proton and heavier ion-beam therapy: ICRU-IAEA,” 2009.

[16] ICRP, “Recommendations of the International Commission on Radiological Protection. ICRP Publication 60,” 1991.

[17] La Rosa V, Kacperek A, Royle G, Gibson, “A. Range verification for eye proton therapy based on proton-induced x-ray emissions from implanted metal markers.”.*Phys Med Biol.*.

[18] Polf JC, Peterson S, McCleskey M, et al, “Measurement and calculation of characteristic prompt gamma ray spectra emitted during proton irradiation.,” *National Library of Medicine,* 21 Nov 2009.

[19] W. Maenhaut, “X-ray fluorescence and emisson | Particle-Induced X-ray Emission,” *Encyclopedia of analytical Science,* pp. 432-442, 2019.

[20] Golnik C, Hueso-González F, Müller A, et al., “Range assessment in particle therapy based on prompt γ-ray timing measurements.,” *National Libery of Medicine,* 26 AUg 2014.

[21] Berger, “Penatration of proton beams through water,” *National Institute of Standards Technology,* 1993.

[22] K. A. Christine, “Range Verification Methods in Particle Therapy: Underlying Physics and Monte Carlo Modeling,” *Frontiers in Oncology,* 2015.

[23] Chul-Hee Min, Chan Hyeong Kim, Min-Young Youn,Jong-Won Kim, “Prompt gamma measurements for locating the dose falloff region in the proton therapy,” *Applied Physics Letters,* 02 Nov 2006.

[24] Antje-Christin Knopf, Antony Lomax, “In vivo proton range verification: a review,” *Physics in Medicine & Biology,* 17 July 2013.

[25] J. Krimmer, D. Dauvergne, J.M. Létang, E. Testa, “Prompt-gamma monitoring in hadrontherapy: A review,” *HAL open science,* 23 Jun 2022.

[26] Ricardo Dal Bello, Paulo M. Martinn, etc al., “Prompt gamma spectroscopy for absolute range verification of 12C ions at synchrotron-based facilities,” *Physics in Medicine & Biology,* 7 May 2020.

[27] Hueso-González F, Rabe M, Ruggieri TA, Bortfeld T, Verburg JM., “A full-scale clinical prototype for proton range verification using prompt gamma-ray spectroscopy.,” *National Library of Medicine,* 17 Sep 2018.

[28] Benzion Kozlovsky; Ronald J. Murphy; and Reuven Ramaty, “Nuclear Deexcitation Gamma-Ray Lines from Accelerated Particle Interactions. ICRU report 63,” *The Astrophysical Journal,* AUgust 2002.

[29] N.Soppera, E.Dupont, M. FLeming, “Nuclear Agency Energy,” September 2020. [Online]. Available: https://www.oecd-nea.org/janis/book/book-proton-2020-09.pdf.

[30] J. S. Y. K. J. P. K. S. W. L. K. L. K. K. B. P. J. Byun, “Monte-Carlo simulation for detecting neutron and gamma-ray simultaneously with CdZnTe half-covered by gadolinium film,,” *ScienceDirect,* March 2023.

[31] O. Jakel, “Physical Advantages of partices : protons and light ions,” *British institute of Radiology,* 09 may 2019.

[32] .. J. A. S. DAVID A. SCHAUER, Clinical Dosimetry, 2003.

[33] B. M. P. i. Marion Essers Ph.D., “In VIvo dosimetry during external photon beam radiotherapy,” *International Journal of Radiation Oncology*Biology*Physics,* 1999.

[34] Rogosnitzky M, Branch S, “Gadolinium-based contrast agent toxicity: a review of known and proposed mechanisms,” *National Library of Medicine,* 06 april 2016.

[35] Michael A. Ibrahim1; Bita Hazhirkarzar2; Arthur B. Dublin3., “Gadolinium Magnetic Resonance Imaging,” *National Library of Medicine,* 3 July 2023.

[36] R. Formento-Cavaier, F. Haddad,C. Alliot etc al., “New excitation functions for proton induced reactions on natural gadolinium up to 70,” *ELSEVIER,* 1 September 2020.

[37] C. Vermeulen, G.F. Steyn, F. Szelecsényi, et al., “Cross sections of proton-induced reactions on natGd with special emphasis on the production possibilities of 152Tb and 155Tb,” *Nuclear Instruments and Methods in Physics Research Section B: Beam Interactions with Materials and Atoms,* 15 March 2012.

[38] Van Delinder, K.W., Khan, R. & Gräfe, J.L., “Neutron activation of gadolinium for ion therapy: a Monte Carlo study of charged particle beams,” *Scientific Reports,* 28 July 2020.

[39] J.L. Gräfe, F.E. McNeill, D.R. Chettle, S.H. Byun,, “Characteristic X ray emission in gadolinium following neutron capture as an improved method of

in vivo measurement: A comparison between feasibility experiment and Monte–Carlo simulation,," *Nuclear Instruments and Methods in Physics Research Section B: Beam Interactions with Materials and Atoms,,* 2012.

[40] N.Nica, "Nuclear Data Sheets 160," 2019.

[41] N.Nica, "Nuclear data sheets 132," 2016.

[42] J.L. Gräfe, F.E. McNeill, S.H. Byun, D.R. Chettle, M.D. Noseworthy, "The feasibility of in vivo detection of gadolinium by prompt gamma neutron activation analysis following gadolinium-based contrast-enhanced MRI,," *ELSEVIER,* 2011.

[43] Kulesza, Joel Aaron and Adams, Terry R. and Armstrong, et. al., "TechReport_2022_LANL_LA-UR-22-30006Rev.1_KuleszaAdamsEtAl," Los Alamos National Laboratory, Los Alamos, NM, USA, 2022.

[44] S. Z. M. Vahabi SM, "Aplications of MCNP simulation in treatment planning: a comparative study," *PUBMED,* 2020.

[45] J. D. I. J. C. A. M. T.D.Solberg, "A review of radiation dosimetry applications using the MCNP Monte Carlo code," 2001.

[46] J. L. Conlin, "Listing of Available ACE Data Tables," 2017.

[47] C. J. Werner, MCNP User's Manual, 2017.

[48] J. Solc, "Comparison of proton interaction physics models and cross section libraries for proton therapy Monte Carlo simulations by MCNP6.2 code," *ELSEVIER,* 2019.

[49] F.G.A. Quarati, P. Dorenbos, J. van der Biezen, Alan Owens, M. Selle, L. Parthier, P. Schotanus, "Scintillation and detection characteristics of high-sensitivity CeBr3 gamma-ray spectrometers,," *Elsevier,* pp. 596-604, 21 November 2013.

[50] Hugo Freitas, Mariana Brás, Jose Vedelago, James Grafe e João Seco, "PGS Gadolinium Project," *HIT PGSX Report GDFLASH,* 9 October 2022.

[51] Mashnik, S. & Gudima, Konstantin & Prael, R. & Sierk, A. & Baznat, M. & Mokhov, N.V.., " CEM03.03 and LAQGSM03.03 Event Generators for the MCNP6, MCNPX, and MARS15 Transport Codes," *Invited Lectures at Joint ICTP-IAEA Advanced Workshop on Model Codes for Spallation Reactions,* 2008.

[52] J.K. Shultis, R.E. Faw, “An MCNP Primer,” Dept. of Mechanical and Nuclear Engineering, Kansas State University , 2006.

[53] S. G. Mashnik, “Validation and Verification of MCNP6 Against High-Energy Experimental Data and calculations by Other Codes.,” *Los Alamos National Laboratory ,* August 2011.

[54] S.G.Mashnik, K.K. Gudima, N.V.Mokhov and R.E.Prael, “LAQGSM03.03 Upgrade and its Validation,” *Los Alamos National Laboratory,* August 2007.

[55] M. Reiser, The Theory and Design of Charged Particle Beams, USA: Wiley-VCH, 1994.

[56] Forrest B. Brown, Jeremy E. Sweezy, Robert B. Hayes, Monte Carlo parameters studies and uncertainty analysis with MCNP5, Chicago: Los Alamos National Laboratory, 2004.

[57] F. Brown, “A Tutorial on Merging Tallies from Separate MCNP5 Runs.,” 2008.

[58] Hughes, Henry Grady III, Improvements in Electron-Photon-Relaxation Data for MCNP6, Los Alamos National Laboratory, 2016.

[59] I. D. O. H.SMITH, “Conversion Coefficients for use in Radiological Protection against External Radiation,” International Commission on Radiological Protection, 1996.

[60] J.Valentin, “The 2007 Recommendations of the International Comission on Radiological Protection,” The international Comission on Radiological Protection, 2007.

[61] R. E. W. Rafael C. Gonzalez, Digital Image Processing, 2017.

[62] E. a. Zsolnay, “Summary Description of the New International Reactor Dosimetry and Fusion File,” International Atomic Energy Agency IAEA;, Vieana, 2012.

[63] A. Munter, “Center of Neutron Research,” 2021. [Online]. Available: https://www.ncnr.nist.gov/resources/n-lengths/list.html.

[64] Knäusl, B., Fuchs, H., Dieckmann, K., & Georg, D, “an particle beam therapy be improved using helium ions? – a planning study focusing on pediatric patients,” *Acta Oncologica,* 2016.

[65] e. a. A.D.Carlson, “IAEA NEUTRON DATA STANDARDS,” 2017. [Online]. Available: https://www-nds.iaea.org/standards/.